EXPERIMENTAL INVESTIGATION OF WAVES BREAKING OVER A BAR IN THE SURF ZONE

By

Ursula Pillay

BSc (Hons)

A THESIS SUBMITTED IN FULFILLMENT OF THE REQUIREMENTS FOR THE DEGREE OF MASTER OF SCIENCE IN THE DEPARTMENT OF PHYSICS IN THE FACULTY OF SCIENCE AT THE UNIVERSITY OF KWAZULU-NATAL (WESTVILLE CAMPUS)

January 2005

Dedicated to the memory of Cindy, Puppy, Anesh and Unnie

DECLARATION

THE REGISTRAR (ACADEMIC)
UNIVERSITY OF KWAZULU-NATAL

DEAR SIR / MADAM

I, URSULA MONICA PILLAY

REG.No.: 9403733
DEGREE: MSc PHYSICS

HEREBY DECLARE THAT THE DISSERTATION ENTITLED

Experimental investigation of waves breaking over a bar in the surf zone

IS THE RESULT OF MY OWN INVESTIGATION AND RESEARCH, EXCEPT FOR THOSE ITEMS EXPLICITLY MENTIONED IN THE ACKNOWLEDGEMENTS, AND THAT IT HAS NOT BEEN SUBMITTED IN PART OR FULL FOR ANY OTHER DEGREE OR TO ANY OTHER UNIVERSITY.

..... 14-01-2005

SIGNATURE DATE

ACKNOWLEDGEMENTS

The presentation of this dissertation would not have been possible without the significant contributions of the following people:

Dr. K. Govender, for his direction and supervision and all that I have learnt from him during the period of my research. In particular I would like to acknowledge the following contribution by Dr. Govender; conducting the experiments and capturing the raw data, assisting in writing up Chapter 3, especially section 3.4, making available his CIV programmes and assisting in the phase-ensemble-average calculations.
Dr. S. Moolla for his computational assistance and his encouragement.
Mr H. Edwards for his computational assistance.

Prof. M. McPherson for his guidance and encouragement.
The members of the Physics department, especially Robert van den Heetkamp, Ronald Teemane and Pam Singh, for their encouragement and advice.

My family for their patience, love and support from the very start.
Kuben Naicker, whose love, support and encouragement have been indispensible.

Finally, I wish to thank God for all that she has done for me.

The financial support supplied by the NRF and the Joint France/South Africa Science and Technology Agreement is acknowledged.

ABSTRACT

Experiments on regular two dimensional waves breaking over an artificial sand bar were conducted in a glass walled flume to facilitate an investigation of the hydrodynamic processes that evolve in the surf zone. The instantaneous time averaged velocities and the velocity flow fields have been measured using digital video imaging and analysis techniques. The instantaneous velocity flow fields were then processed, resulting in the phase-ensemble-averaged velocities, time averaged velocities and energy and momentum fluxes. The time averaged velocities above the trough level have been found to be much higher than those below. After wave breaking, kinetic energy and momentum flux are shown to increase, reaching a peak value and decreasing thereafter. An estimate of the relative density of the fluid in the wave crests was obtained by comparing the forward and reverse velocity fluxes.

Other surf zone physical parameters such as the free surface displacements, wave heights across the flume and potential energies have been derived from the resistive wave gauge measurements. A spectral analysis of the water level time series was conducted and the energy growth in each spectral component was examined. It was noticed that there is a transfer of energy from the primary frequency of the wave maker to higher harmonics. Also, wave breaking has little effect on the amplitudes of the harmonic components.

The roller and aeration areas were also computed. Two methods of estimating the roller area have been explored and these are the analysis of the wave gauge measurements of the surface elevation and the analysis of the

video images. There was agreement between the results obtained and those published in the literature.

Contents

List of Figures

Chapter 1

Introduction

The oceans, which cover vast expanses are used daily for transport, recreation, swimming, fishing, surfing and boating. It is for this reason that the processes that influence these activities are investigated. The part of the ocean that is most well known and least understood is the surf zone, a region where wave breaking occurs. Breaking waves play a vital role in the air-sea interaction, the transfer of momentum from waves to currents, the generation of turbulence and the subsequent sediment suspension and transport.

A knowledge of the hydrodynamics of breaking waves is of great importance as life is, in some way or the other, affected by the oceans. The design of offshore structures for industrial activity is dependent on an understanding of the behaviour of the ocean. Incorrect deployment of structures near the shore or off-shore can have major repercussions for the coastline. One of the aims of this research is to quantify the decay of wave energy, in particular in waves breaking over a sand bar. In the process, other objectives include the

investigation of the generation of mean currents and the comparison of video measurements with measurements obtained using different methods. These results will be useful in the understanding and prediction of beach erosion and sediment transport.

1.1 Physical processes

Ocean waves are produced by a variety of forces. Wind and pressure produce swells, astronomical forces produce the tides and earthquakes produce tsunamis. In deep water, because the ratio of wavelength to water depth is so small, the passage of waves is hardly noticeable. Deep water waves have a sinusoidal profile. The wave particle orbits are circular in deep water and the wave speed depends on the wavelength. In deep water, waves of longer wavelengths travel faster than those of shorter wavelengths.

It is when deep water waves enter regions of shallow water that many interesting processes take place. The wave profile is no longer sinusoidal but instead the crests become peaked and the troughs are drawn out. The particle orbits in shallow water are elliptical. Closer to the bottom boundary, the orbits are more flattened. Shallow water waves are non-dispersive and the wave speed is controlled by the water depth.

When deep water waves encounter a decreasing water depth several transitions occur. As the water depth decreases, the waves slow down and the

wave height increases. The front face of the wave continues to steepen until the crest becomes unstable and the wave breaks. Wave breaking results in the formation of a roller that rides on the front face of the wave. The roller is a mass of aerated fluid. From a biological perspective, wave breaking is important since it aerates the water and this sustains life within the oceans. Wave breaking also results in the creation of rip currents, longshore currents and undertow currents. Rip currents run on the surface of the water from the shore towards the break point, undertow runs near the bottom of the wave from the shore towards the break point and longshore currents are currents that run parallel to the shoreline. There are also high levels of turbulence associated with wave breaking. It is this turbulence that suspends sediments that are eventually carried away by the currents.

Sediments transported by the undertow current are eventually deposited at the break point. This then results in the erosion of the beach and an accumulation of sediment at the break point resulting in the formation of a sand bar. The sand bar in turn influences the wave breaking process. It is the aim of this thesis to investigate the breaking of waves over the bar and the subsequent generation of currents.

1.2 Theoretical developments

The field of Hydrodynamics is well described by the Navier-Stokes equation. This equation is highly non-linear and when the boundary conditions at the

surface are taken into account, the problem of non-linearity is enhanced. At present there is no general solution to the equation. The way to simplify any such equation is to consider possible approximations relevant to a particular case. Solutions to the Navier-Stokes equation in deep water have been possible through the linearisation of both the surface boundary conditions and the convective acceleration terms *[Whitham, 1974; Le Mehaute, 1976]*.

Boussinesq-type equations which are able to describe the non-linear transformation of irregular, multidirectional waves in shallow water have been derived *[Peregrine, 1967]*. Boussinesq equations represent the depth-integrated equations for the conservation of mass and momentum for an incompressible and inviscid fluid. Since the Boussinesq equations include the lowest order effects of frequency dispersion and non-linearity, they can account for the transfer of energy between different frequency components. A major limitation of the commonly used form of the Boussinesq equations is its applicability to only shallow water depths.

There have been several attempts to extend the range of applicability of the Boussinesq equations to deeper water. The dispersion properties of the different forms of the Boussinesq equations have been investigated *[Madsen et al., 1991]*. The authors have introduced a third order term to improve the dispersion properties of the equations. In this form the equations assume a constant water depth, and so are not applicable to shoaling waves.

Recently, a new form of the Boussinesq equation was derived *[Nwogu, 1993]*.

Instead of the usual depth-averaged velocity, the velocity at an arbitrary distance from the still water line was used. This model makes the equation applicable to a wider range of water depths. In addition, the model is able to reproduce several non-linear effects such as the generation of longer- and shorter-period waves, an increase in horizontal and vertical asymmetries and the evolution of wave groups.

Sakai and Battjes [1990] have applied Cokelets numerical non-linear theory for progressive, periodic gravity waves to the two-dimensional shoaling of finite-amplitude waves on a beach. They compared the shoaling curves they obtained with existing models of shoaling curves and with existing experimental data. The shoaling curves obtained from the Cokelets theory show agreement with existing experimental data except in the region of the breakpoint. Near the breakpoint, the Cokelets theory predicts a larger wave height compared to the experimental measurements.

The following conclusions were drawn from an investigation of laboratory shoaling waves *[Flick et al., 1981]*. The harmonic growth of single-frequency plane laboratory waves up to the breakpoint, in the spilling breaker regime, is quantitatively predicted by a third order Stokes theory that conserves energy flux. The non-linear harmonic amplitude changes shoreward of the Stokes regime up to the breakpoint of plunging waves is adequately predicted by cnoidal equations. The Stokes and cnoidal expressions for energy flux, phase speed and the first three harmonic amplitudes have identical functional form to $O(Ur^2)$, in shallow water and in the limit of small Ursell number. Turbu-

lent fluctuations are more important in plunging than in spilling waves.

The modelling of processes in the surf zone is highly complex due to the highly non-linear nature of the processes occurring. In this regard, it is necessary to examine average quantities. The decay of wave energy in the surf zone has been described using an hydraulic jump analogy *[Battjes and Janssen, 1978; Engelund, 1981].*

Undertow and mass flux have been examined by *Svendsen [1984].* The set-down and set-up of the mean water level in the surf comprising plane slope beaches have been successfully described using the concept of radiation stress *[Longuet-Higgins, 1964].*

Research in the modelling of the roller is still an active area *[example, Dally and Brown, 1995].* One of the first empirical estimates of the roller size was made by *Svendsen [1978]* using the experimental data from *Duncan [1981].*

1.3 Existing experimental measurements

The processes occurring in the surf zone are highly non-linear and complete analytical analysis of these processes is difficult. There is thus a definite need for experimentation to provide insight into the physical mechanisms that are involved. Experimental data is also useful in validating mathematical models of surf zone processes. A qualitative description of wave breaking has been provided by *Basco [1985].* This is based on the observation that a con-

tinuous spectrum occurs between the two extremes of a strongly plunging breaker and a weakly spilling breaker, which differ only in the strengths of the vortex systems involved. For the plunging cases, the initial splash from the plunging jet becomes a second plunging jet, creating a second splash. The process repeats itself resulting in as many as five successive vorticies. Each succeeding vortex being weaker than the preceeding one. This process eventually creates much mixing and reduces the organized motion into turbulence. In this description, two key elements were introduced for the first time and these are, a secondary wave disturbance generated by the translation of the plunger vortex and a turbulence mechanism and scale.

Geometrical parameters describing the evolution of both plunging and spilling breakers with frequencies ranging from 1 to 2 Hz have been measured *[Bonmarin, 1989]*. This study concentrated on the evolution of symmetry factors describing the overall shape of the waves and on the surface motion induced by the jet impact in the plunging breakers. In an experiment conducted by *Duncan et al. [1998]*, it was found that the breaking process began with the formation of a bulge near the crest on the forward face of the wave and capillary waves formed upstream of the toe of the bulge. The shape and lengths of these features were found to be nearly independent of wave frequency and wavemaker amplitude. This study led to a formula used to determine the length of surface features in terms of surface tension and the density of water.

Laser Doppler Anemometer (LDA) measurement of undertow in laboratory spilling waves have been conducted by *Stive [1980]* and *Ting and Kirby [1994]*

and in plunging waves by *Ting and Kirby [1994]*. However, measurements were restricted to positions below the trough level, a limitation of the LDA technique. Using a video technique *Govender et al. [2002]* have managed to obtain measurements for positions above the trough level in the crests of spilling and plunging waves breaking on a 1:20 plane slope beach. Video techniques have also been used to study deep water breaking waves *[Perlin et al., 1996]*.

Experimental studies of waves breaking over a submerged bar have been conducted by *Smith and Kraus [1990]*, *Beji and Battjes [1992]* and *Mory [1994]*. *Smith and Kraus [1990]* designed an experiment to measure the macroscale properties of breaking waves on bar and trough beaches. By maintaining a constant water depth (and thus generating relatively high waves), the authors were able to minimize the effect of surface tension and to improve the accuracy of the video tape analysis. Tests were conducted on bar slopes that occur in nature and on steeper slopes. The cases that were tested on the plane slopes fall in the spilling region. One important conclusion was that the gentler, more natural bar slopes permitted spilling breakers to develop while the steeper bar type structures did not.

The aim of the investigation carried out by *Beji and Battjes [1992]* was to determine the role of wave breaking in the nonlinear phenomenon of high frequency energy generation and transfer, occurring in long waves propagating over submerged bars. Some of the conclusions of this investigation follow. Wave breaking occurred over the horizontal crest, there was no breaking be-

fore the shallowest region. The final spectral shape is determined by the redistribution of the total energy among the primary wave and harmonics. The generation of high frequency energy and its transfer is hardly affected by wave breaking which acts merely as a secondary effect.

Laboratory experiments on the breaking of regular waves over a submerged bar were conducted by *Mory [1994]*. His experimental results were based on velocity measurements obtained using a Laser Doppler Anemometer. Measurements of undertow currents were conducted for positions below the effective trough level. The free surface displacements were also measured using resistivity gauges. The power spectra were computed using a Fast Fourier Transform of the time variation of the free surface position and confirmed the occurrence of surface oscillations with higher frequencies. The potential energy was found to decrease rapidly in the breaking zone. It was observed, from the plot of the mean velocity profiles, that a significant mean current exists below the breaking wave. The results were analysed in terms of the momentum flux and the contributions of radiation stress, mean water level set-up and set-down and momentum flux of the mean current were estimated.

The purpose of the present investigation is to reproduce some of the results of *Mory [1994]* [1] and also to provide further insight into the dynamics of that part of the wave above the trough level, as the wave progresses over the bar. Time-averaged estimates of the mass, momentum and energy fluxes over the entire water column above the bottom boundary layer in waves breaking

[1] A copy of this paper is included in the appendix for easy reference.

over a bar are presented. The velocity flow fields at various positions beyond the bar were measured using video imaging and were analysed using digital correlation image velocimetry (DCIV). By tracking the motion of neutrally buoyant particles, as well as bubble structures within the crest of the wave, it was possible to measure velocities well into the crest of the wave. The validation of this measurement technique can be found in *Govender et al. [2002a].* This technique has already provided greater insight into wave breaking on a plane slope beach *[Govender et al., 2002b; Govender et al., 2004].* The instantaneous velocity flow fields were measured at various positions beyond the bar. The time averaged velocities, mass flux and momentum and energy fluxes were then computed.

1.4 Outline of the Thesis

The basic hydrodynamic concepts and definitions are introduced in Chapter 2. Included here are the definitions of mass and momentum flux, as well as radiation stress. The water wave equations and their linear solutions are also presented. Some surf zone processes are reviewed with an emphasis on breaking waves.

A description of the experimental facilities and the diagnostic equipment is given in Chapter 3. The velocity measurement technique is discussed here. A detailed description of an experiment with a rotating disc is given and a sample velocity flow field in breaking waves is also presented.

In Chapter 4 a discussion of the surface elevation measurements ensues. A spectral analysis is conducted and the energy growth in each spectral component is examined. The variation in wave height across the flume and the energy estimates are investigated. The wave profile changes as the wave propagates from deep water to shallow water. A comparison of the wave profile with linear theory and Stokes theory is undertaken in this chapter.

Mass, momentum and energy of a surf zone wave are explored in Chapter 5. The time-averaged velocity flow fields are plotted. The velocities in the crests and the troughs of the waves are investigated, along with the changing profile of the undertow. The discrepancy between the forward and reverse mass fluxes is discussed in relation to the fractional density of the fluid in the crests. The increase in momentum and kinetic energy soon after breaking is also described.

Chapter 6 includes measurements of the roller and aeration areas at various positions beyond the breakpoint. The area computed from the wave gauge measurements of the surface elevation is compared with the area obtained from the analysis of the video images.

Finally, some discussion and conclusions are given in Chapter 7.

Chapter 2

Basic Concepts and Theory

2.1 Introduction

This chapter contains some general mathematical theories necessary for the understanding of waves in fluids. The mathematics associated with deep water waves is described first, followed by an extension to waves in shallow waters and to waves in the surf zone.

The basic equations of water waves are the continuity equation and the Navier-Stokes equation. These equations are obtained by considering mass conservation and the balancing of all the forces acting on a fluid element. The convective acceleration and the friction terms make the Navier-Stokes equation highly non-linear. If the friction forces are negligible, the Navier-Stokes equation reduces to the Euler equation. The Euler equation is still non-linear because of the convective acceleration terms. If the convective acceleration terms are linearised and the boundary conditions are considered,

it is possible to find a linear solution to Eulers equation.

As deep water waves propagate towards a sloping beach, they begin to be slowed down by the slope. Since the energy flux is constant, the reduction in speed results in an increase in the wave height and a decrease in the mean water level, and this is known as set-down. When a critical point is reached, the crest becomes unstable and the wave breaks. This critical point depends on the wave slope and the beach slope. The toppling wave crest results in the formation of a roller that is carried along with the wave. Measurements have been made of some of the properties of surface rollers, in particular, the size of the roller and the energy of the roller.

Due to the highly non-linear nature of waves in shallow water and in the surf zone, it is necessary to use average quantities to describe the relevant processes. The average quantities are described mathematically by depth integrating the equations of motion.

The definition of variables and mathematical preliminaries are discussed in section 2.2, while the equations of water waves and the boundary conditions are described in section 2.3. The linear solution of the equations of water waves is given in section 2.4. Waves in shallow water are described using non-linear theories and the depth integrated equations which are discussed in sections 2.5 and 2.6 respectively. Finally, the processes occurring in the surf zone are described in section 2.7.

2.2 Hydrodynamic Concepts and Definitions

A definition sketch of the coordinate axes and the symbols often used in hydrodynamics is given in Figure 2.1. The x, y, and z axes form a right-handed co-ordinate system with the positive x-axis pointing in the direction of wave propagation. The velocity components in the x, y and z directions are denoted by u, v and w respectively. The still water line (swl) is the level of the water in the absence of waves. The distance between the bed and the swl is represented by d, while η represents the displacement of the water surface relative to the swl. The wave height, which is the vertical distance between the crest and the trough, is denoted by H.

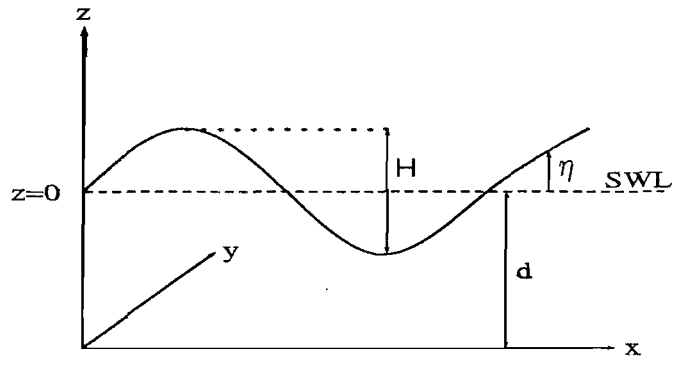

Figure 2.1: *Definition sketch of coordinates axes and wave parameters.*

The components of the velocity in the x, y and z directions of a water particle located at (x, y, z) will be denoted by $u(x, y, z, t)$, $v(x, y, z, t)$ and $w(x, y, z, t)$

respectively. The acceleration is then given by

$$\mathbf{a} = \frac{d\mathbf{u}}{dt} = \frac{d[u(x,y,z,t), v(x,y,z,t), w(x,y,z,t)]}{dt}. \tag{2.1}$$

Expanding the right hand side of equation 2.1 results in

$$\mathbf{a} = \frac{\partial \mathbf{u}}{\partial t} + \frac{\partial \mathbf{u}}{\partial \mathbf{x}} \frac{d\mathbf{x}}{dt} \tag{2.2}$$

where $\mathbf{u} = (u, v, w)$ and $\mathbf{x} = (x, y, z)$. Thus the total acceleration $\mathbf{a}$ of a fluid element is the sum of the local and the convective acceleration terms. The local acceleration is the change of velocity with respect to time at a fixed point in space (first term on RHS of equation 2.2), while convective acceleration is the change in velocity with respect to change in position (second term on RHS of equation 2.2).

2.3 Equations of Water Waves

The basis of theoretical fluid dynamics rests on the mechanics of an elementary mass of fluid. In this case several assumptions are made and these are; that the fluid element is either infinitely small or small enough that all parts of the element can be considered to have the same velocity of translation $\mathbf{u}$ and the same density ρ, that the fluid is homogeneous, isotropic and continuous in the macroscopic sense and that the molecular pattern and the molecular and Brownian motions within the particle are negligible.

The equations of water waves are based on the conservation of mass and momentum together with the description of the pressure and the boundary

conditions. These are discussed below.

Continuity

Consider an imaginary surface in the form of a cube lying within a fluid as shown in Figure 2.2. Let u=u(x, y, z, t), v=v(x, y, z, t) and w=w(x, y, z, t) be the components of the velocity $\mathbf{u}$ of a fluid element which at time t is situated at the point (x, y, z). For a one dimensional motion in the x-direction, the difference between the rate of mass entering through edge abcd and the rate of mass leaving through edge efgh is equal to the rate of mass accumulating within the cubic volume. This law of conservation of mass in a given space occupied by a fluid is known as the continuity principle. In general, for a three dimensional motion the continuity equation for a fluid of constant density is given by

$$\nabla.\mathbf{u} = 0 \tag{2.3}$$

which means that there are no sources or sinks within the fluid.

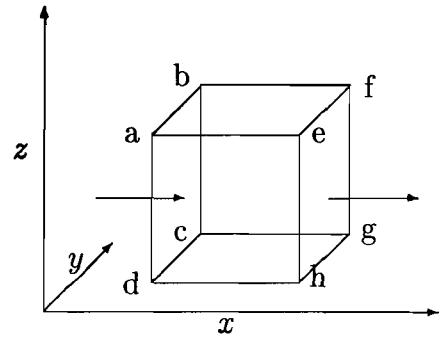

Figure 2.2: *Schematic illustrating one dimensional fluid motion through an imaginary surface in the form of a cube.*

Momentum

By applying Newtons' second law to the cubic volume, and employing a co-ordinate system as shown in Figure 2.1, we obtain the Navier-Stokes equation

$$\rho\left(\frac{\partial \mathbf{u}}{\partial t} + \mathbf{u}\nabla.\mathbf{u}\right) = -\nabla\left(p + \rho g z\right) + \mu\nabla^2\mathbf{u} \tag{2.4}$$

where μ is the viscosity and p is the dynamic pressure associated with the wave motion. The Navier-Stokes equation is non-linear because of the convective acceleration and the viscosity terms.

Pressure

The pressure at any point in the fluid is given by

$$p = p^{+} - \rho g z \tag{2.5}$$

where p^{+} is referred to as the dynamic pressure and it is the pressure over and above hydrostatic pressure due to the mean water level.

Boundary conditions

In the study of waves on a free surface we have the following boundary conditions *[Fredsoe and Deigaard, 1992]*

1. At the bed the flow velocity perpendicular to the bed is zero. For a plane horizontal bed this gives

$$w = 0 \quad \text{for } z = -d \tag{2.6}$$

2. A fluid particle at the free surface must remain at the free surface giving

$$w = \frac{d\eta}{dt} \quad \text{for } z = \eta \tag{2.7}$$

3. The pressure at the surface must be equal to atmospheric pressure and can be set to zero.

2.4 Linear Solution

It is not possible to find a general solution to the Navier-Stokes equation due to the non-linear nature of the viscous forces and the convective acceleration term. However, by neglecting the viscous term and by linearizing the convective term it is possible to obtain a linear solution *[Le Mehaute, 1976]*.

An alternate approach is to assume that the viscous forces are negligible and to use the irrotational property of the fluid. If the flow is irrotational, that is, $\nabla \times \mathbf{u} = 0$ then there exists a potential function ϕ such that $\mathbf{u} = -\nabla\phi$. In this particular case the potential function can be shown to be *[Le Mehaute, 1976]*

$$\phi = -\frac{H}{2}\frac{\omega}{k}\frac{\cosh k(d+z)}{\sinh(kd)}.\cos(\omega t - kx) \tag{2.8}$$

where H is the height of the wave, ω is the wave frequency in radians, k is the wave number and d is the local water depth.

By using $\mathbf{u} = -\nabla\phi$ we obtain the following expressions for the particle velocities

$$u = \frac{H\omega}{2}\frac{\cosh k(d+z)}{\sinh(kd)}.\sin(\omega t - kx) \tag{2.9}$$

and

$$w = \frac{H\omega}{2}\frac{\sinh k(d+z)}{\sinh(kd)}.\cos(\omega t - kx) \tag{2.10}$$

where u and w are the velocities in the x and z directions respectively.

Using the above expressions for u and w, it is possible to determine the orbit of each particle. The particle orbits in deep water are shown in Figure 2.3. The water particles move in nearly circular vertical orbits as the waves pass. The radius of the orbits of each particle decreases with water depth. At a depth corresponding to half a wavelength or more, the effect of a surface wave is minimal as shown in Figure 2.3. The diameter of the orbit of a particle on the surface is equal to the wave height.

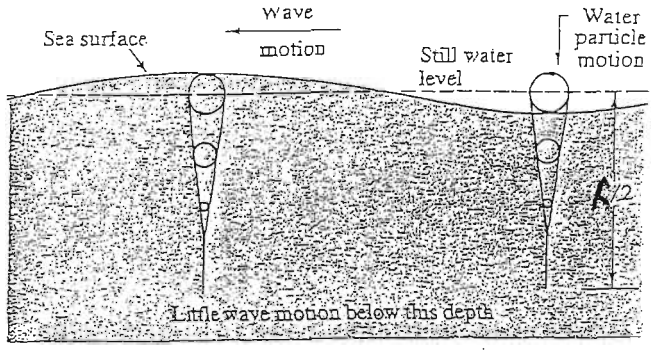

Figure 2.3: *Particle orbits in deep water [Oceanography, 1990].*

The particle orbits change when the waves move into shallow water. Figure 2.4 depicts the particle orbits in shallow water. Water particles move in flattened elliptical orbits that are flat near the bottom and almost circular near the surface.

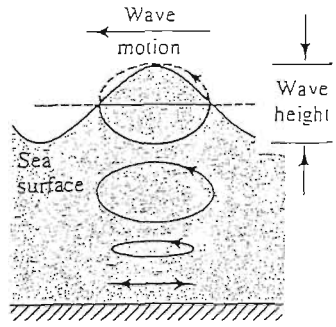

Figure 2.4: *Motions of water particles in shallow-water waves [Oceanography, 1990].*

It can also be shown that the expression for pressure is given by

$$p = \rho g \frac{H}{2} \frac{\cosh(kz)}{\cosh(kd)} \sin(\omega t - kx). \tag{2.11}$$

The dispersion relation

The property that waves of different wavelengths travel at different speeds is known as dispersion. If the wave speed is independent of direction, the system is said to be isotropic. From the linear solution of the equations of water waves it is also possible to find the dispersion relation. In this case ω and k are related by

$$\omega^2 = g\, k\, \tanh(kd) \tag{2.12}$$

where g is the acceleration due to gravity and d is the still water depth.

The dispersion relation as given in equation 2.12 is general and applies to waves in deep water as well as in shallow water. Two approximations exist and these are the deep water approximation where $d >> \lambda$ to give

$$\omega^2 = g\,k \qquad (2.13)$$

since $kd >> 1$ so that $\tanh(kd) \approx 1$, and the shallow water approximation where $d << \lambda$ and

$$\omega^2 = g\,k^2 d \qquad (2.14)$$

since $kd << 1$ and $\tanh(kd) \approx kd$.

Figure 2.5 illustrates the relationship between the wave speed c and the wavelength λ for fixed water depths h. In the range between $3.5h$ and $14h$, the dependence of c on λ as given by

$$c = \left(\frac{g\lambda}{2\pi}\right) \tanh\left(\frac{2\pi h}{\lambda}\right) \qquad (2.15)$$

deviates significantly from both its limiting forms. The graph makes a smooth transition between the 'parabolic' limiting form $(g\lambda/2\pi)^{\frac{1}{2}}$ for $\lambda < 3.5\,h$ and the constant asymptote $(gh)^{\frac{1}{2}}$ for $\lambda > 14\,h$ *[Lighthill, 1978].*

The phase velocity

The phase velocity is the speed at which a particular phase of the wave propagates and is defined as

$$c_p = \frac{\omega}{k} \qquad (2.16)$$

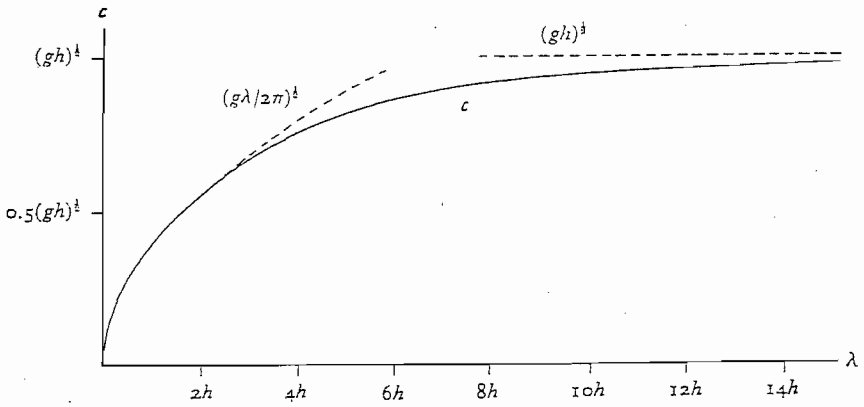

Figure 2.5: *Wave speed c for waves of varying wavelength λ on water of uniform depth h [Lighthill, 1978].*

which can be written as

$$c_p = \frac{g}{k} \tag{2.17}$$

in deep water by the use of equation 2.13 and as

$$c_p = \sqrt{g\,d} \tag{2.18}$$

in shallow water by the use of equation 2.14.

In deep water, the wave speed is determined by the wavelength. In shallow water, the wave speed is controlled by water depth, that is, there is no dispersion. In deep water, waves of longer wavelengths travel faster than those of shorter wavelengths.

The group velocity

In general, an ocean wave does not exist on its own, but is made up of a

group of waves of different lenghts, each travelling at its own speed. This results in the profile of the group shifting constantly. The group velocity is the velocity at which a group of waves travels and is defined as

$$c_g = \frac{\partial \omega}{\partial k} \tag{2.19}$$

where $\partial\omega$ is the change in wave frequency and ∂k is the change in wave number. Using equation 2.12 in equation 2.19 results in

$$c_g = \frac{g}{2\omega} \tag{2.20}$$

in deep water and

$$c_g = \sqrt{g\,d} \tag{2.21}$$

in shallow water. It is worth noting that the phase velocity in deep water is twice the group velocity, while in shallow water they are the same.

The energy equations

The energy of a wave comprises potential energy and kinetic energy. Potential energy arises because water below the mean water level is moved above the mean water level. The energy equations are determined by assuming a sinusoidal wave profile. The potential energy is evaluated from

$$E_p = \frac{1}{\lambda}\int_0^{\lambda}\left(\int_0^{\eta} \rho g z\, dz\right) dx \tag{2.22}$$

and the kinetic energy is evaluated from

$$E_k = \frac{1}{\lambda}\int_0^{\lambda}\left(\int_{-d}^{\eta} \frac{1}{2}\rho(u^2 + w^2)\, dz\right) dx \tag{2.23}$$

where η represents the free surface displacements, H is the wave height and u and w are the particle velocities in the x and z directions respectively. Using the result from the linear solution to the equations of water waves in the above equations, results in the following expressions for the potential and kinetic energies

$$E_p = \frac{1}{16}\rho g H^2 \tag{2.24}$$

$$E_k = \frac{1}{16}\rho g H^2 \tag{2.25}$$

which gives a total energy of

$$E = \frac{1}{8}\rho g H^2. \tag{2.26}$$

The above formula gives the energy per unit horizontal area. The property that the kinetic and potential energies are equal is known as equipartition of energy. The energy is transported at the group velocity in the direction of wave propagation.

2.5 Non-Linear Wave Theories

As waves migrate from deep water into shallow water they undergo several transitions. These changes are largely due to the influence of the bottom boundary as the water depth decreases. Linear shallow water wave theory is inaccurate near the breaking point. In this region the waves are more peaked at the crests and more flattened at the troughs than a sine wave. This significant deviation from the sinusoidal prediction of linear theory makes it

necessary to employ non-linear theories such as Stokes theory or cnoidal theory which give a better prediction of the waves profile than does first order linear theory.

"*Stokes (1847)* showed that the surface elevation η in a plane wave-train on deep water could be expanded in powers of the amplitude a as *[Whitham, 1974]*

$$\eta = a\cos(kx - \omega t) + \frac{1}{2}ka^2\cos 2(kx - \omega t) + \frac{3}{8}k^2a^3\cos 3(kx - \omega t) + ... \tag{2.27}$$

where

$$\omega^2 = gk(1 + k^2a^2 + ...). \tag{2.28}$$

The linear result would be the first term in equation 2.27 and the dispersion relation would be

$$\omega^2 = gk.$$

Korteweg and deVries (1895) showed that long waves in relatively shallow water could be described approximately by a non-linear equation of the form[1]

$$\eta_t + (c_0 + c_1\eta)\eta_x + \nu\eta_{xxx} = 0 \tag{2.29}$$

where c_0, c_1 and ν are constants. In addition, they showed that periodic solutions

$$\eta = f(\theta), \qquad \theta = kx - \omega t$$

[1]Subscripts here denote partial differentiation, i.e. $\eta_x = \frac{\partial\eta}{\partial x}$, $\eta_{xxx} = \frac{\partial^3\eta}{\partial x^3}$ and $\eta_t = \frac{\partial\eta}{\partial t}$

of equation 2.29 could be found in terms of the Jacobian elliptic functions. Since $f(\theta)$ was found in terms of the elliptic function $\mathrm{cn}\theta$, the solutions were named *cnoidal* waves" *[Whitham, 1974].*

2.6 Depth Integrated Equations

Due to the difficult nature of waves in the surf zone, it is necessary to investigate average quantities. A description of some important averaged quantities such as mass flux, momentum flux, radiation stress and energy flux follows.

The mass flux in the horizontal direction is given by

$$M = \int_{-d}^{\eta_{crest}} \rho \overline{u(z)}\, dz \tag{2.30}$$

and the momentum flux is given by

$$F = \int_{-d}^{\eta_{crest}} \rho \overline{u(z)}^2\, dz \tag{2.31}$$

where ρ is the fluid density, η_{crest} is the crest position and $-d$ is the position of the bed relative to the swl. The overbar denotes time averaging.

Radiation stress is defined as the excess flow of momentum due to the presence of waves *[Longuet-Higgins and Stewart, 1964].* The principal component of radiation stress in the direction of wave propagation is the difference between the time-averaged total momentum flux in the presence of waves and the mean momentum flux in the absence of waves. For waves propagating in

the x-direction, the principal component of the radiation stress is given by

$$S_{xx} = \overline{\int_{-d}^{\eta} (p + \rho u^2)\, dz} - \int_{-d}^{0} p_o\, dz \tag{2.32}$$

where p is the pressure and p_o is the atmospheric pressure.

For the case of linear waves, the radiation stress in the x-direction is

$$S_{xx} = E\left(\frac{2kh}{\sinh(2kh)} + \frac{1}{2}\right) \tag{2.33}$$

where E is the energy of the wave, k is the wave number and h is the local water depth. This relation reduces to

$$S_{xx} = 0.5\,E \quad \text{in deep water} \tag{2.34}$$

$$S_{xx} = 1.5\,E \quad \text{in shallow water} \tag{2.35}$$

for waves propagating in the x-direction, and the other components of the radiation stress tensor are

$$S_{yy} = 0 \quad \text{in deep water} \tag{2.36}$$

$$S_{yy} = 0.5\,E \quad \text{in shallow water} \tag{2.37}$$

$$S_{xy} = 0. \tag{2.38}$$

The relationship between the mean water level and the radiation stress is given by

$$\frac{d\overline{\eta}}{dx} = -\frac{1}{\rho g(d + \overline{\eta})} \cdot \frac{dS_{xx}}{dx} \tag{2.39}$$

where d is the still water depth, $\overline{\eta}$ is the mean water level relative to the still water line and S_{xx} is the principal component of the radiation stress. This

equation expresses balance between the pressure force from the slope of the mean water surface and the gradient of the radiation stress.

The dissipation of energy in the surf zone and the associated decrease in wave height towards the shore result in a gradient in the radiation stress. The decrease in radiation stress is balanced by a slope of the mean water surface, the set-up. The magnitude of the set-up can be determined by the horizontal component of the momentum equation *[Fredsoe and Deigaard, 1992]*.

The energy equation expresses the variation in energy flux, E_f, with respect to horizontal distance and is given by

$$\frac{dE_f}{dx} = -\overline{D} \tag{2.40}$$

where $\overline{D}$ is the mean energy dissipation rate per unit bed area.

The pressure equation is

$$\overline{P}_b \frac{dd}{dx} - \rho g(d+\overline{\eta})\frac{d\overline{\eta}}{dx} - \frac{dS_{xx}}{dx} - \overline{\tau}_b = 0 \tag{2.41}$$

where $\overline{P}_b$ is the mean dynamic pressure on the bottom surface, $\overline{\tau}_b$ is the mean shear stress at the bottom and

$$S_{xx} = \int_{-d}^{\eta_c} (\overline{P} + \rho\overline{u^2})dz + \frac{1}{2}\rho g\overline{(\eta - \overline{\eta})^2} \tag{2.42}$$

where η_c is the level of the wave crest and the overbar denotes time averaging.

2.7 Surf Zone Processes

An illustration of the changes that occur when deep water waves propagate towards a sloping beach is given in Figure 2.6. As the waves enter shallow water, their wave speed decreases and there is an increase in wave height, and this is known as "shoaling". During shoaling, there is also a corresponding decrease in the mean water level, and this is known as "set-down". The wave height continues to increase until at some critical point, the wave collapses and this is called "wave breaking", which is accompanied by an increase in the mean water level, a process known as "set-up".

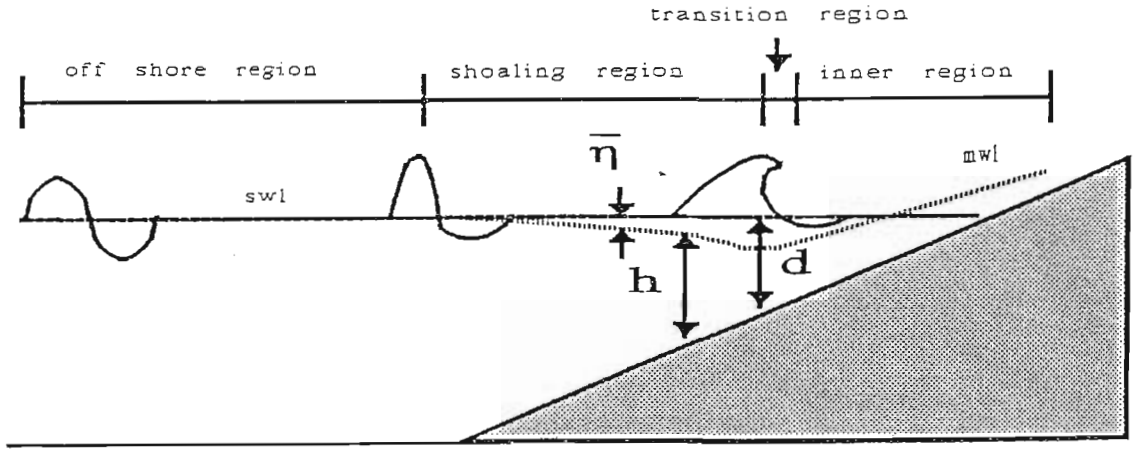

Figure 2.6: *Schematic of shoaling, wave breaking, setdown and setup of the mean water level as taken from [Govender, 1999].*

In addition to the symbols already discussed, the following symbols relevant to the surf zone are defined: $\overline{\eta}$ denotes the mean water level relative to the still water line and h denotes the mean local water depth. Variables with a

subscript o denote conditions off-shore while those with a subscript b denote conditions at the break point.

Wave breaking

As deep water waves approach a sloping beach, several transitions occur. The bottom surface influences orbital water-particle motions. Although the wave period remains unchanged, the wavelength is shortened and the wave speed decreases. This causes the wave height to increase and the wave crests to become more peaked. The wave steepness (H/λ) increases until it reaches a critical value. At this point, the wave crests peak sharply, become unstable and break.

Wave breaking may be characterised by the wave steepness and the beach slope in a dimensionless surf similarity parameter ξ given by *[Battjes,* 1974*]*,

$$\xi = \frac{\tan\beta}{\sqrt{\frac{H_o}{\lambda_o}}} \tag{2.43}$$

where λ_o is the wavelength, H_o is the wave height and β is the beach slope. Wave breaking occurs when the ratio of wave height to wavelength exceeds 0.142.

Conventionally, waves that collapse to induce the process of wave breaking are called breakers. Three types of breakers are distinguished by use of ξ and these principal types are depicted in Figure 2.7 *[Galvin, 1968]*. The first one is a "collapsing breaker" in which only the lower portion of the front face becomes vertical and plunges forward. The wave crest is unbroken and

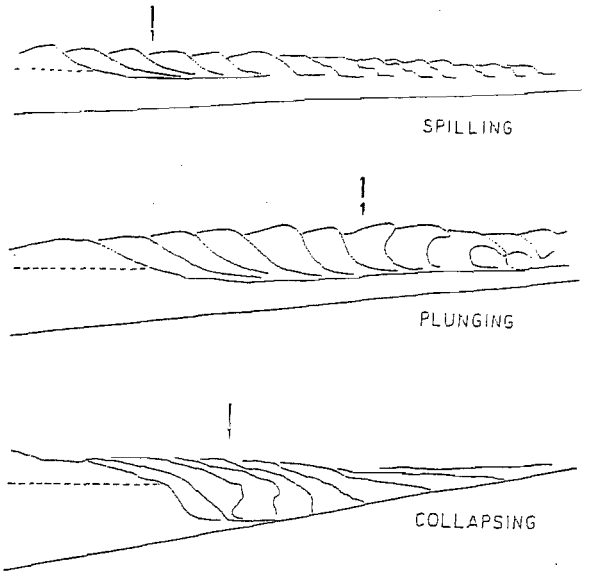

Figure 2.7: *Principal breaker types, with the swl indicated by the dashed line and the breaking point denoted by the arrow [Galvin, 1968].*

collapses onto the base of the wave. The second is a "plunging breaker" and this is one in which the crest of the wave curls forward and forms a jet that plunges into the trough ahead. The third is a "spilling breaker", where the trough ahead is not visibly disturbed as the fluid near the top of the crest slides down the front face of the wave. In addition to the above, waves that do not break are termed surging breakers.

Wave rollers

When the wave breaks, the tip of the crest falls onto the front face of the wave forming a body of water that rides on the wave face. This body of water is called a roller. Figure 2.8 shows a roller on the front face of a wave. The roller moves in the direction of wave propagation with a speed corresponding to the phase speed. This results in a transport of mass in the forward direction.

In order to undertake a full momentum balance it is necessary to determine the cross sectional area of the roller. The cross sectional area is also needed to calculate the energy of the roller.

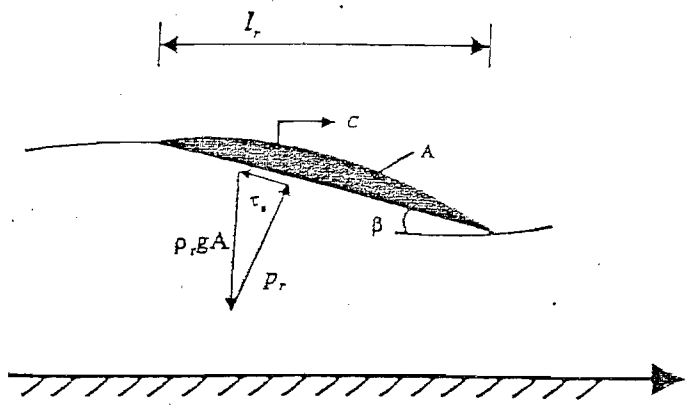

Figure 2.8: *Schematic of a wave roller and the forces acting on it. l_r is the length of the roller, α_o is the roller slope, P_r is a pressure force, T_r is a shear force on the surface between the roller and the water below, $\rho g A$ is the force of gravity and c is the wave speed [Mocke, 1998; Fredsoe and Deigaard, 1992].*

Empirical estimates of the roller area were first made by *Duncan [1981]* and using his results *Svendsen [1984]* formulated the following relation

$$A = 0.9H^2. \tag{2.44}$$

The energy flux of the roller E_r, is given by *[Svendsen, 1984]*

$$E_r = \frac{A}{2\lambda}\,\rho\, c^3 \tag{2.45}$$

where ρ is the fluid density, c is the wave propagation speed, A is the area of the roller and λ is the wavelength.

The mean momentum flux due to the roller is

$$F_r = \rho\, c\frac{A}{T} \tag{2.46}$$

where T is the wave period.

The minimum and maximum aeration areas have been estimated *[Govender, 1999]* for several positions in the surf zone for spilling and plunging waves. The normalised area for the spilling case spans a range of 0.5 to 1.5 and is almost evenly distributed about the $\frac{A}{H^2} = 0.9$ line. The normalised area for the plunging case shows an increasing trend and is greater than 0.9 for the major part of the surf zone.

The wave roller slope has been estimated near the break point and further in the surf zone by Govender (1999). His findings are tabulated below.

	Break Point	Surf Zone
Spilling wave	$\approx 30^o$	$\approx 15^o$
Plunging wave	$\approx 40^o$	$\approx 15^o$

Table 2.1. Wave roller slope for plunging and spilling waves.

Currents

In the surf zone there is an onshore flow of water due to two mechanisms,

firstly the wave drift and secondly due to the transport of the surface roller. Since there is no build up of water on the shore, there has to be a current in the offshore direction. This return current has its maximum near the bed and is called the undertow. Figure 2.9 is an illustration of the profile of the undertow. This picture is for the case of waves breaking over a bar in the surf zone but applies to the undertow in general.

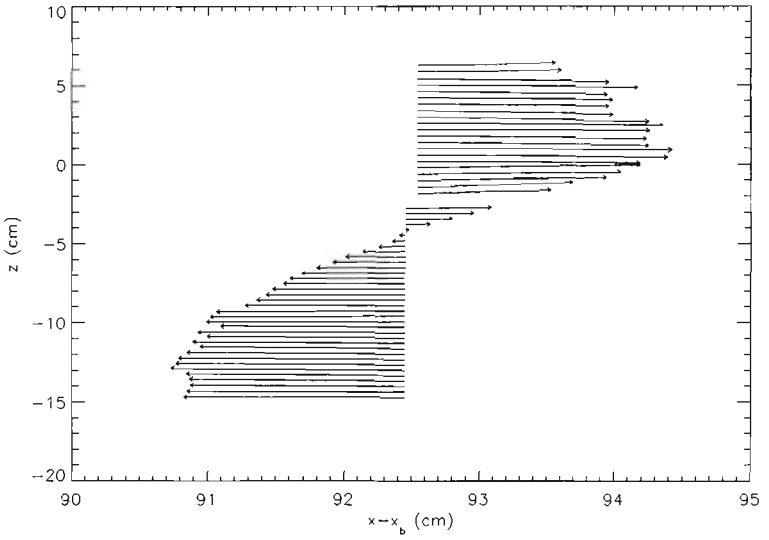

Figure 2.9: *Typical profile of undertow and forward current. This is a sample measurement taken from waves breaking over a bar. See section 5.3.2 for more details.*

2.8 Summary

In this chapter we have introduced the basic hydrodynamic concepts and discussed the theory of water waves. The relevant water wave equations, particle velocities, the dispersion relation, phase and group velocities and

the energy and pressure equations have been reviewed. The need for non-linear wave theories has been explained briefly. Depth-integrated quantities such as radiation stress, energy flux and pressure have been discussed. The surf zone has been discussed in great detail. The criteria for wave breaking have been reviewed and the beach slope and wave slope are shown to be important factors. Plunging, spilling and collapsing breakers have also been discussed. Wave roller properties such as energy, slope, area and momentum flux have also been discussed.

Chapter 3

Experimental Procedure

3.1 Introduction

Using video imaging and analysis techniques, waves breaking over a bar in a laboratory surf zone were investigated. The experimental work was conducted by M.J. Alport and K. Govender during January-February 2000 in France. A digital camera was used to image the wave and the aeration. The images were stored on video tape. In this chapter, a description of the experimental setup and the measurement of the surface elevations and the velocity vector fields are described.

The free surface displacements were measured using resistive wave gauges. The signal from the gauges was recorded onto the audio channel of a video casette recorder (VCR). The signal from the VCR was recovered and captured using a digital storage oscilloscope.

The velocity vector fields were measured using the digital correlation image velocimetry (DCIV) technique. The fluid velocity is estimated by tracking the displacement of a small region of seeded and aerated flow over a known time interval. Instantaneous flow fields were measured over three different sampling times. At each measurement position, the wave was imaged at twelve equally spaced phases.

To demonstrate familiarity with and the limitations of the CIV measurement procedure, an experiment was conducted to determined the velocity of points on a rotating disc. The experimental setup was similar to the one used to determine the flow fields, except that instead of a light sheet a stroboscope was placed in front of the disc. The velocity of the disc was also determined by a second method. There was good agreement between the two sets of results.

3.2 Wave Flume and Wave Conditions

Experiments on regular two dimensional waves breaking over an artificial bar were conducted in a glass walled flume, located in the Laboratoire de Mecanique des Fluides, Grenoble, France. The flume was 17 m long, 0.8 m wide and 0.8 m high. The flume was fitted with a bar-type bottom topography. A schematic of the bar profile is given in Figure 3.1. The bar, which was placed 8.2 m from the wave maker, had a 600 cm upslope (1:20), a 10 cm horizontal crest, a 70 cm downslope (1:10) and a 2 m horizontal section. A photo showing the bar profile is given in Figure 3.2. At the end of the bar

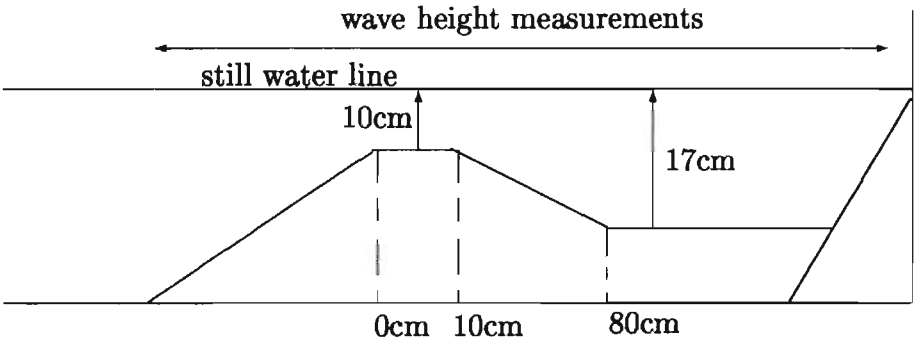

Figure 3.1: *Schematic of bar profile.*

Figure 3.2: *Close-up view of the flume showing the bar profile. a, b and c denote the upslope, the horizontal crest and the downslope, respectively.*

was a beach absorber. The still water depth in the section between the wave maker and the bar was 40 cm, at the crest it was 10 cm and in the horizontal section beyond the downslope it was 17 cm.

Figure 3.3: *Overall view of the wave flume.*

Figure 3.3 gives an overall view of the wave flume. Regular sinusoidal waves of period $T = 1.5$ s were produced by a piston type wave maker. The piston paddle was attached to a drive, which in turn was connected, off-center, to a drive disc. The wave frequency could be changed by varying the speed of the drive disc. A picture of the piston paddle is given in Figure 3.4 and the drive disc is shown in Figure 3.5. The wave height in the deep water section of the flume was 7.4 cm.

Figure 3.4: *Photo of the piston paddle. The piston is driven by a beam (black in photo) which is attached to a disc driven by a motor.*

Figure 3.5: *Photo of the disc drive. The wave frequency is varied by changing the speed of the disc.*

3.3 Surface Wave Measurements

The free surface displacement, corresponding to the surface waves, was measured using resistive and capacitive wave gauges. In this thesis only the measurements from the resistive wave gauges are considered. A picture of a resistive wave gauge is given in Figure 3.6. The gauges were attached to a trolley that could be translated on a pair of rails located above the flume walls. Figure 3.7 shows a top view of the flume and clearly shows the rails, trolley and wave gauges. A side view of the flume depicting the suspended gauges is shown Figure 3.8. The signal measured with the gauges was modulated onto a 600 Hz carrier wave before being recorded onto the audio channel of the VCR. The wave was also video recorded at the position where the gauges were located.

The signal from the audio channel of the VCR was recovered as follows. The signal from the audio channel was applied to a demodulating circuit. The output voltage of the demodulating circuit (that is, the measured signal) was applied to a digital storage oscilloscope (DSO). Commercially available software, WaveStar, was used to record 30 wave cycles, at each measurement position. WaveStar was also able to download the recordings of the time and voltages to a personal computer in the format of a text file. Calibration of the wave gauge will be discussed in Chapter 4.

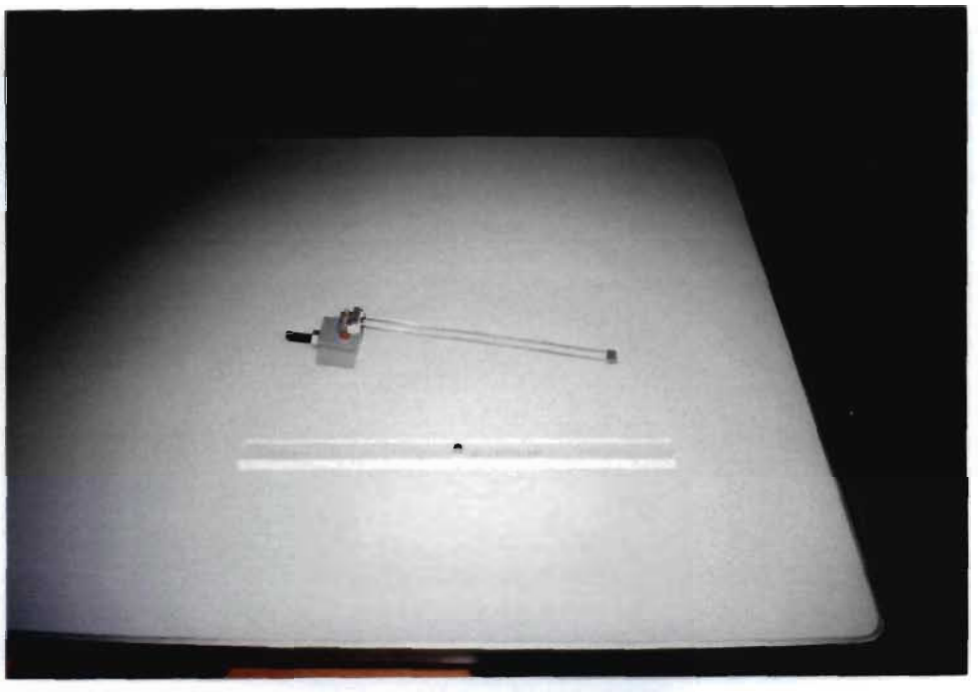

Figure 3.6: *Photo of a resistive wave gauge. Alongside the gauge is a 50 cm ruler.*

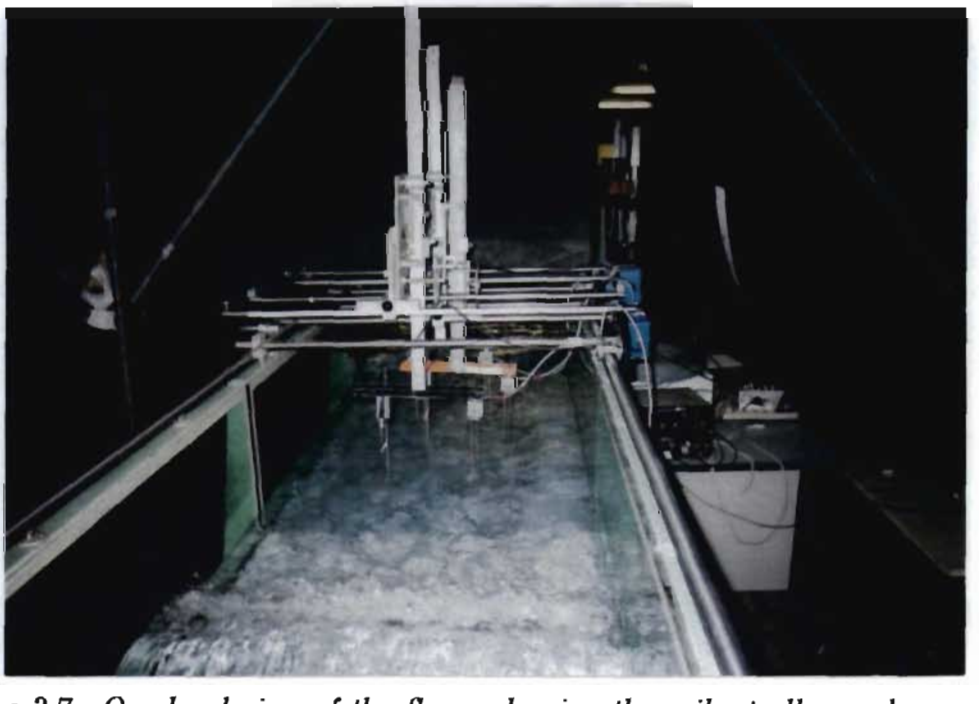

Figure 3.7: *Overhead view of the flume showing the rails, trolley and wave gauges.*

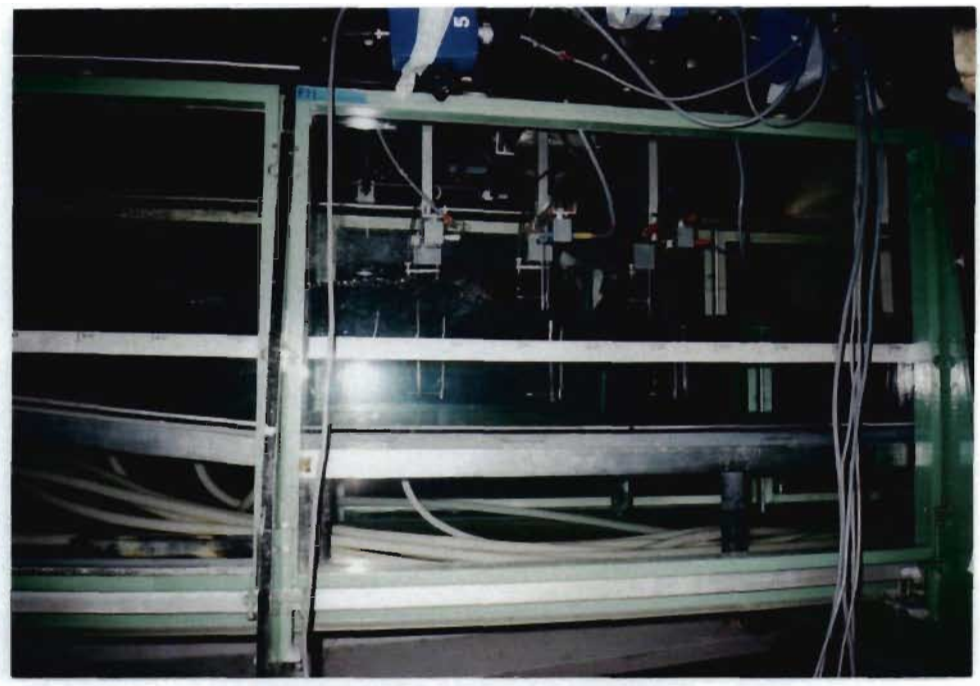

Figure 3.8: *Side view of the flume showing the suspended wave gauges.*

3.4 Velocity Measurements

The velocity vector field of the wave was measured using a technique known as digital correlation image velocimetry (DCIV). The fluid velocity is estimated by tracking the displacement of a small region of seeded and aerated flow over a known time interval. A description of the experimental setup follows. A longitudinal section of the flume was illuminated with a strobed light sheet and the aeration and illuminated particles were imaged using a progressive scan CCD camera connected to a frame grabber residing in a personal computer. Figure 3.9 illustates the experimental setup of the DCIV apparatus. Two video images of the aerated and seeded flow are captured.

The instantaneous velocity field is obtained as follows. An interrogation win-

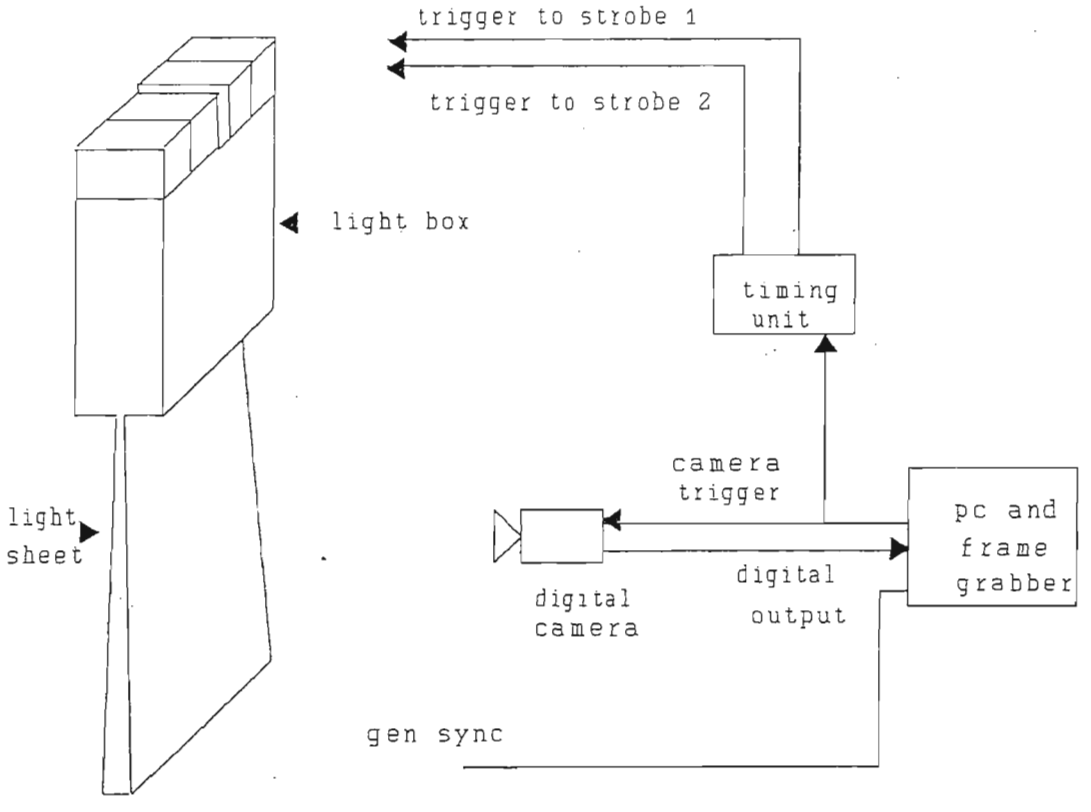

Figure 3.9: *Experimental setup of the DCIV apparatus [Govender, 1999].*

dow, of size 24x24 pixels, is placed at the bottom left corner of the image. The sub-image within the interrogation window is then cross-correlated with the corresponding sub-image in the second image. The position of the peak in the cross-correlation is a measure of the displacement of the structure in the second sub-image with respect to that in the first. The velocity at the location of the interrogation window is then obtained by dividing the displacement of the structure in the sub-images by the time interval between the images. The interrogation window is then moved horizontally and vertically in steps of six pixels and the above procedure is repeated. The computation of the cross correlation is implemented in the frequency domain. More details of the experimental setup, imaging and computational procedures can be found in *Govender et al. [2002a]* and *Govender [1999].*[1]

Instantaneous velocity flow fields were measured using three sampling times, namely, 1, 5 and 10 ms. Since the camera is capable of imaging only a 30 cm section of the wave in order to provide an acceptable spatial resolution, the wave had to be imaged in sections. The camera and computer were setup to measure a 30 cm section of the flow field of the wave at four positions along the flume, namely, 10-40 cm, 40-70 cm, 90-120 cm and 130-160 cm beyond the break point. A TTL trigger signal obtained from the wave generator made it possible to capture an image at a particular phase at each position. A sample of an image of the crest of a wave at the first measurement position is given in Figure 3.10.

[1]The relevant chapter from *Govender [1999]* describing the video measurement technique is included in the appendix.

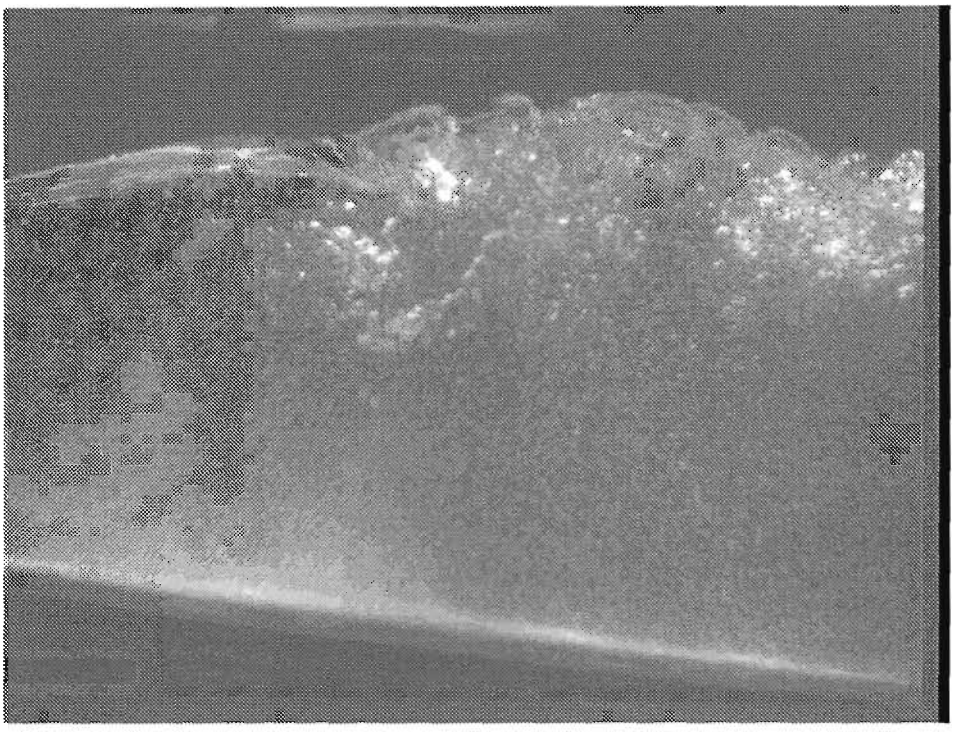

Figure 3.10: *Image of the crest of a wave showing neutrally bouyant particles and aeration. This image is one from a pair of images spaced* 1 *ms apart and captured at* $10 - 40$ *cm beyond the bar crest.*

Fifty images at this phase position were captured for each sampling time, resulting in 150 images. These 150 images were then processed to yield 150 instantaneous velocity vector fields. The vector field corresponding to the image in Figure 3.10 is shown in Figure 3.11. Averaging operations on these instantaneous vector fields then yielded phase-ensemble-averaged velocities, kinetic energy, momentum, etc. In Figure 3.11 there are isolated regions where no velocity measurements are available, due to a lack of correlated seed or aeration structures between the pair of images. Thus, not all 150

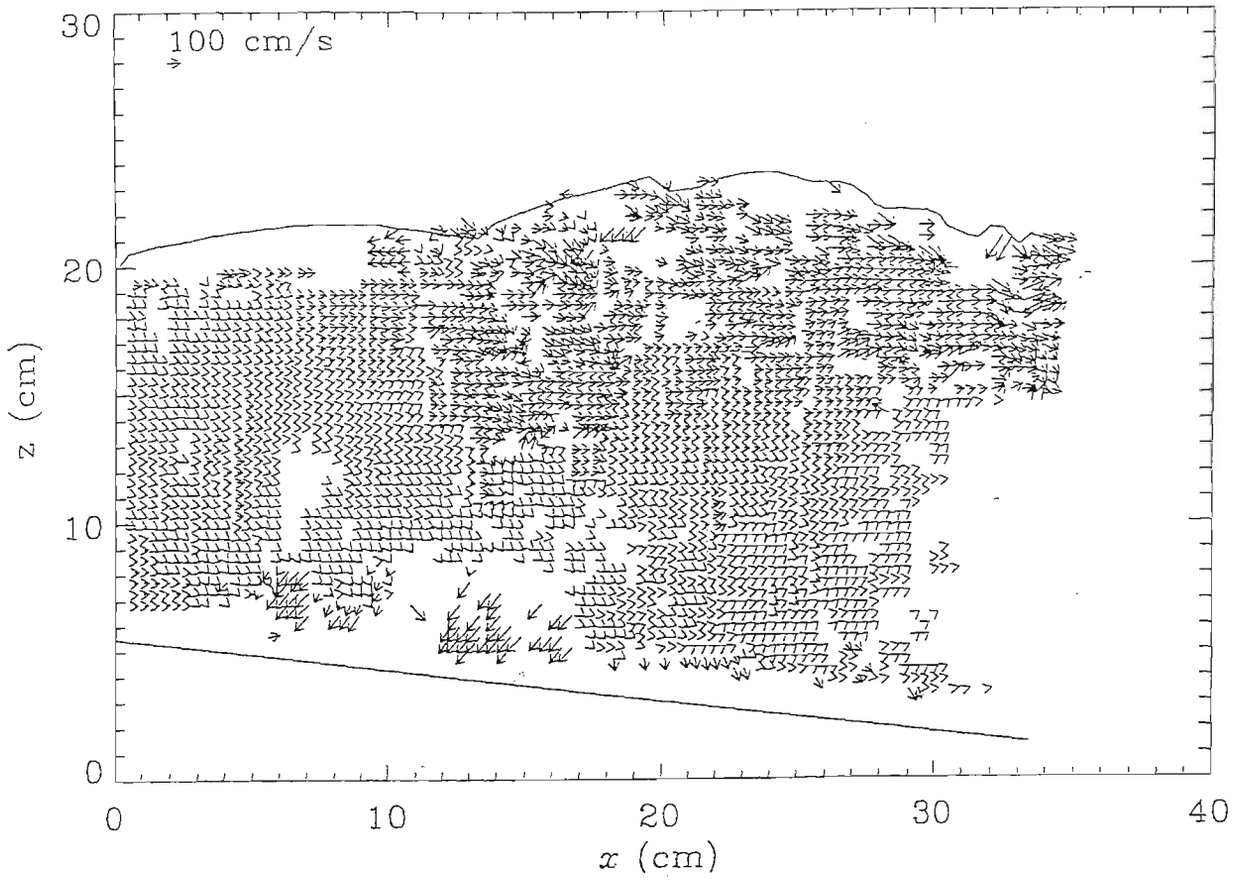

Figure 3.11: *Velocity vector field corresponding to Figure 3.10.*

ages result in a velocity vector at a given point in the image. Each quantity in the phase-ensemble-averaged fields were estimated using 30 to 50 instantaneous velocity vectors. The trigger delay was then adjusted to capture images of the wave at the same position along the flume, but corresponding to a different wave phase. For each measurement position the wave was imaged at twelve equally spaced phases. The measurements at each position were done in two stages. The first set of measurements were conducted with the light sheet located approximately 10 cm from the glass wall. The second set of measurements were conducted with the light sheet located ap-

proximately 25 cm from the glass wall. The vector fields corresponding to positions above the trough level from the near wall measurements were then combined with the vector field corresponding to positions below the trough level from the inner measurements. This procedure is necessary to utilise the aeration structures in the crests of the waves to obtain the vector field. With the light sheet located further away from the glass wall, images of the turbulent structure are obscured by aerated fluid in front of the light sheet. The velocity vectors corresponding to positions below the trough level from the near wall measurements were discarded as they may be contaminated by boundary layer effects. In the crest of the wave the boundary layer is much thinner due to the oscillatory nature of the flow and the intermittent contact of fluid with the glass at a given position, thus resulting in minimal boundary layer effects at the position where the light is located.

3.5 Velocity Measurements from Rotating Disc

In order to demonstrate familiarity with and limitations of the CIV measurement procedure, an experiment to determine the velocity of points on a rotating disc was conducted. A pattern of a black background with randomly spaced white dots, was pasted onto a rotating disc. A picture of the disc with this pattern is given in Figure 3.12. Two images of the rotating disc were obtained using the setup described in the previous section, except that a light sheet was not used, rather a stroboscope was placed in front of the disc. A sampling time (time between capture of images) of 1.08 ms was used. In order to convert from image pixels to centimeters, a calibration factor was

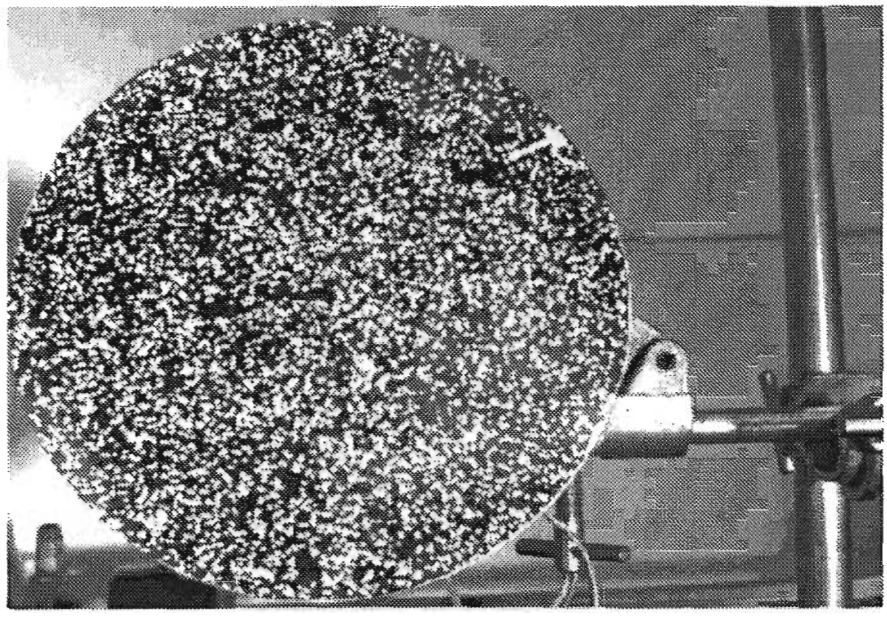

Figure 3.12: *A disc with random white dots on a black background.*

determined. A calibration card with a square grid pattern of 2 cm × 2 cm was pasted onto the disc and an image of it was taken. The image was then analysed using an image processing package IDL[2]. Since the measurements on the calibration card were known in centimeters, and the corresponding measurements could be read off the screen in pixels, it was possible to determine the calibration factors and these were found to be 42.27 pixels/cm in the x-direction and 41.86 pixels/cm in the y-direction.

After the two images of the rotating disc were analysed, a velocity vector field was plotted and this is shown in Figure 3.13. Using this velocity vector field, the speed of the disc was found to be 2.5 ms^{-1} at a radius of 5 cm,

[2]Interactive Data Language

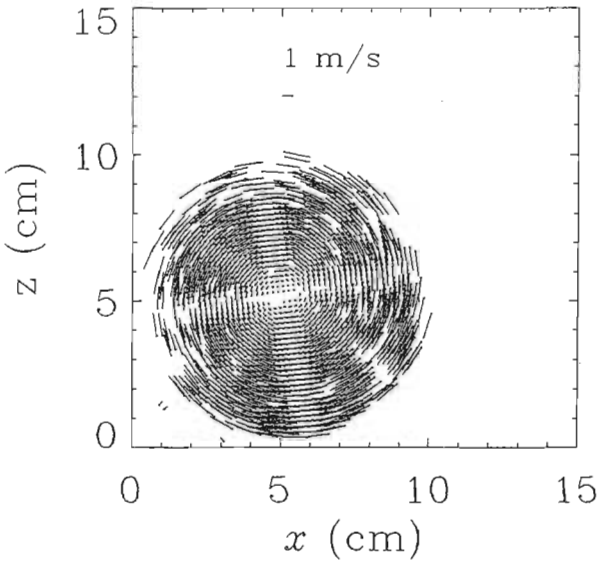

Figure 3.13: *Velocity vector field of rotating disc.*

corresponding to a frequency of 7.95 Hz.

As a result of the randomness in the position of the dots, there are areas where no dots appear. This lack of structure results in no velocity estimates at certain positions, as is visible from the vector plot. However, through a process of ensemble averaging the missing vectors can be filled in.

A second method was employed to determine the speed of the disc and this was accomplished by use of a free running stroboscope. In this method, an arrow was drawn onto the disc and the stroboscope was adjusted until the disc appeared to be stationary. The frequency of the disc was assumed to be the same as that of the stroboscope when this occurred. The strobe had

a frequency of 7.8 Hz when the arrow appeared to be stationary. The two measurements of angular frequency are in agreement, differing by 1.9%.

The radial dependency of the velocity as calculated by the two methods is illustrated in Figure 3.14. The plot shows that the measurements obtained from the DCIV method are in good agreement with the measurements obtained from the stroboscope. It is thus demonstrated that the DCIV technique is a reliable method.

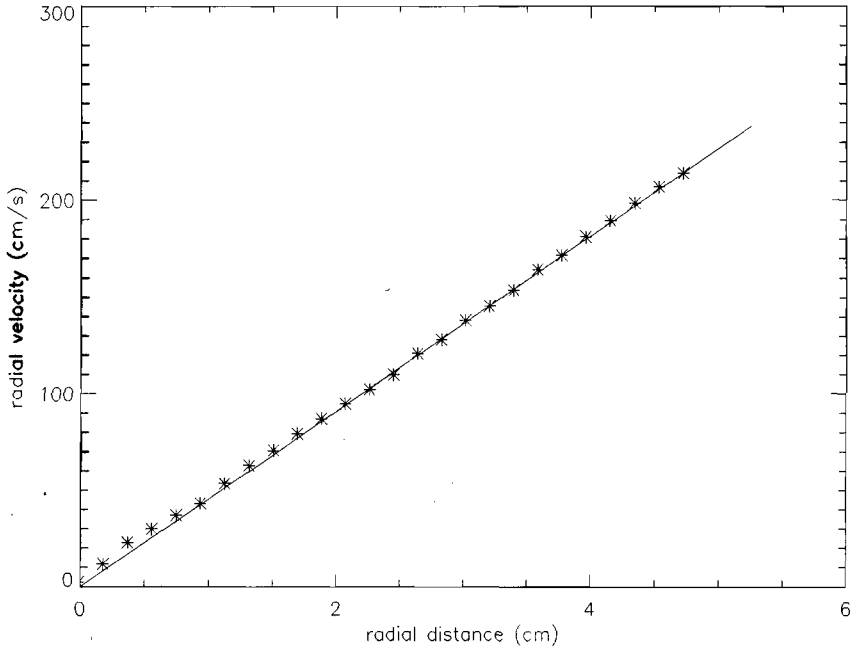

Figure 3.14: *Radial profile of velocity vectors as measured with the DCIV technique(*) and with a stroboscope (solid line).*

3.6 Summary

The experimental procedure was described as well as the flume dimensions and the measurement positions along the flume. The velocity measurement technique was discussed. The time series of the surface wave was obtained from the resistive wave gauge measurements. The velocity flow fields were measured by tracking the displacement of the seed particles and the aeration over a known time interval. The seed particles are polystyrene beads which are partially expanded (diameter of 1mm) to make them neutraly buoyant. There is however, a small difference between the seed velocities and the fluid velocities because the seeds are not perfectly neutrally buoyant. Experimental tests have shown that the error associated with this difference in velocities is much smaller than the error in velocity associated with the pixel resolution of the images. An experiment was conducted to demonstrate familiarity with the DCIV technique by measuring the velocity of points on a rotating disc. A second method was also employed to measure the velocity of the points on the rotating disc. DCIV was shown to be a reliable technique.

Chapter 4

Surface Elevation Measurements

4.1 Introduction

In this chapter the characteristics of waves approaching and breaking over an artificial sand bar, as inferred from the measurement of the surface displacement, are described. Measurements of the time series of the waves is presented for positions before and after breaking. Fourier Analysis of the time series then resulted in the spectral evolution of the wave as it approaches breaking and beyond.

Also available from the time series measurements of the surface profile are the overall wavelength and the amplitude of each spectral component. These are used to examine the growth of energy in each spectral component and also the decay of energy after breaking. Comparisons of the energy decay

measurement with those predicted by the bore approximation of wave after breaking is also presented. Potential energy estimates show a gradual decrease in energy in the fundamental component and a steady increase in energy in the first and second harmonics, for waves prior to breaking. After breaking, the potential energy continues to decrease, reaching a minimum and then increasing to a steady value thereafter.

Examination of the wave profile shows a gradual change from being sinusoidal in deep water to becoming non-linear as it approaches shallow water. The crests become peaked and the troughs are drawn out. Beyond the break point the wave has a saw-tooth profile. Beyond the break point, in the flat section of the bed, the wave profile is still non-linear due to the harmonics which are still present in the wave.

The experimental procedure and calibration are described in section 4.2 followed by the spectral analysis in section 4.3. The energy analysis is described in section 4.4 and the comparison of wave profiles with theory is discussed in section 4.5.

4.2 Experimental Procedure

The description of the flume and experimental conditions have been given in the previous chapter, however, some of it is repeated here for completeness. Figure 4.1 shows a schematic of the wave flume which is identical to that used by *Mory [1994]*. A piston type wave maker produces regular sinusoidal

waves of period $T = 1.5\,\mathrm{s}$ and having a wave height of 7.4 cm in the deep water section of the flume. The bottom topography, which is of bar type, is placed 8.2 m from the wave maker. The bar has an upslope (1 : 20), a 10 cm horizontal crest, a 70 cm downslope (1 : 10) and a 2 m horizontal section. The still water depth in the section in front of the bar is 40 cm, at the crest of the bar it is 10 cm and in the horizontal section beyond the bar it is 17 cm. At the end of the bar is an absorbing beach. A magnified schematic showing the measurement positions and bar profile, more clearly, is given in Figure 4.2.

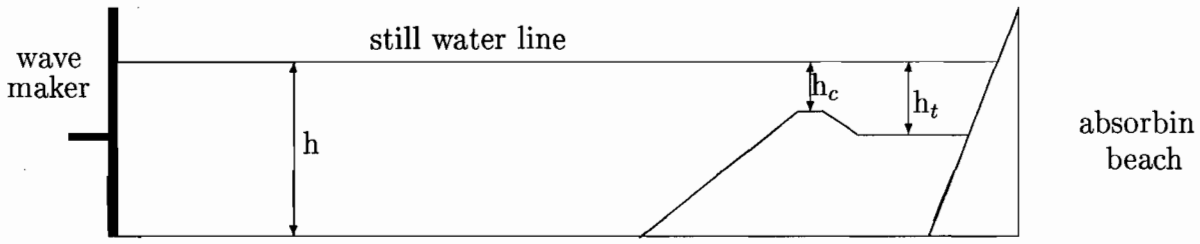

Figure 4.1: *Schematic of the wave flume.*

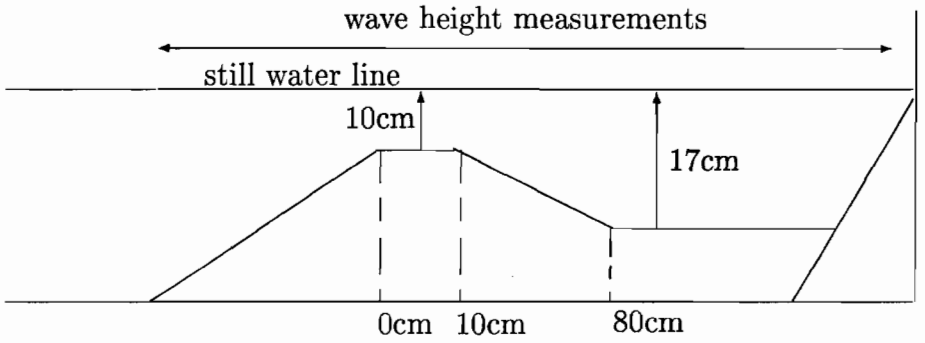

Figure 4.2: *Magnified schematic showing measurement positions and bar profile.*

The free surface displacements of waves propagating along the flume were measured using resistive gauges and were recorded onto the audio channel of a video cassette recorder (VCR). The measured signal was modulated on a 600 Hz carrier wave before being recorded onto the audio channel of the VCR. An available frequency demodulating circuit was used to demodulate the measurement signal from the carrier wave. A digital storage oscilloscope (DSO) was used to observe and store the signal. Commercially available software, Wavestar, was used to acquire the signal from the DSO and to generate a text file containing the time and output voltage of the signal. These text files were used for further processing. A block diagram illustrating the above procedure is given in Figure 4.3.

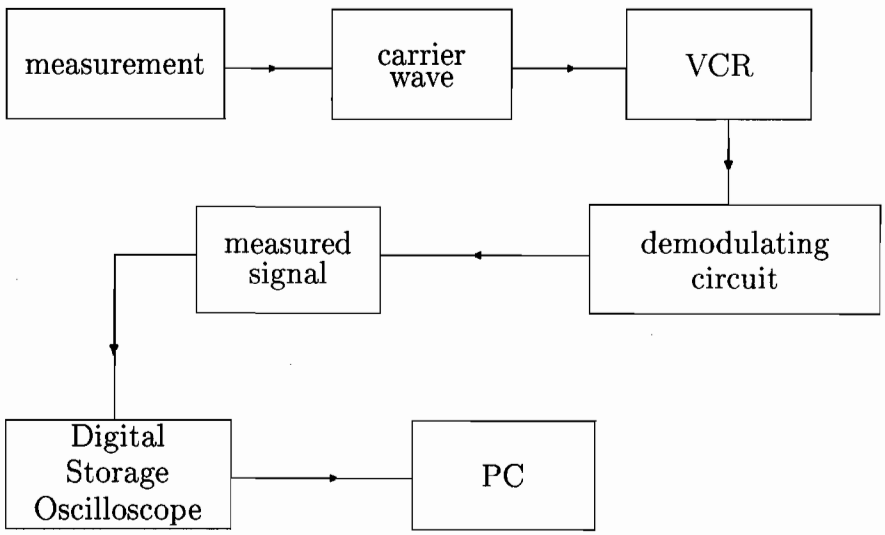

Figure 4.3: *Block diagram showing the path of the signal from the moment of capture to being input to a PC.*

4.2.1 Gauge Calibration

The output of the audio channel of the VCR gives the time series of the water level as a voltage. It is essential to convert the output voltages to centimeters in order to investigate the physical sensibility of our results. To this effect a gauge calibration was performed. At 1 cm intervals from 25 cm to 35 cm, the resistive gauge displacement was recorded. At each of these positions, the corresponding output voltage was recorded. The graph of voltage versus gauge displacement that was obtained is shown in Figure 4.4.

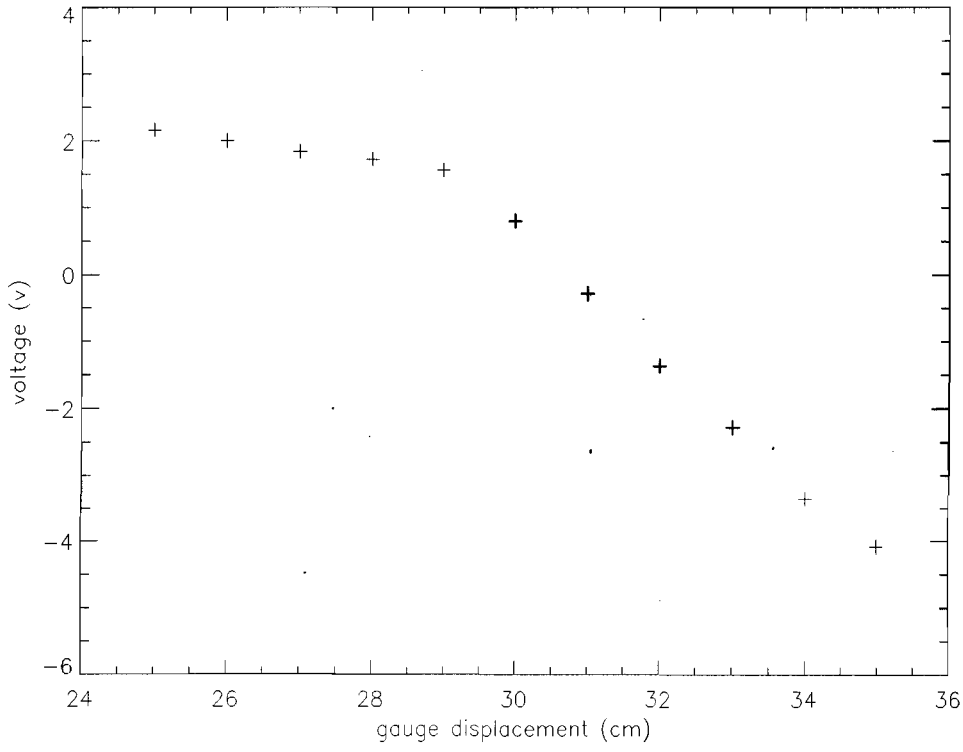

Figure 4.4: *Calibration curve showing the output voltage and the corresponding gauge displacement.*

It is evident from Figure 4.4 that the calibration curve is not linear. This non-linearity is actually a measurement oversight resulting from saturation of the wave gauge amplifier. We overcome this measurement oversight by fitting two straight lines to our measurements, one for displacements less than 29 cm and another for displacements greater than or equal to 29 cm. The 'best fit' linear curves were obtained using the data analysis program Microcal Origin. The equations of the best fit curves were used to convert the temporal water level measurements from volts to centimeters.

Further, a gauge displacement of 30 cm corresponds to the position of the still water line (swl). Table 3.1 tabulates the relationship between gauge displacement and position from the swl. The positive signs indicate positions above the swl, while the negative signs indicate positions below the swl.

Gauge displacement(cm)	25	26	27	28	29	30	31	32	33	34	
Position from still water line(cm)	+5	+4	+3	+2	+1	0	-1	-2	-3	-4	

Table 3.1. Gauge displacement versus position from still water line.

4.3 Frequency Spectra across the Flume

The frequency spectra were obtained by computing the Fast Fourier Transforms (FFT) of the free surface displacements. The FFT were computed from a set of 2000 points. Figures 4.5 and 4.6 show the time variation of the free surface displacements in the first column and the corresponding frequency spectra in the second column. The frequencies observed are f = 0.67, 1.33,

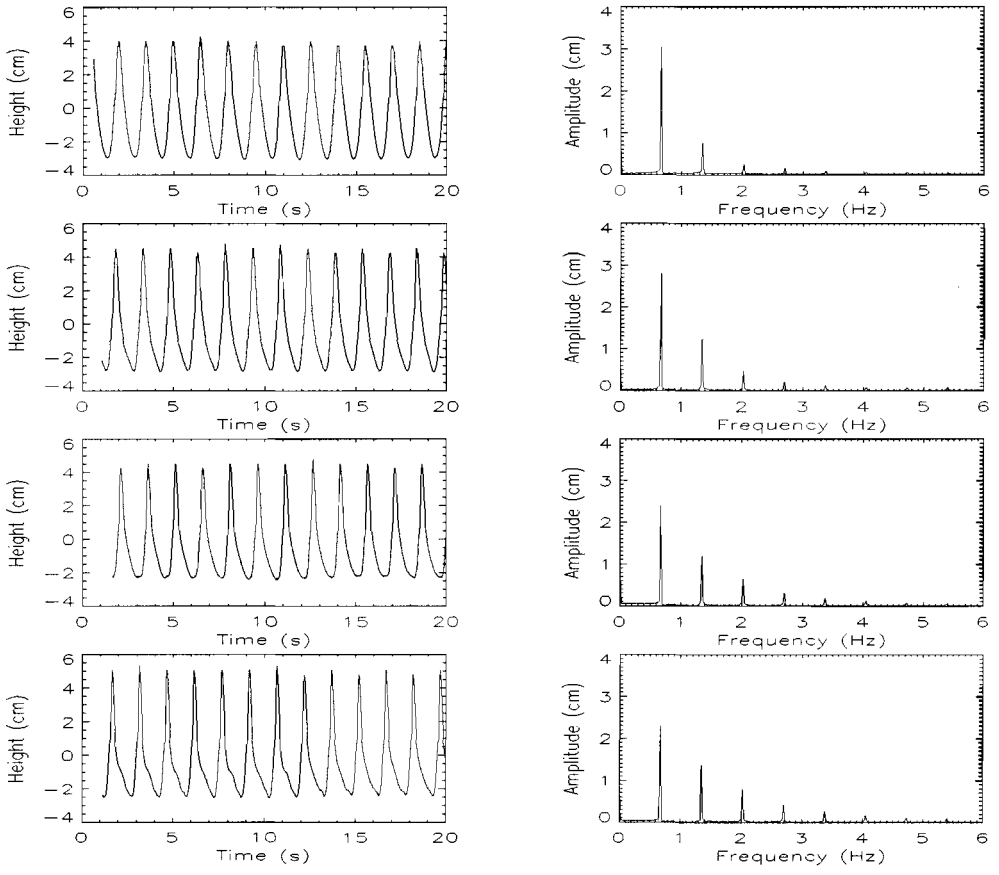

Figure 4.5: *Free surface displacements and corresponding frequency spectra prior to breaking at positions (from top to bottom)* $x - x_b = -200, -140, -80$ *and* -40 *cm.*

2.00, 2.67 and 3.33 Hz. Harmonics are generated by the interaction of the wave with the bottom boundary surface. The amplitude of the harmonics increases as the bottom slope increases. A decrease in the primary mode is accompanied by an increase in the amplitudes of the higher frequencies. Also, note that even after breaking, the harmonics are still present in the flat section of the bed beyond the break point.

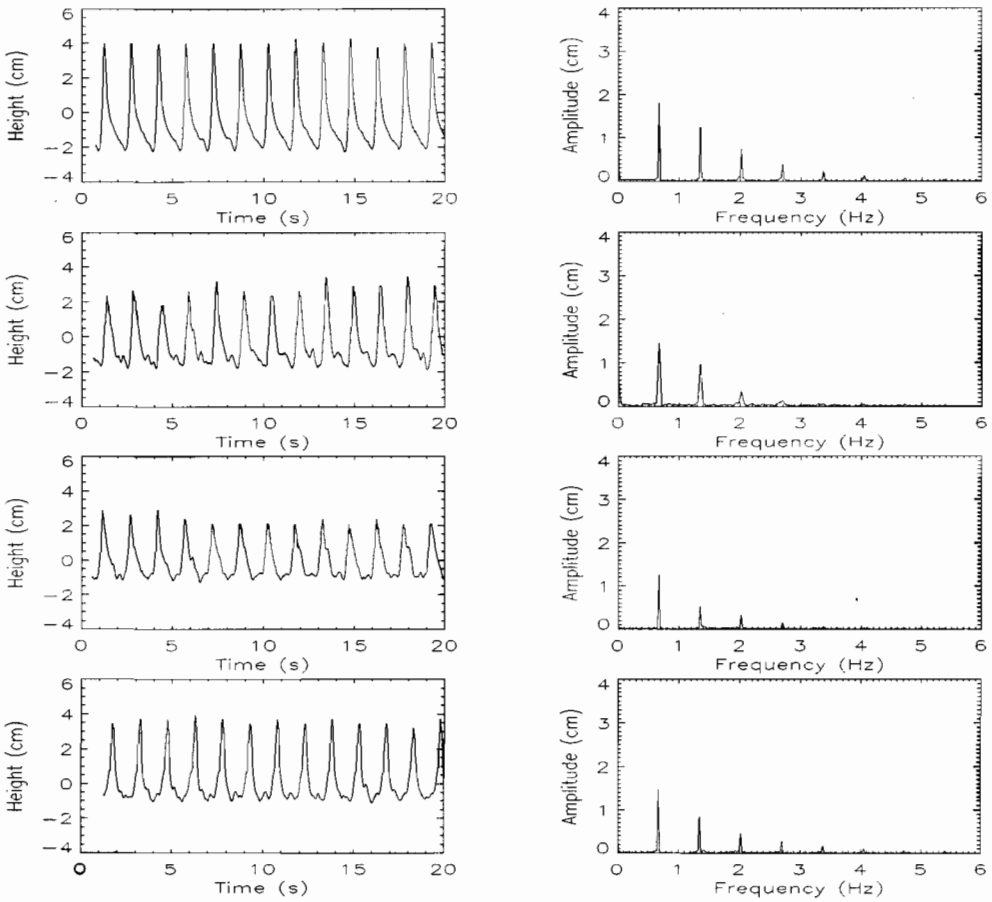

Figure 4.6: *Free surface displacements and corresponding frequency spectra at the break point and beyond at positions (from top to bottom)* $x - x_b = 0, 40, 100$ *and* 160 *cm.*

The time variation of the free surface displacements clearly shows the changes in the symmetry of the wave as it reaches the horizontal bar, breaks and is reconstructed. Initially the form of the free surface displacements is sinusoidal. As the waves migrate towards the horizontal bar, their crests become peaky and the troughs lose their symmetry. Figure 4.7 depicts the free surface displacements at various positions along the flume, corresponding to different stages of the wave evolution over the bar. Only one wave cycle is plotted to show the details more clearly.

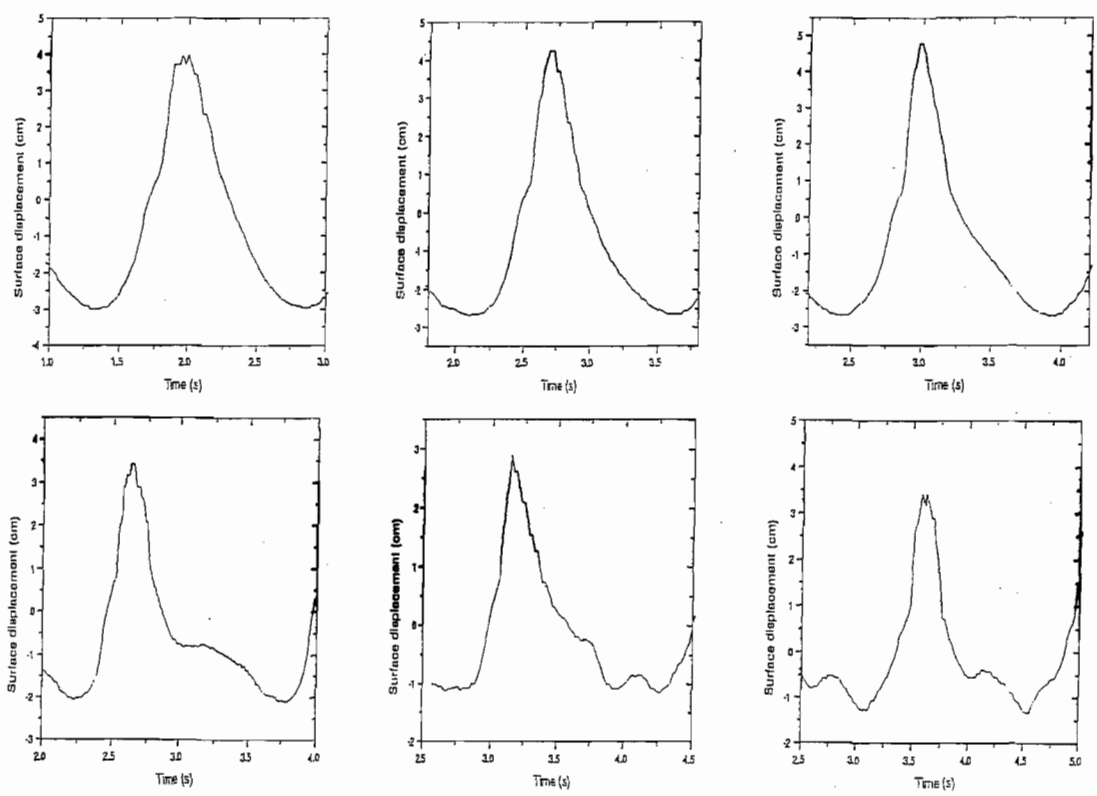

Figure 4.7: *Single wave cycles of the free surface displacements at positions(from left to right), top row,* $x - x_b = -200$, *-160 and* $-100\,cm$, *and bottom row,* $x - x_b = 20$, *100 and* $140\,cm$.

4.4 Wave Height Distribution and Energy Analysis

At various positions along the flume approximately 30 cycles of the surface elevations were captured. The wave height of each cycle was determined and the average was computed. Figure 4.8 below shows the variation in wave height as the wave shoals, in the breaking region and past breaking. In Figure 4.8, there is a slight increase in wave height until the maximum is reached just prior to breaking. This is followed by a sharp decrease in wave height in the breaking region until a minimum height of 3.5 cm is reached at $x - x_b = 100\,\text{cm}$. Beyond $x - x_b = 100\,\text{cm}$, the wave height increases again.

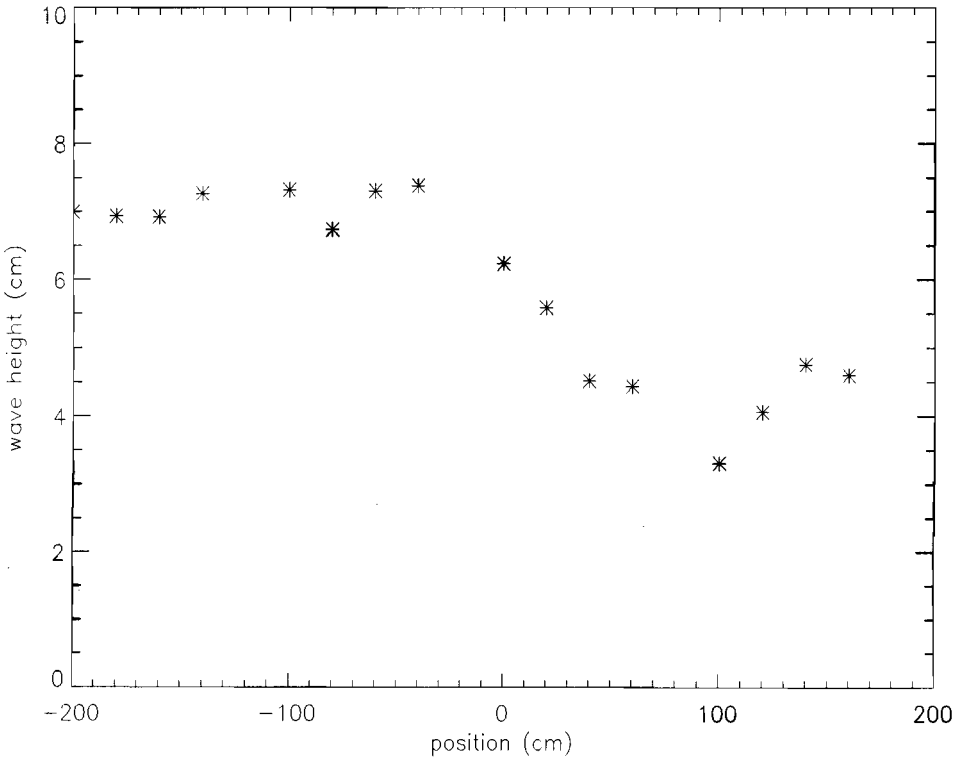

Figure 4.8: *Measured wave height distribution across the flume.*

The variation in wave height is a combination of three effects, the change in water depth, the dissipation of energy and the change in the shape of the wave *[Svendsen, 1984]*. The observed trend in the wave height measurements may be explained as follows. As the waves approach the breakpoint, they begin to slow down, due to the reduced water depth. This reduction in speed is accompanied by an increase in wave height in order to maintain a constant energy flux, thus the gradual increase in wave height up to the break point. The wave period remains unchanged but the wavelength is shortened. and wave crests become more peaked. The wave steepness (H/L) increases until it reaches a critical value. At this point, the wave crest peaks sharply, becomes unstable and breaks. Beyond the break point, there is a reduction in wave height due to breaking.

As shown in the next chapter, the decrease in wave height is accompanied by an increase in the currents generated as a result of breaking. Some of the energy in the current is transferred back to the wave resulting in an increase in wave height further along the flume at $x - x_b \approx 140\,\text{cm}$.

4.4.1 Potential Energy

The potential energy corresponding to each harmonic is computed using $E = \frac{1}{16}\rho g H^2$ where H is twice the amplitude of each spectral component. Figure 4.9 shows the spatial variation of the potential energy density. The asterisks denote the total potential energy, the crosses denote the potential energy of the primary mode, the dots and the plus signs denote the potential energy associated with the first and second modes respectively.

Prior to breaking, there is an increase in the potential energy associated with the first and second modes. In the breaking zone there is a very rapid decrease in the potential energy with all modes experiencing a minimum at position 100 cm. As shown in the next chapter, the decrease in potential energy in the region $0 - 100$ cm beyond the break point is associated with an increase in the kinetic energy of the mean currents generated as a result of breaking.

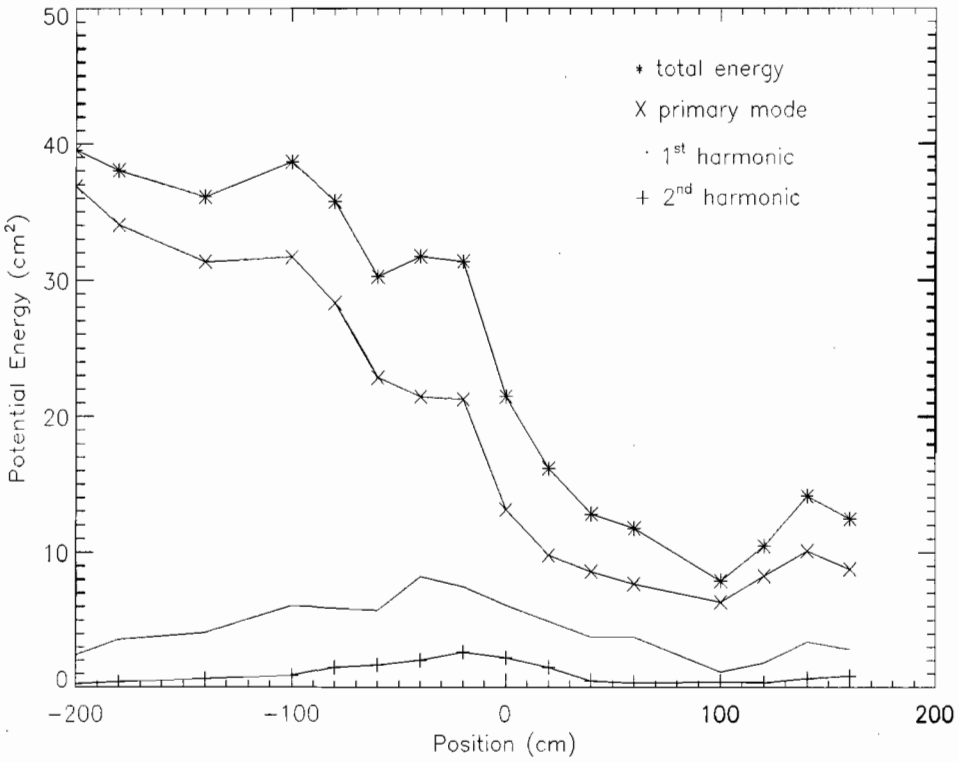

Figure 4.9: *Variation of the potential energy density (normalised with respect to $\frac{\rho g}{16}$) of the primary mode (X) and the first (solid line) and second (+) harmonics.*

4.4.2 Energy Dissipation

The energy dissipation rate has been estimated from the gradient in the energy flux ($c\,E$), as follows

$$D = -\frac{d}{dx}(cE) \tag{4.1}$$

where $c = \sqrt{gd}$ is the shallow water wave speed and $\mathrm{E} = \frac{1}{8}\,\rho\,\mathrm{g}\,\mathrm{H}^2$. Figure 4.10 shows the energy dissipation as a function of position. The asterisks denote

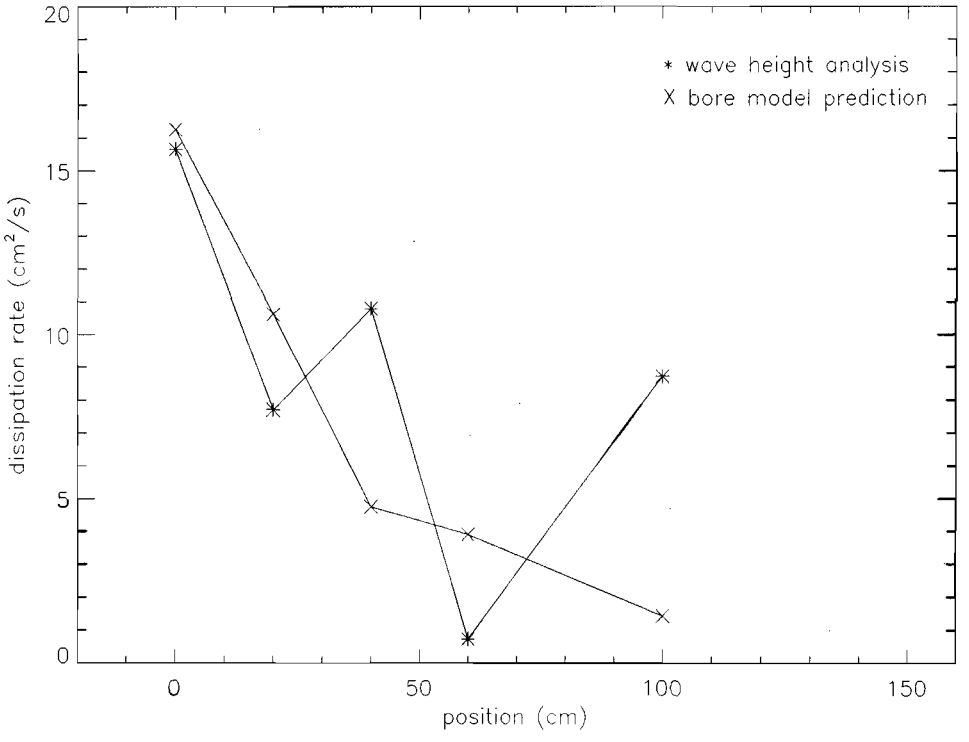

Figure 4.10: *Energy Dissipation as calculated from wave height analysis (*) and the bore prediction (X). Note that the dissipation rate is normalised with respect to* $\frac{\rho g}{8}$.

the energy dissipation calculated using equation 4.1 and the crosses denote

the dissipation rate as given by the bore approximation, which is discussed below.

Battjes and Janssen [1978], developed a model for predicting the dissipation of energy in random waves breaking on a beach. In their model the dissipation rate per breaking wave is estimated from that in a bore of corresponding height. The equation for the bore model of energy dissipation is

$$D = \frac{1}{4} f \rho g \frac{H^3}{h} \tag{4.2}$$

where f is the frequency.

The general trend of the energy dissipation measurements as given by the bore approximation is a decrease with position. At $x - x_b = 0$ and $x - x_b = 20$ the dissipation in a surf zone wave is larger than that predicted by the bore approximation. There is some agreement between the measured dissipation and that predicted by the bore analogy. The scatter in the measured dissipation is associated with approximating the derivative in equation 4.1 with finite differences.

4.5 Comparison of Experimental Surface Profiles with Theory

Although surface waves are inherently non-linear, it is assumed that the amplitude of the waves on the water surface is infinitely small. This approximation leads to the equations of motion which are a part of linear wave theory. If it is assumed that the amplitudes are small but not infinitely so, wave properties that can be written as a power series of kH are obtained. This finite-amplitude theory is known as Stokes theory. In this section our experimental results are compared with both linear theory and Stokes theory.

Single wave cycles of the experimental data at positions $x-x_b = -200, -100, 0,$ 40 and 140 cm have been plotted. Each cycle is compared with Stokes theory and linear theory. The expression for Stokes second order solution, as given in *Fredsoe and Deigaard [1992]*, is

$$\eta = \frac{H}{2}\cos(\omega t - kx) + \frac{1}{16}kH^2\big(3\coth^3(kD) - \coth(kD)\big)\cos\big(2(\omega t - kx)\big). \tag{4.3}$$

where all symbols have their usual meaning.

In deep water, at $x - x_b = -200$ cm, linear theory resembles the form of the experimental data points. Stokes theory also predicts the experimental curve well. The peak of the experimental data points is smaller than that predicted by Stokes theory. At $x-x_b = -100$ cm Stokes theory deviates from the experimental data points. Here, the linear curve gives better agreement with the experimental data points than Stokes theory.

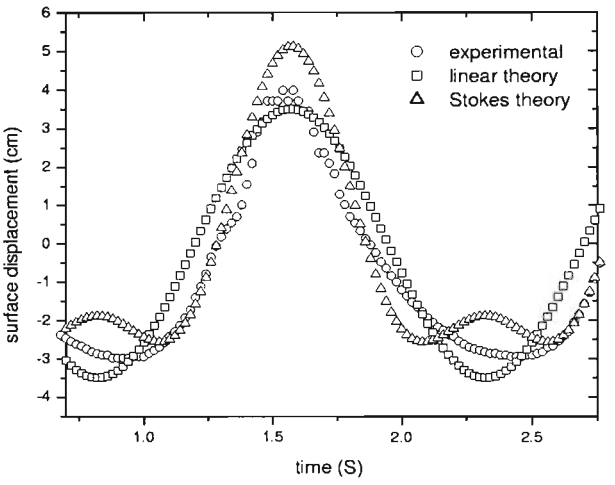

Figure 4.11: *Comparison of experimental data(∘) with linear theory (□) and Stokes theory(△) at* $x - x_b = -200\ cm.$

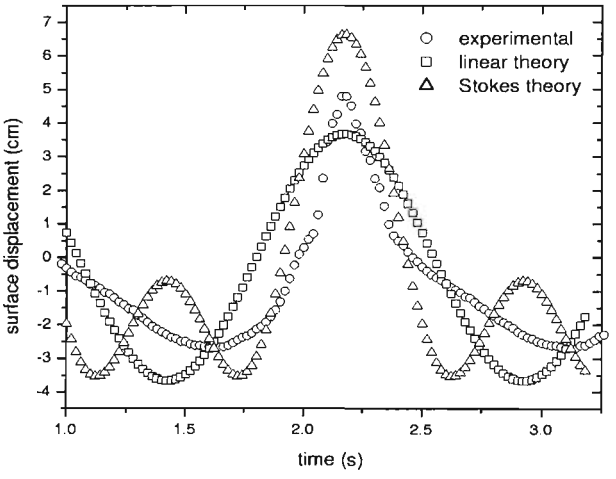

Figure 4.12: *Comparison of experimental data(∘) with linear theory (□) and Stokes theory(△) at* $x - x_b = -100\ cm.$

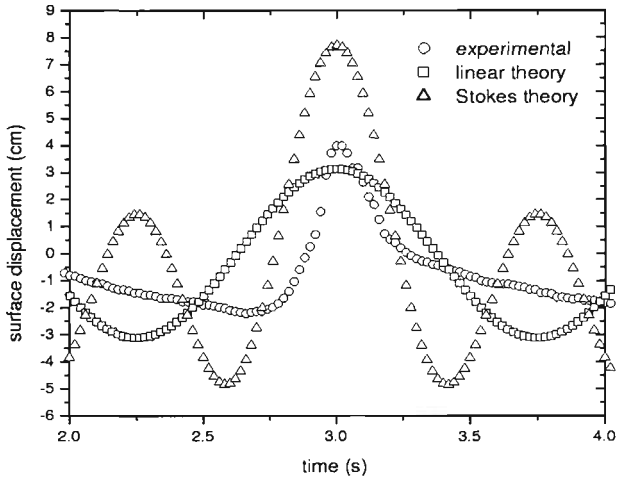

Figure 4.13: *Comparison of experimental data(∘) with linear theory (□) and Stokes theory(△) at* $x - x_b = 0\ cm$.

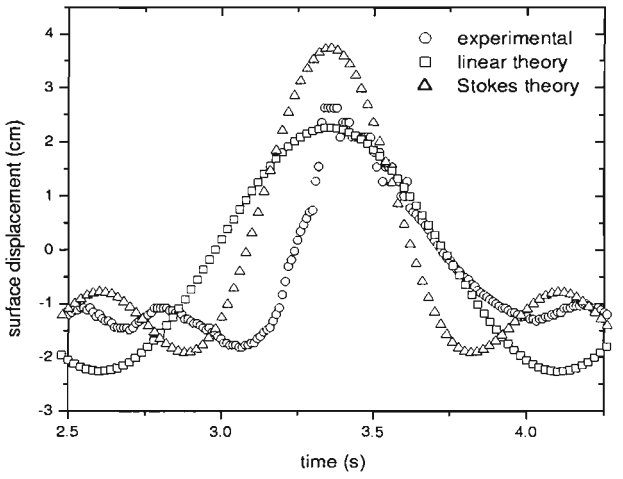

Figure 4.14: *Comparison of experimental data(∘) with linear theory (□) and Stokes theory(△) at* $x - x_b = 40\ cm$.

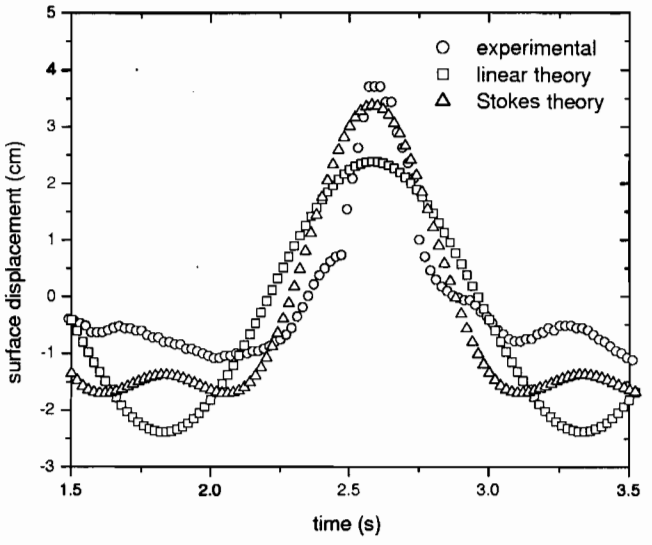

Figure 4.15: *Comparison of experimental data(∘) with linear theory (□) and Stokes theory(△) at* $x - x_b = 140\ cm$.

At $x - x_b = 0\,\text{cm}$, neither linear theory nor Stokes theory is able to describe the experimental data points. The peak of the Stokes curve is much larger than that of the experimental data. The linear curve gives a better prediction of the peak in the experimental data. At $x - x_b = 40\,\text{cm}$ the results are similar to those at the break point. Even here, both theories fail to be representative of the experimental data. The linear curve co-incides with the experimental curve between times 3.38 and 3.82 s. The Stokes curve appears to have nothing in common with the experimental curve. The above two positions are in close proximity to the break point and this explains the poor fit. At these positions the processes are highly non-linear.

Further on, at $x - x_b = 140\,\text{cm}$, linear theory fails to predict the experimental data points. Stokes theory is a reasonable approximation of the experimental data. Although the Stokes curve does not co-incide with the experimental curve, it is able to predict the shape of the experimental data points well. The peak of the crest of the experimental data is only slightly larger than that predicted by Stokes theory. At this position, there is no breaking and therefore the fit is good.

It is clear from the above figures that under weakly non-linear situations the second order Stokes theory is well suited to describing the surface profile. For a more accurate representation of the wave surface, higher order Stokes formulae would be necessary. Alternatively, advanced theory such as stream function theory or cnoidal wave theory may be used.

4.6 Summary

Measurements were made of the free surface displacements of waves breaking over a bar in a laboratory flume. The variation in wave height across the flume was plotted. It was found that the wave height increases to reach a maximum value just before breaking. After breaking there is a sharp decrease in wave height until a minimum is reached $x - x_b = 100cm$. Thereafter, the wave height increases again.

The time series of the surface elevations were plotted along with the corresponding frequency spectra. It was found that the wave becomes asymmetrical as it approaches the break point. Also, there is more than one frequency component present. Only frequencies that are simple harmonics of the frequency of the wave maker are observed. The amplitude of the primary frequency decreases as the wave shoals while the amplitudes of the higher frequencies increase. The potential energies of the primary mode as well as that of the higher harmonics were calculated.

The rate of energy dissipation as calculated by two different methods, the bore prediction and wave height analysis, were compared. The bore prediction shows a decrease in energy dissipation as the distance from the break point increases. Wave height analysis shows a similar pattern initially.

A comparison of experimental data with linear theory and Stokes theory was conducted. Five positions were chosen, two prior to breaking, the break point and two after breaking, to investigate the relationship between experiment

and theory. Single wave cycles of experimental data, linear theory and Stokes theory were plotted on the same set of axes. Stokes theory is found to be a close approximation to the experimental data in shallow water. In deep water, linear theory predicts the experimental curves well. In the vicinity of the break point, neither theory is able to predict the experimental curves well.

Chapter 5

Mass, Momentum and Energy Flux Measurements

5.1 Introduction

In this chapter the video measurements of the velocity flow fields in laboratory waves breaking over a bar are presented. Details of the wave flume, bottom profile and wave conditions were described in chapter 3. However, certain relevant details will be repeated here in section 5.2.

The instantaneous velocity fields were obtained using the technique of digital correlation image velocimetry (DCIV). This method involves tracking the positions of particles and aeration structures over a specific time interval. Two consecutive images were obtained a few milliseconds apart, the second image being a shifted version of the first. This gives the displacements of the particles as well as the time interval, and so the particle velocities may

be computed. The measurement of the phase-ensemble-averaged and time-averaged velocity fields are presented in section 5.3.

The mass, momentum and energy flux were obtained by depth integrating the time-averaged velocity flow fields. The relative density of the fluid in the crests of the waves was obtained by taking the ratio of the reverse and forward velocity fluxes, and it was used to correct the momentum and energy calculations in the regions above the wave crests. Plots of mass, momentum and energy as functions of position from the bar are given. Changes in both momentum and energy have been detected. These and other observations are discussed.

The results are compared to those obtained with a different technique, namely, Laser Doppler Anemometry *[Mory, 1994]*. Laser Doppler Anemometry is sensitive to the presence of air bubbles, and therefore LDA measurements are available mostly for positions below the trough level. Thus using the video technique, results are presented that are not available elsewhere.

5.2 Experimental Conditions and Procedures

A magnified view of the bar profile is shown in Figure 5.1. Velocity flow fields were measured on the downslope section of the bar and on the horizontal section following the bar. The wave conditions were as stated in previous chapters, that is, the wave period, $T = 1.5\,\mathrm{s}$ and the deep water wave height

is 7.4 cm.

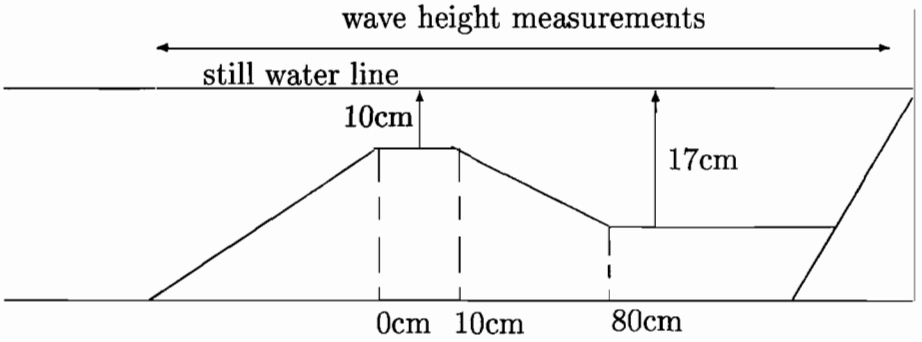

Figure 5.1: *Magnified schematic showing the bottom profile.*

The velocity vector field of the wave was measured using Digital Correlation Image Velocimetry (DCIV). The computational details of this technique can be found elsewhere in this thesis. This technique enables measurements in highly aerated regions of the wave. Three sampling times(time interval between image pair), 1, 5 and 10 ms, were used to measure each instantaneous flow field. In some parts of the wave the particle velocities are very large and therefore shorter sampling times were used. In regions where the particle velocities are smaller, longer sampling times were necessary.

Figure 5.2 illustrates the method used to determine the velocity field of the wave. The wave was imaged at four sections along the flume, namely, 10 - 40 cm, 40 - 80 cm, 80 - 100 cm and 100 - 130 cm beyond the break point. At each section a pair of images, separated by a few milliseconds, of the wave was captured at a particular wave phase by means of a trigger signal from the wave generator. This was repeated for the next 50 wave cycles.

The above procedure was performed for the three sampling times of 1, 5 and 10 ms, resulting in 150 image pairs. The trigger delay from the generator was then adjusted to capture images at a different wave phase but at the same section along the flume. In this way the wave was imaged at 12 equally spaced phases. This procedure was then repeated for other positions along the flume.

Each image pair was analysed using the DCIV technique and each pair resulted in a single instantaneous flow field. Thus, at each measurement section, there were 150 instantaneous flow fields at each wave phase. These 150 images were then processed to give the phase ensemble-averaged horizontal and vertical velocities, (u, w), together with u^2, w^2, u', w', u'^2, and w'^2, where u' and w' are the fluctuating parts of the horizontal and vertical velocities, respectively. The characteristics of the fluctuating parts of the velocities will not be discussed in this thesis.

The ensemble-averaged flow fields of each of the twelve sections were averaged to give the time-averaged flow field over the entire wave. It is from these time-averaged flow fields that the measurements of the mass, momentum and energy are computed.

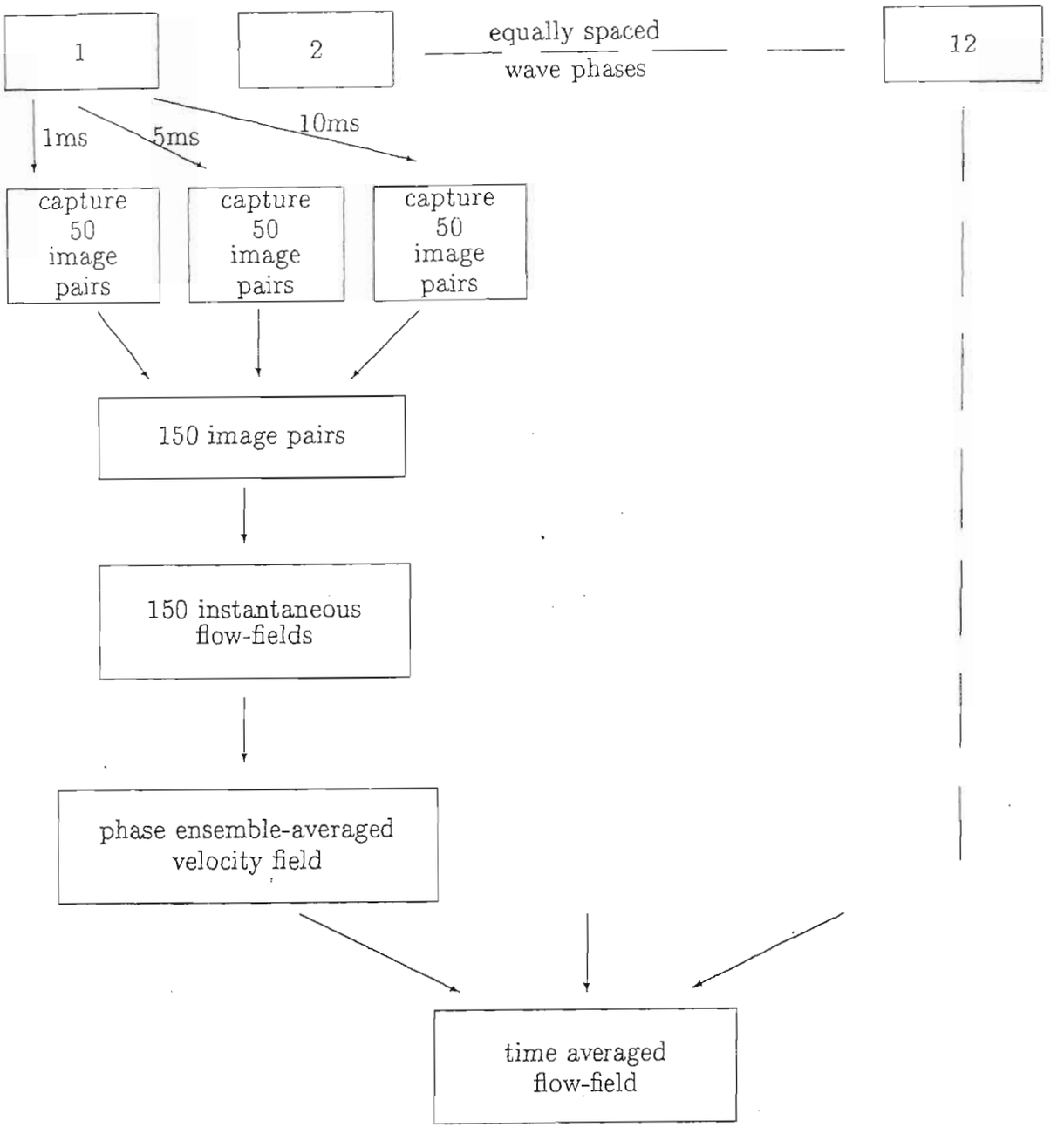

Figure 5.2: *Procedure involved in processing the instantaneous velocity field. The blocks numbered* 1 *to* 12 *represent approximately a* 30 *cm section of the wave at a particular phase, at a given position along the flume.*

5.3 Results

5.3.1 Phase-Ensemble-Averaged Flow Fields

Figure 5.3 shows the phase-ensemble-averaged flow field at one particular phase at the first measurement position, that is at $10 - 40\,\text{cm}$ beyond the break point. Samples of the phase-ensemble-averaged flow field at other phases at the same position are shown in Figure 5.4.

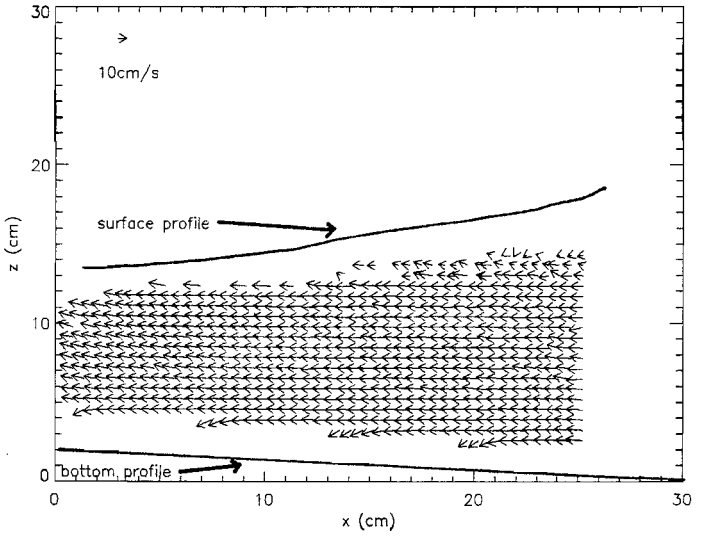

Figure 5.3: *Phase-ensemble-averaged flow field, at position* $10-40$ *cm beyond the break point, for a particular wave phase. Also shown in the figure are the wave surface and bed profile.*

The velocities in the crests are approximately $20\,\text{cms}^{-1}$ while in the trough region they are $10\,\text{cms}^{-1}$. It is clearly visible that measurements are available for positions high up in the crest area. Velocity measurements are restricted

to positions 2 cm above the bottom boundary.

Vectors are plotted on a uniform grid having a horizontal and a vertical spatial resolution of 0.6 cm and 0.57 cm respectively. The velocity flow fields for the other positions are similar in character to that shown in Figure 5.4. Prior to time-averaging, the phase-ensemble-averaged flow fields are interpolated using a 2-D (TRIGRID / INTERPOL) algorithm available in IDL to fill in areas with missing vectors.

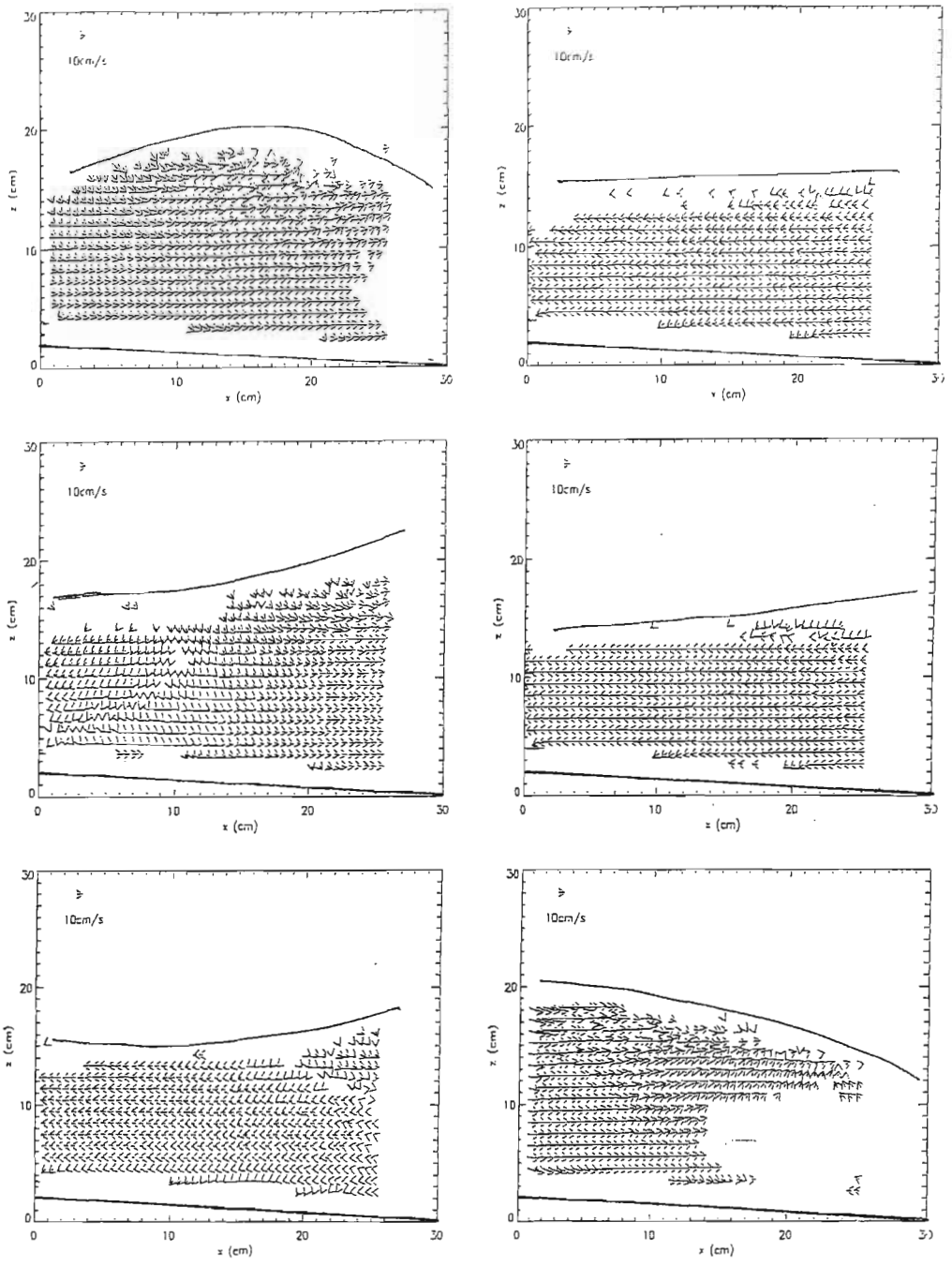

Figure 5.4: *Samples of the phase-ensemble-averaged flow fields at position* $10 - 40\,cm$ *beyond the break point, from top to bottom, spanning the entire wave.*

5.3.2 Time-Averaged Velocity Measurements

Figure 5.5 illustrates the time-averaged velocity vectors, together with the bottom profile. The x-axis shows the horizontal position from the bar. The z-axis represents the vertical postions relative to the still water line (swl). Note that the horizontal spatial resolution of the vector field shown in Figure 5.5 has been reduced to show the vectors more clearly.

Careful examination of Figure 5.5 indicates a circulation or an eddy formation as a result of the wave breaking over the bar. In the region $-3 \leq z \leq 3\,\text{cm}$ and $40 \leq x - x_b \leq 150\,\text{cm}$, the flow above the swl is towards the shore. In the same region, the flow below the swl is towards the sea. At $x - x_b = 40\,\text{cm}$ and $x - x_b = 150\,\text{cm}$ the flow is approximately vertically up and vertically down respectively. Thus one may draw in an elongated ellipse showing the circulation/eddy. Above the approximate trough level there is a net flow in the forward direction and a net reverse flow (undertow) below. It is evident from the plot that in the region $10 \leq x - x_b \leq 70\,\text{cm}$ the velocities in the crest regions are much larger than those in the lower part of the wave. The maximum velocity in the forward direction is $26\,\text{cm}\,\text{s}^{-1}$, while the maximum velocity in the return flow is $11\,\text{cm}\,\text{s}^{-1}$. Beyond $x - x_b \approx 80\,\text{cm}$, the velocities in both directions are much smaller than the velocities in the regions nearer to the bar, and the magnitude of the velocity in the forward direction equals the magnitude of the velocity in the reverse direction.

In order to show more detail the time-averaged vectors at a few selected positions are plotted on separate graphs. These are shown in Figure 5.6.

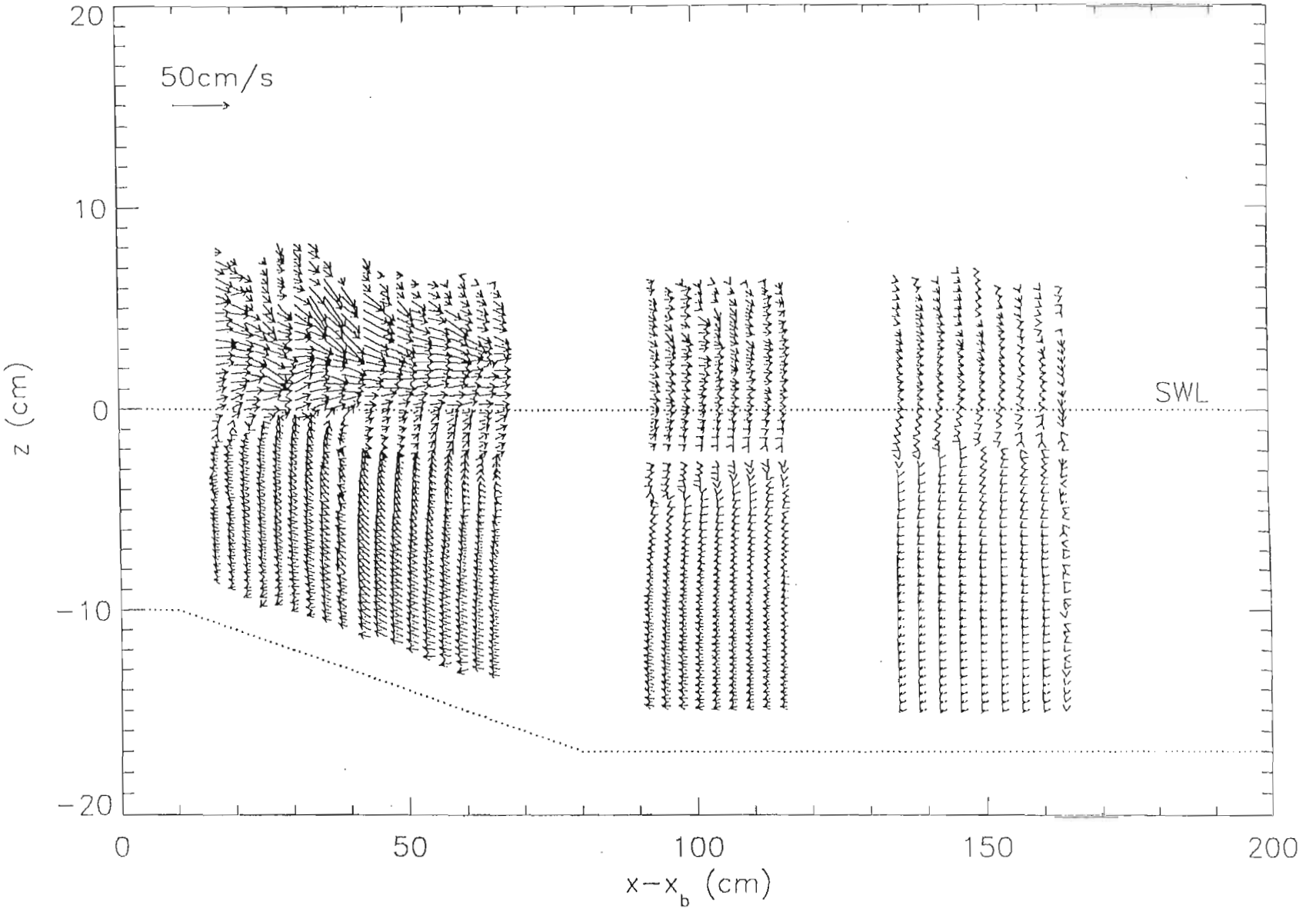

Figure 5.5: *Vertical profiles of the time-averaged velocity vectors for positions beyond the bar.*

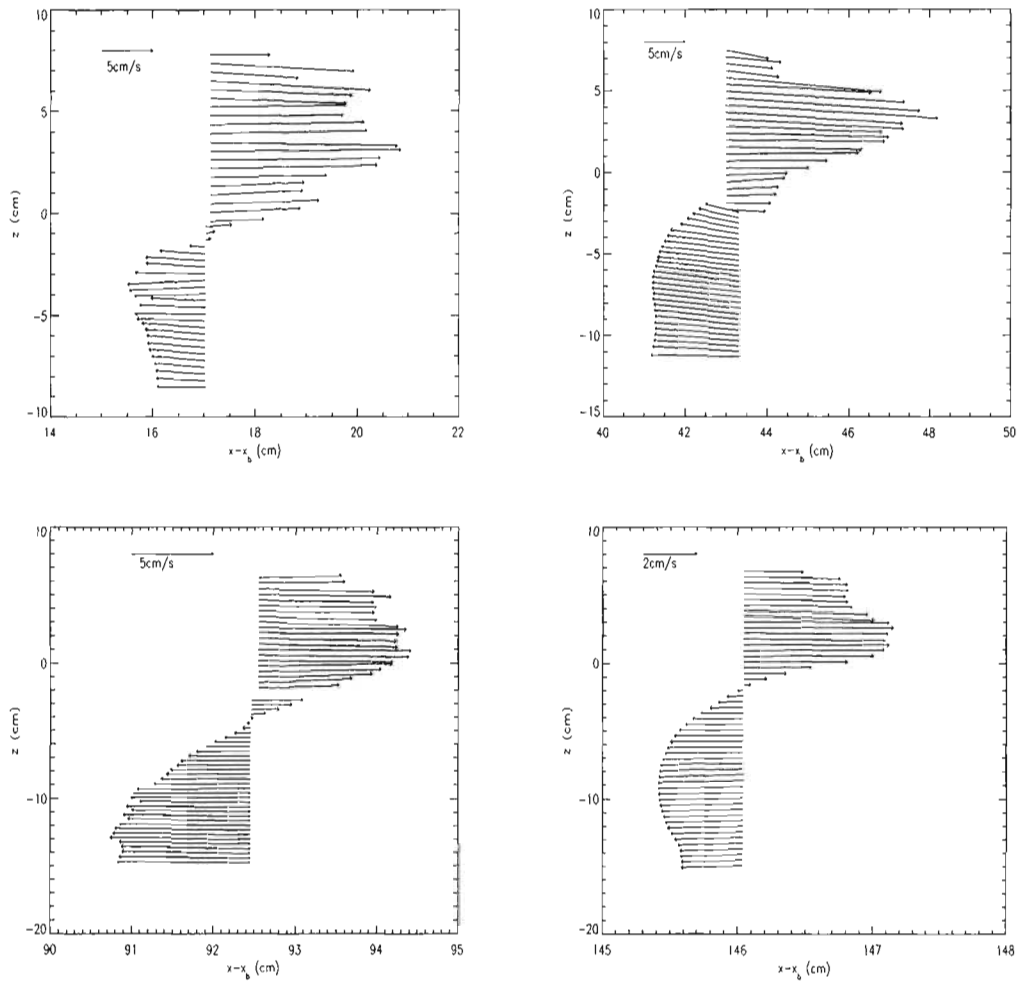

Figure 5.6: *Magnified profiles of the time-averaged velocity vector as a function of depth at (clockwise starting from top left)* $x - x_b \approx 17, 43, 146$ *and* 92 *cm beyond the break point.*

In the first graph (top left) of Figure 5.6 the profile of the undertow is almost linear with the velocity increasing from the bottom up. This is typical of pre-breaking waves. Although this is the region just after breaking, the effects due to breaking are yet to reach the undertow at this position. Further along the flume, in the top right of Figure 5.6, we observe a change in the profile of the undertow. The velocity no longer increases upwards but rather seems to be almost constant. Further still, in the bottom left of Figure 5.6, the profile of the undertow decreases from the bottom upwards. In the last graph of Figure 5.6 the profile of the undertow is a smooth curve with the maximum velocity at the center of the profile.

Using the time-averaged values $\overline{u}, \overline{w}, \overline{u^2}$, and $\overline{w^2}$, at each of the vertical and horizontal positions where vectors are drawn in Figure 5.5, the mass flux due to the mean current, the momentum flux of the mean current and the energy are calculated by numerical evaluation of the following integrals

$$\begin{aligned} mass\,/\,velocity flux &= \int \overline{u}\, dz \\ momentum flux &= \int \rho_r \overline{u}^2\, dz \\ energy &= \frac{1}{2}\int \rho_r(\overline{u^2} + \overline{w^2})\, dz \end{aligned}$$

that is,

$$\begin{aligned} mass flux &= \sum u_j\, \delta z \\ momentum flux &= \sum \rho_r \overline{u}_j{}^2\, \delta z \\ energy &= \frac{1}{2}\sum \rho_r(\overline{u_j^2} + \overline{w_j^2})\, \delta z \end{aligned}$$

where j refers to the vertical grid positions in Figure 5.5 and δz is the spac-

ing between grid positions. (Note that the above formulae are normalised with respect to the density of water.) In most cases, the summation in the previous formulae are divided for positions below the approximate trough level and for positions above the approximate trough level.

The mass (velocity) flux calculation is used to determine the relative density of fluid above the trough level and the relative density is used in further calculations involving the momentum flux and the energy for positions above the approximate trough level. For positions below the approximate trough level, $\rho_r = 1$.

5.3.3 Mass Flux

Figure 5.7 shows the plot of the forward and reverse mass flux, $\int \overline{u}\, dz$ (normalised with respect to the density of water), as a function of distance from the bar. The plus signs indicate the flux in the crest regions and the asterisks denote the mass flux in the return flow (undertow). In the region $0 \leq x - x_b \leq 70\,\text{cm}$ the profiles of the flux in the forward and reverse directions are very similar. In both cases, there is a maximum is reached at $x - x_b \approx 40\,\text{cm}$. After reaching the maximum value there is a steady decrease in mass flux. Beyond $x - x_b = 90\,\text{cm}$, the flux in the forward direction is equal to the flux in the reverse direction. In the region $130 \leq x - x_b \leq 160\,\text{cm}$, the mass flux is well described by a constant $30\,\text{cm}^2\text{s}^{-1}$.

The characteristic features of Figure 5.7 may be explained using the following argument. When some critical wave height is reached, breaking occurs.

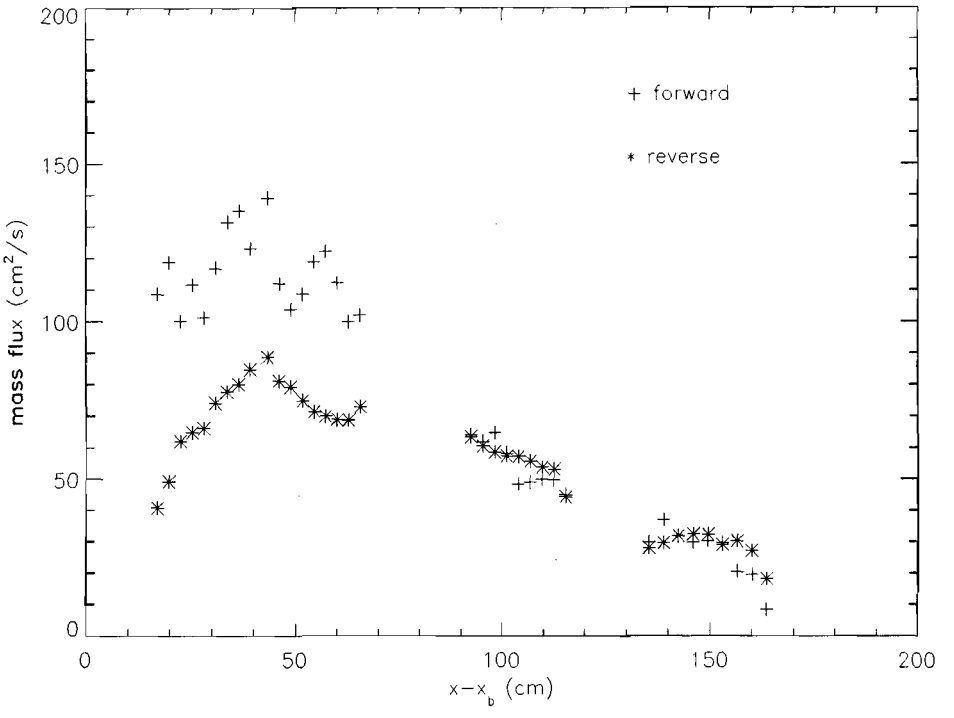

Figure 5.7: *Forward horizontal mass flux above the approximate trough level (+) and reverse horizontal mass flux below approximate trough level (*) for positions beyond the break point.*

This results in the formation of a roller which rides on the front surface of the wave. In the region $0 \leq x - x_b \leq 40\,\text{cm}$ the roller size increases and this results in the increase in forward mass flux. Beyond $x - x_b = 40\,\text{cm}$, wave breaking ceases accompanied by a decrease in roller size and thus there is a corresponding decrease in forward mass flux. Similarly, for the undertow, all the fluid that reaches the non-absorbing beach must return 'seawards', where it originated. This is evident in the pattern of the undertow current which mimics the form of the flux in the forward direction.

Since the water in the flume forms a closed system, at each vertical section there should be conservation of mass, that is, the mass flowing above the trough level must equal the mass flowing below the trough level. In Figure 5.7 there is a discrepancy between the forward and reverse flux in the region $10 \leq x - x_b \leq 70$ cm. This discrepancy is due to the water in the crest regions being highly aerated and hence its density is not the same as the density of water in the trough regions. Thus the ratio reverse flux/forward flux gives the relative density, ρ_r, of the water in the upper parts of the wave.

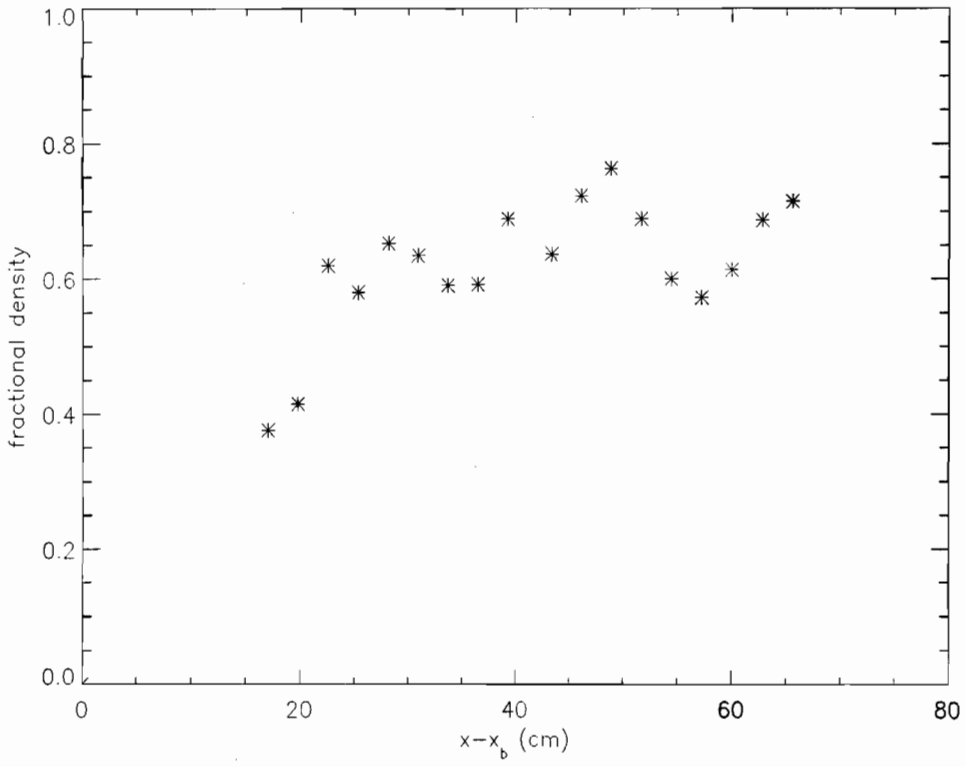

Figure 5.8: *Fractional density* $\frac{\rho_{crest}}{\rho_{water}}$ *of the fluid in the crest for horizontal positions beyond the break point.*

Figure 5.8 illustrates the relative density as a function of position from the bar. The relative density was only calculated for the region just after breaking. The reason for this is, further away from the break point the mass flux in the forward direction is equal to the flux in the return flow. This is to be expected since there is not much aeration in the crest area further away from the break point. The average relative density is approximately 0.7. This means that the density of the water in the highly aerated crest regions is $\approx$ $700\,\mathrm{kgm}^{-3}$. The estimated relative density is used in all further calculations involving the waves crests. In the range $10 \leq x - x_b \leq 70\,\mathrm{cm}$, ρ_r has values as given in Figure 5.8 for all vertical positions above the approximate trough level. For all other positions ρ_r is taken to be unity.

5.3.4 Momentum Flux

The horizontal momentum flux, $\int \rho_r \overline{u}^2\, dz$, of the mean forward and reverse currents as a function of position from the bar is depicted in Figure 5.9. The plus signs denote the momentum flux in the forward direction whilst the asterisks denote the momentum flux in the reverse flow.

It is observed that the momentum in the crest area is very much larger than that in the trough region. In the return flow there is an increase in momentum until a maximum is reached at $x - x_b = 40\,\mathrm{cm}$. A similar pattern is seen in the momentum flux of the crest regions. The maximum momentum flux in the crest region is ≈ 1.7 times the maximum flux in the return flow. In the region $80 \leq x - x_b \leq 120\,\mathrm{cm}$, there is a steady decrease in momentum and the flux in both directions is approximately equal. Beyond $x - x_b = 130\,\mathrm{cm}$,

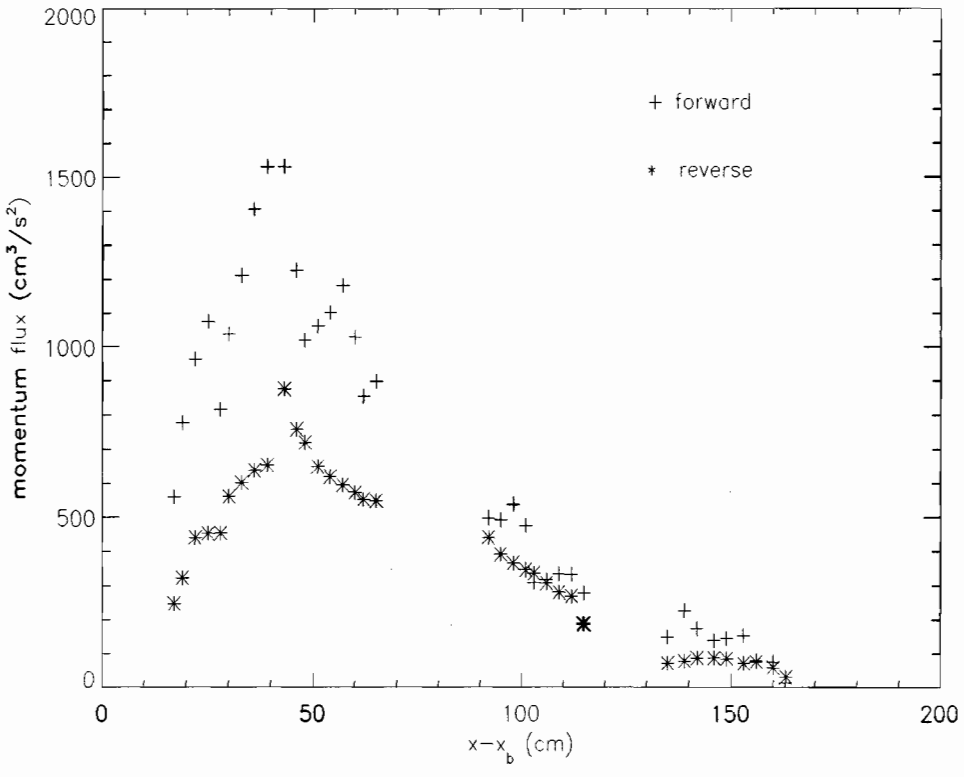

Figure 5.9: *Forward horizontal momentum flux above the approximate trough level(+) and reverse horizontal momentum flux below approximate trough level(*) of the mean current for positions beyond the break point.*

the flux in each direction may be approximated by a constant value. The momentum flux in the crest being approximately 150 $\mathrm{cm^3 s^{-2}}$ and the flux in the return flow slightly lower at $90\,\mathrm{cm^3 s^{-2}}$.

A plot of the total horizontal momentum, $\int \rho_r \overline{u^2}\, dz$, versus position from the bar is given in Figure 5.10. From linear theory, $S = 0.5\,E$ in deep water, where S is the momentum flux of the wave and E is the wave energy. This yields an initial momentum flux of $3354\,\mathrm{cm^3\,s^{-2}}$ in terms of ρ. From the plot,

the maximum momentum flux is $9000\,\mathrm{cm^3\,s^{-2}}$ in terms of ρ. This maximum momentum flux occurs at approximately the same position from the bar as the maximum mass flux. This increase in momentum flux is due to the additional mass being transported in the roller. Hence, the large increase in mass flux due to the presence of a roller results in an increase in momentum flux.

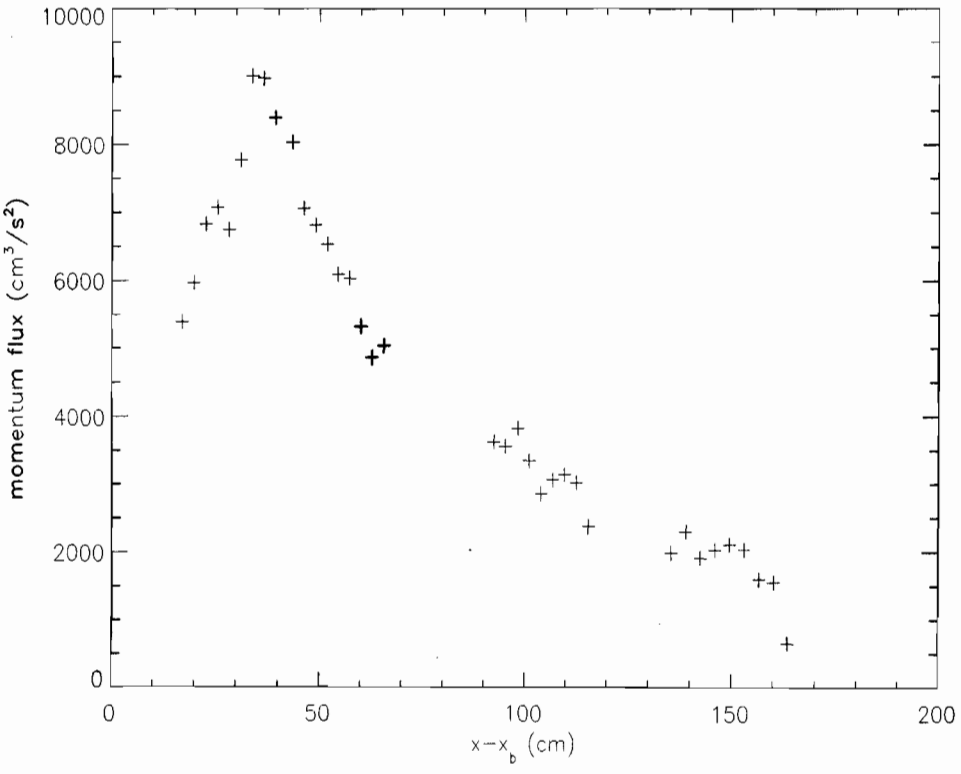

Figure 5.10: *Total momentum flux of wave plus current for positions beyond the break point, (normalised with respect to ρ_{water}).*

N.B. The momentum flux is the same as the depth integrated value of the kinetic energy density or more specifically, the kinetic energy of the horizontal

motion. Thus, an increase in momentum flux implies an increase in energy density. This increase in kinetic energy density is due to the conversion of wave potential energy into kinetic energy.

5.3.5 Energy Flux

Figure 5.11 illustrates the energy of the mean current ($\frac{1}{2}\int \rho_r \, (\overline{u^2} + \overline{w^2}) \, dz$) as a function of position from the bar. The asterisks denote the energy of the reverse current and the plus signs denote the energy of the forward current. The energy of the reverse current has a very distinct pattern.

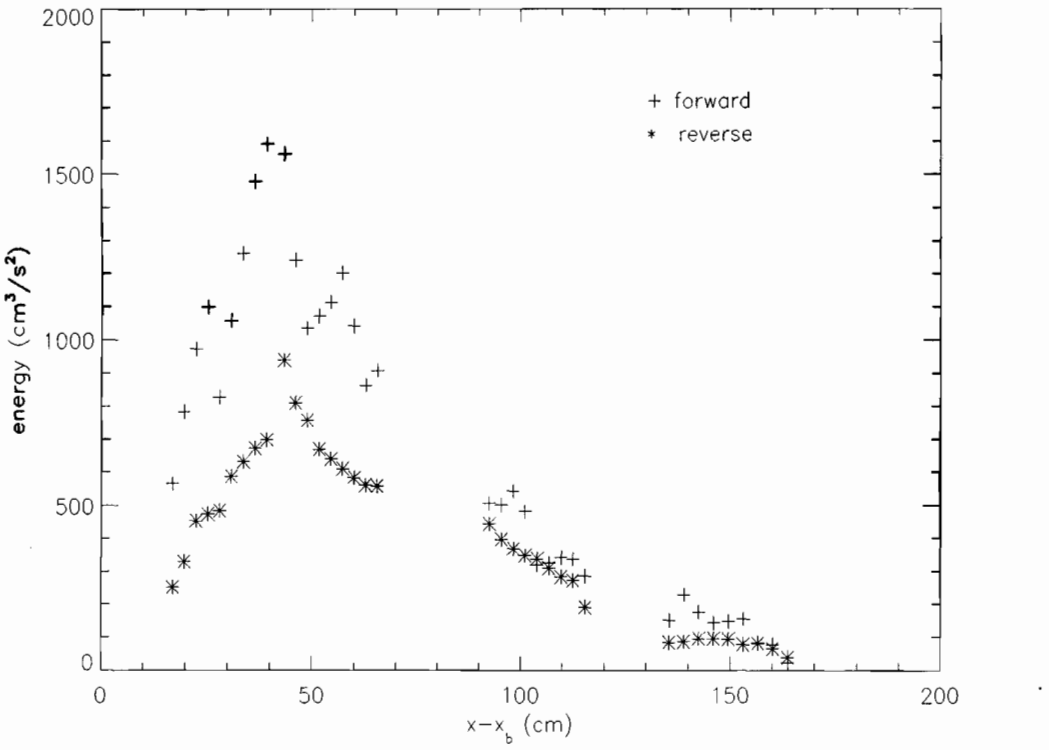

Figure 5.11: *Energy of mean forward current above the approximate trough level(+) and mean current below(*), (normalised with respect to ρ_{water}).*

There is a steady increase in energy until a maximum of 900 $cm^3\,s^{-2}$ is reached at $x - x_b = 40\,cm$. Thereafter, the energy decreases steadily. Beyond, $x - x_b = 130\,cm$ the energy of the reverse current is a constant $100\,cm^3\,s^{-2}$. The maximum energy of the forward current, $1600\,cm^3\,s^{-2}$, is reached at $x - x_b = 40\,cm$. Beyond $x - x_b = 60\,cm$, the energy decreases until it 'levels-off' to $150\,cm^3\,s^{-2}$ at $x - x_b = 140\,cm$.

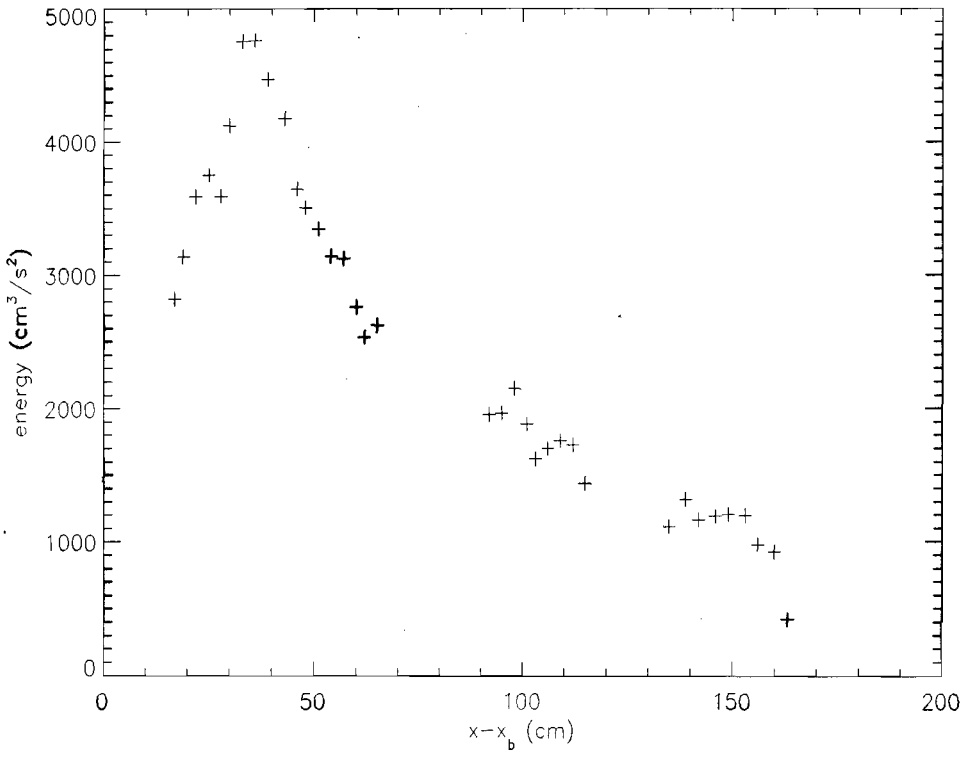

Figure 5.12: *Total kinetic energy of wave and current normalised with respect to* ρ_{water}.

Similarly to the momentum flux,the energy flux of the crest regions has been multiplied by the relative density. Figure 5.12 illustrates the total kinetic energy of the wave plus current, $\frac{1}{2}\int \rho_r(u^2 + w^2)\,dz$ as a function of posi-

tion from the bar. The total energy increases rapidly from $2800\,\mathrm{cm^3\,s^{-2}}$ at $x - x_b = 20\,\mathrm{cm}$ to $4750\,\mathrm{cm^3\,s^{-2}}$ at $x - x_b = 35\,\mathrm{cm}$. Thereafter there is a decrease in energy. In the region $120 \leq x - x_b \leq 150\,\mathrm{cm}$ the energy flux is constant at $\approx 1150\,\mathrm{cm^3\,s^{-2}}$.

From linear theory, the initial energy of the wave is given by $\frac{1}{8}\rho g H^2$, where H is the wave height. This translates to $E = 6708\,\mathrm{cm^3\,s^{-2}}$ in terms of ρ. This initial energy is shared equally between kinetic energy and potential energy, that is, $3354\,\mathrm{cm^3\,s^{-2}}$ each. Thus, there is an increase in kinetic energy from $3354\,\mathrm{cm^3\,s^{-2}}$ to $4750\,\mathrm{cm^3\,s^{-2}}$. This increase in kinetic energy is due to the initial potential energy of the wave being converted to kinetic energy in the breaking process.

5.4 Comparison with LDA Measurements

Figure 5.13 depicts the profiles of the velocity flow field resulting from two different methods. The asterisks denote the horizontal velocity obtained using Laser Doppler Anemometry (LDA) *[Mory, 1994]*. The plus signs denote the horizontal velocity obtained using the video technique.

The profiles of both measurements are approximately the same. In the region $-10 \leq z \leq -5\,\mathrm{cm}$ the profiles are in good agreement with each other. There is however some deviation from the LDA measurements closer to the bed. It is evident that many more measurements are possible with the video technique, especially in the aerated crest regions where LDA cannot provide

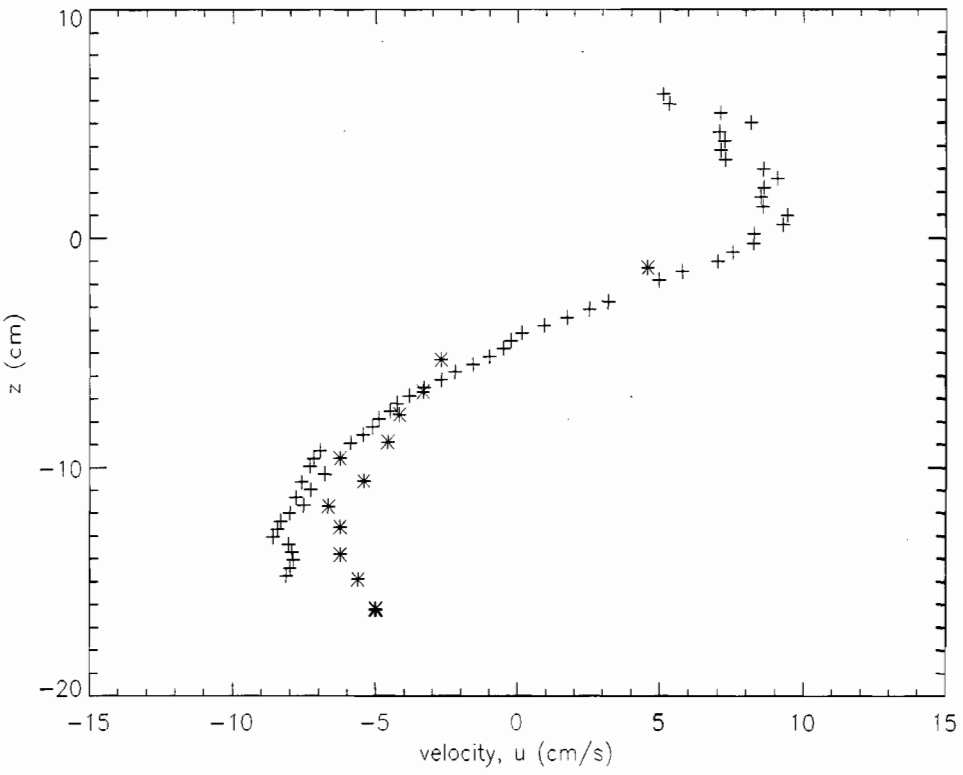

Figure 5.13: *Time-averaged horizontal velocity at* $x - x_b \approx 95\,cm$ *as measured by LDA [Mory, 1994] (*) and DCIV (+).*

sufficient measurements. The maximum velocity from the LDA measurements is $-7\,\mathrm{cms}^{-1}$ and from the video measurements it is $-9\,\mathrm{cms}^{-1}$.

5.5 Summary

Measurements were made of various internal parameters of waves breaking over a bar in a laboratory flume. The time-averaged velocity flow fields were presented. From the plots we deduce that in the region soon after breaking, the velocities in the crests of the waves are larger compared to the velocities

in the troughs of the waves. The maximum velocity in the crest was found to be 26 cms^{-1}, and in the troughs it was -11 cms^{-1}. It is also evident that the profile of the undertow changes from having a maximum at the top to having its maximum velocity at the center of the profile.

The forward mass flux in the crests of the waves was found to be larger than the reverse mass flux below the trough level. This was due to a difference in the fluid densities in these regions. The fractional density of the fluid in the crests was calculated to be in the range 600 $kg\,m^{-3}$ - 800 $kg\,m^{-3}$.

The initial momentum flux of the wave was calulated as 3354 $cm^3\,s^{-2}$ in terms of ρ. From the plot of momentum versus position from the bar the maximum momentum was 9500 $cm^3\,s^{-2}$. This increase in momentum flux may be attributed to the large increase in mass flux in the wave roller.

The initial energy (per unit area) of the wave was 6708 $cm^3\,s^{-2}$ in terms of ρ. From the plot of kinetic energy versus position from the bar, the maximum energy was 4750 $cm^3\,s^{-2}$ in terms of ρ. Thus, there is an increase in kinetic energy in the region soon after breaking. The increase in kinetic energy is due to the initial potential energy of the wave being converted to kinetic energy during wave breaking.

Our video measurements show good agreement with measurements obtained from Laser Doppler Anemometry (LDA). One advantage video techniques have over LDA is that while LDA is sensitive to the presence of air bubbles,

video techniques are not. For this reason video measurements are available well into the aerated crest regions. Also, the video technique is non-intrusive and is less labour intensive.

Chapter 6

Wave Roller and Aeration

6.1 Introduction

When water waves break, the overturning of the wave crest results in the formation of a surface roller. The roller is a body of aerated fluid that rides on the front face of the wave and is transported shorewards. As a result of the aeration, the density of the fluid in the roller is lower than that in the rest of the wave. A detailed knowledge of the dynamics and physical characteristics of the roller is essential for the analysis of turbulence generation and mass, momentum and energy transport in the crest of the waves.

The investigation and analysis of surface rollers and their characteristics is not a simple task. Hence we proceed cautiously with a qualitative approach to the formation and propagation of surface rollers as well as the distribution of aeration. In particular we investigate the roller area and aeration.

Two methods of estimating the roller area are explored here. The first method utilises the wave gauge measurements of the surface elevation whilst the second uses video images. The wave gauge measurements of the surface elevation for several wave cycles at each position were plotted and analysed. The portion of the wave cycle that is considered to constitute the roller was determined. The area of the surface roller was calculated for each of the wave cycles and an average was computed. This procedure was repeated for other positions beyond the break point.

The estimate of the roller area from video images was restricted to one position. Using the cursor we outlined the overall surface profile, the approximate lower aeration boundary and an estimate of the wave profile in the absence of a roller. The roller area and the aeration area were estimated from these profiles. The video images were analysed with IDL[1], an image processing program.

Before elaborating on the wave gauge measurements and the video measurements, we first discuss some theory and revise previous results. Some concepts have already been introduced in Chapter 2 but are included here for completeness and ease of reading.

[1]Interactive Data Language

6.2 Theory and Previous Measurements

The schematic shown in Figure 6.1 illustrates the concept of a roller riding on the front face of a wave. The important geometrical characteristics are the cross-sectional area of the roller and the slope of the roller.

It is assumed that the roller is that part of the wave lying above an imaginary line joining the foot of the wave front and the peak of the crest. Also, the slope of this line is considered to be the roller slope *[Schaffer et al., 1992; Engelund, 1981].*

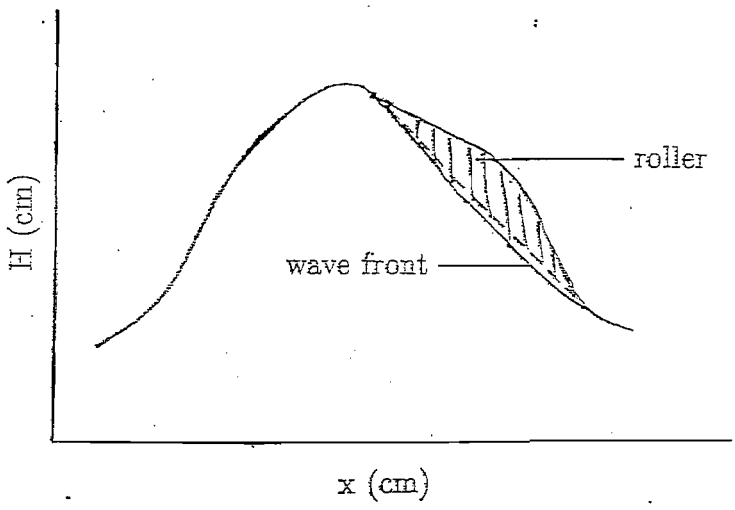

Figure 6.1: *Schematic of a roller on the front face of a wave.*

A theoretical estimate of the roller area can be made by comparing the broken wave with an hydraulic jump. *Engelund [1981]* devised a model of the hydraulic jump in which the roller is stationary and is regarded as a layer of "dead" water. Using this model, the cross-sectional area of the surface roller

is given by

$$A = \frac{H^3}{4D\alpha_0} \tag{6.1}$$

where α_0 is the slope of the straight line boundary between the roller and the water below, H is the wave height and D is the mean water depth.

The energy flux E_r of the roller is given by *[Svendsen, 1984]*

$$E_r = \frac{A}{2\lambda}\rho c^3 \tag{6.2}$$

where ρ is the fluid density, c is the wave propagation speed, A is the area of the roller, λ is the wavelength.

The momentum flux F_r due to the roller is

$$F_r = \rho c \frac{A}{T} \tag{6.3}$$

where T is the wave period.

There have been a limited number of measurements of wave roller area reported in the literature. We mention only a few here. One of the earliest mesaurements is by *Duncan [1981]*. He conducted an experiment that generated breaking waves when a hydrofoil was towed through water. *Svendsen [1984]*, using the data from *Duncan [1981]*, derived an empircal formula for the roller area as

$$A \approx 0.9H^2. \tag{6.4}$$

Govender [1999] investigated the minimum and maximum aeration areas in the surf zone for both spilling and plunging waves. He found that the normalised area for spilling waves spans a range of 0.5 to 1.5 and is almost evenly distributed about the $\frac{A_r}{H^2} = 0.9$ line as shown in Figure 6.2. The normalised area for plunging waves shows an increasing trend and is greater than 0.9 for the major part of the surf zone as shown in Figure 6.3.

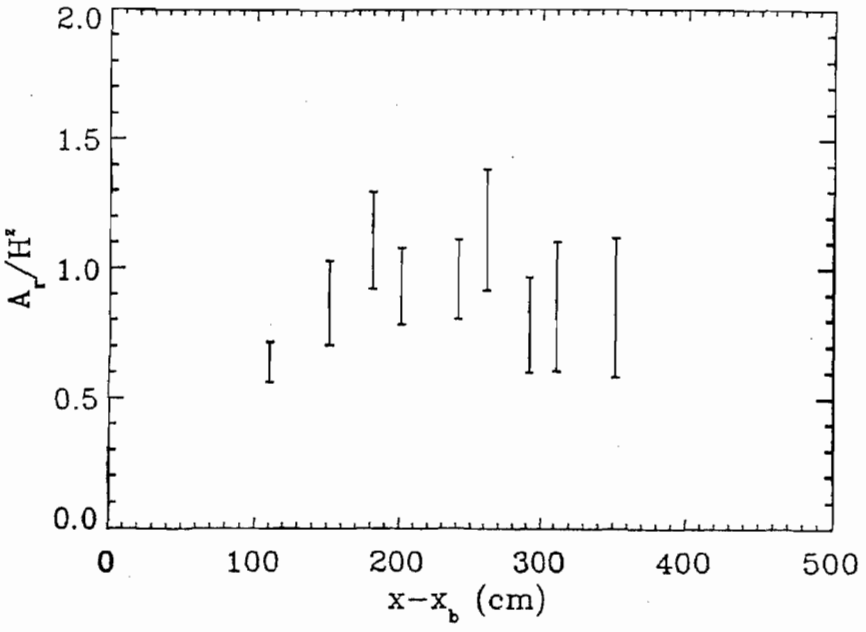

Figure 6.2: *Normalised aeration area versus position for a spilling wave as measured by Govender [1999].*

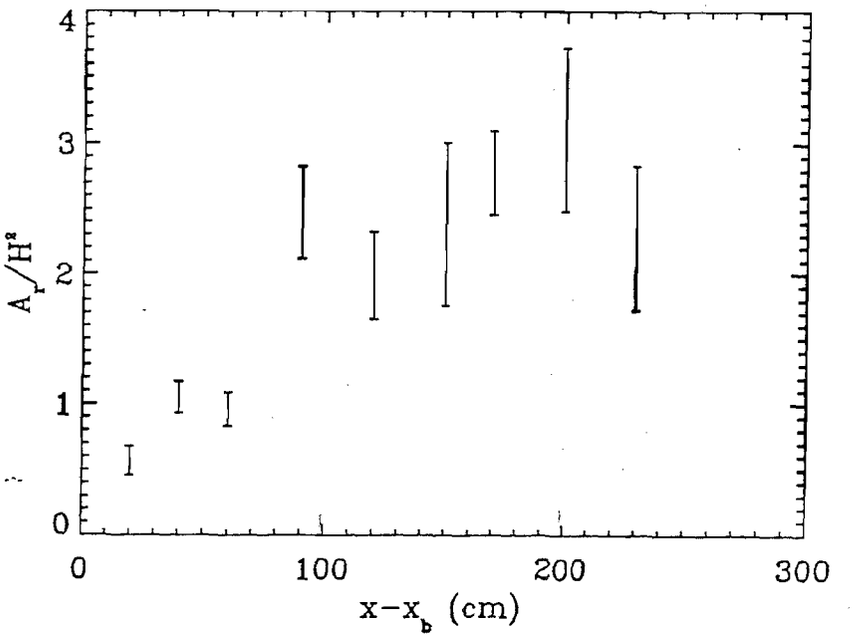

Figure 6.3: *Normalised aeration area versus position for a plunging wave as measured by Govender [1999].*

Schaffer et al. [1992] defined the boundary between the roller and the wave front (that is, the roller slope) to be a line extending from the toe of the wave front to the crest at an angle of 20^o to the horizontal. The roller was then estimated to be that body of fluid above the 20^o slope.

Measurements of the roller slope were also performed by *Govender [1999]* for spilling and plunging waves near the break point and in the surf zone. In his experiments the roller slope was found to be 15^o in the surf zone for both spilling and plunging waves. Near the break point, the slope for the spilling wave was 30^o and for the plunging wave it was 40^o.

6.3 Wave Gauge Measurements

The elevation of the water surface was measured using resistive wave gauges. At each measurement position approximately thirty wave cycles were recorded. The resulting time series measurements that were obtained in volts from the VCR were converted to a time series in centimeters, using the calibration curve described in chapter 4. The resultant data was exported to Microcal Origin[2] for analysis.

Figure 6.4 shows the measurement of the surface elevation for one cycle at three positions beyond the break point. Also shown in this figure is the estimated position of the wave front (that is, the solid dark line joining the foot of the wave front and the peak of the wave). The roller is considered to be the fluid between the solid line and the wave profile. The area is now in units of cm.s as given in Figure 6.4. The conversion from cm.s to cm^2 was performed by multiplying by the group velocity.

The area of the surface roller was calculated for each of the thirty cycles and an average value was obtained. These average values, obtained for each position beyond the break point, the corresponding wave heights as well as the area as calculated from *Svendsen's [1978]* approximation are shown in Table 6.2.

[2]A data analysis package

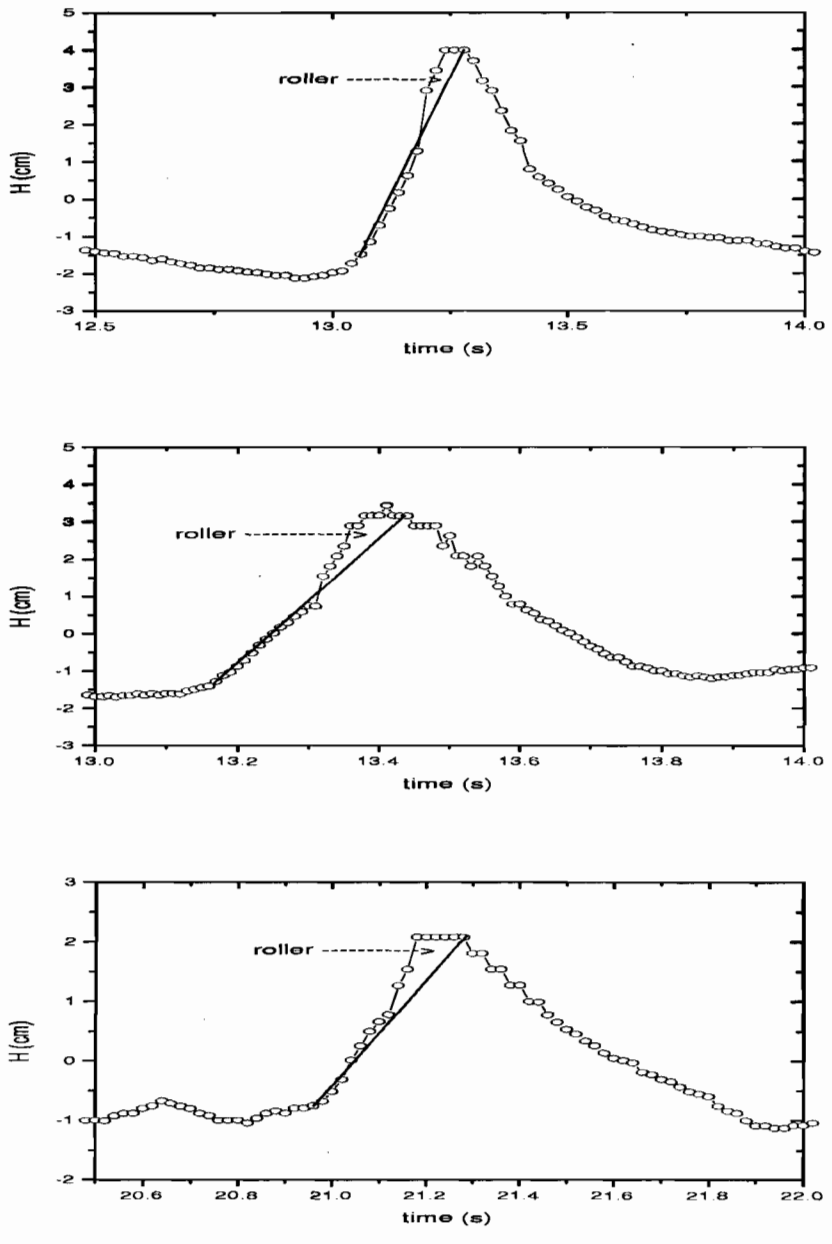

Figure 6.4: *Wave gauge measurements of the surface profile of a single cycle (from top to bottom) at* $x - x_b = 0, 40$ *and* $100\,cm$ *(o). The solid line represents the boundary between the roller and the wave front.*

Position (cm)	H (cm)	0.9 H^2 (cm^2)	Area (cm^2)	Area (Normalised)
bp	6.24	35.00	16.36	0.42
20	5.59	28.08	16.90	0.54
40	4.52	18.36	21.77	1.1
60	4.44	17.71	10.60	0.54
100	3.31	9.87	10.33	0.94
120	4.06	14.84	13.19	0.80
140	4.76	20.37	19.34	0.85
160	4.60	19.03	12.90	0.61

Table 6.2. Roller area versus position as calculated from Svendsen's approximation (column 3) and from the wave gauge measurements (column 4). The roller area normalised with respect to H^2 is given in column 5.

To see the results of Table 6.2 better, a plot of normalised area versus position is given in Figure 6.5. It is evident that at $x - x_b = 100$, 120 and 140 cm our results compare well with the literature. There a noticeable increase in the normalised area from the break point to $x - x_b = 40$ cm. The maximum is reached at $x - x_b = 40$ cm and thereafter there is a decrease in the normalised area. This behaviour can be attributed to the growth in the roller from the moment that the breaking events begin until the roller reaches its' maximum size at $x - x_b = 40$ cm. Beyond $x - x_b = 40$ cm the roller decays. Figure 6.5 is in agreement with the plots of mass, momentum and energy as given in chapter 5 where the maxima are reached at $x - x_b = 40$ cm.

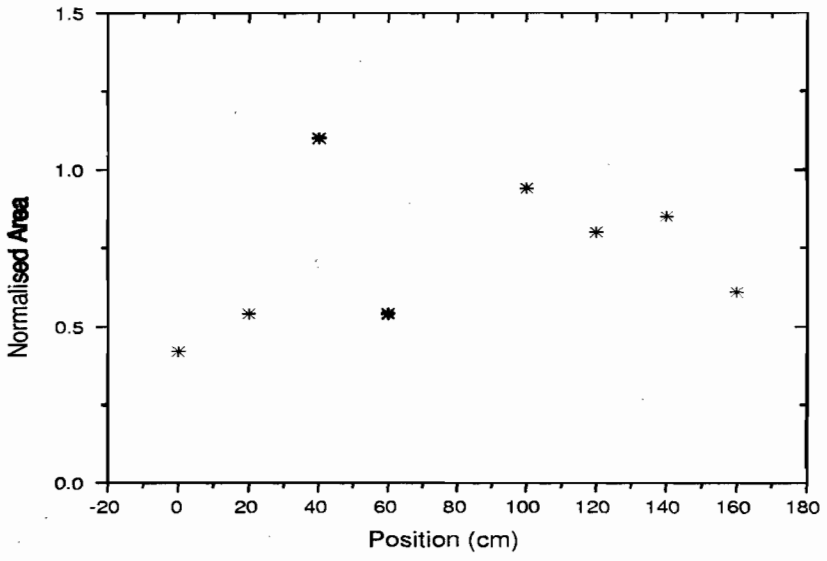

Figure 6.5: *Normalised roller area versus position beyond the break point for waves breaking over a bar in the surf zone.*

6.4 Video Measurements

Figures 6.6 and 6.7 show the video images of the waves as they pass 40−80 cm beyond the break point. These images were those taken for the Correlation Image Velocimetry (CIV) measurement and they are not consecutive images of a single wave. Rather, they are snap-shots of the wave at consecutive phase positions but each image is taken from a different wave cycle. A detailed explanation of the capture of the different phase positions is given in Chapter 5.

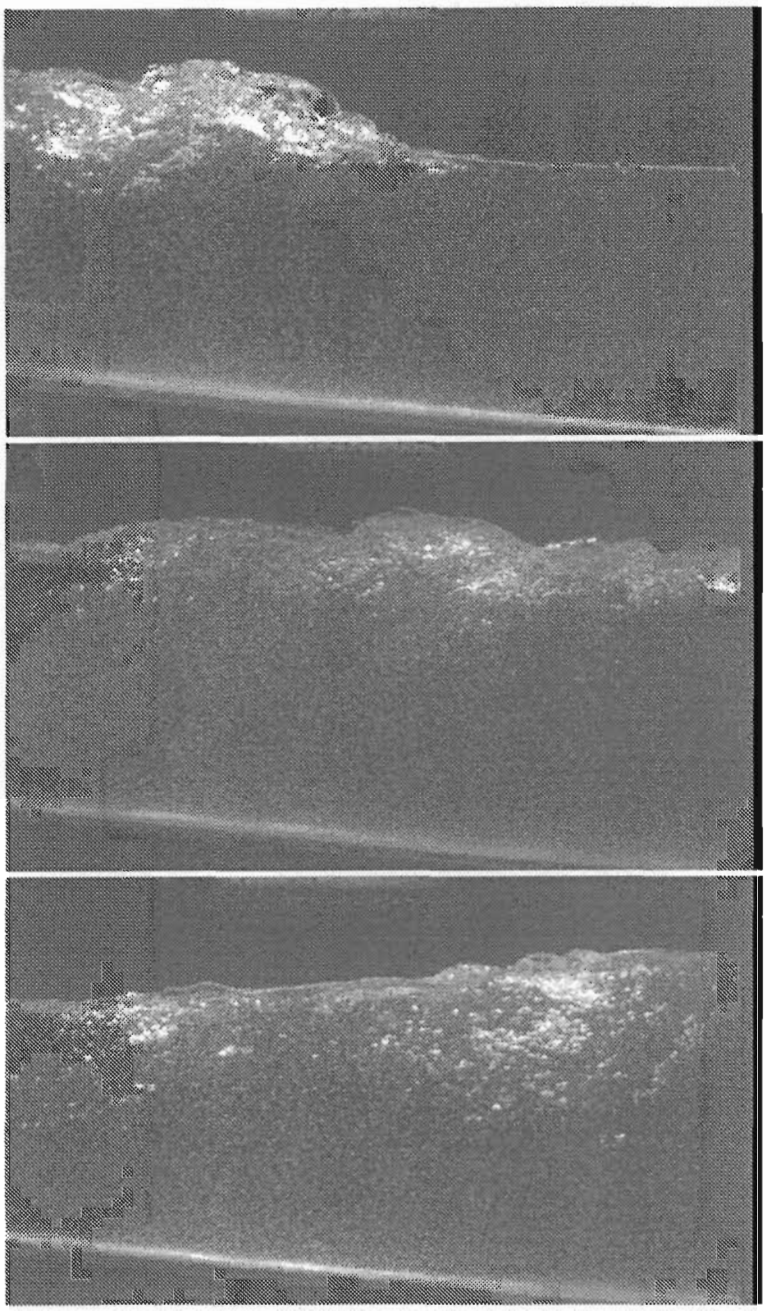

Figure 6.6: *Video images (for position* $40 - 80$ *cm beyond the break point) of different waves (from top to bottom) at wave phases* $0, 1$ *and* 2 *as captured during the CIV measurement part of the experiment.*

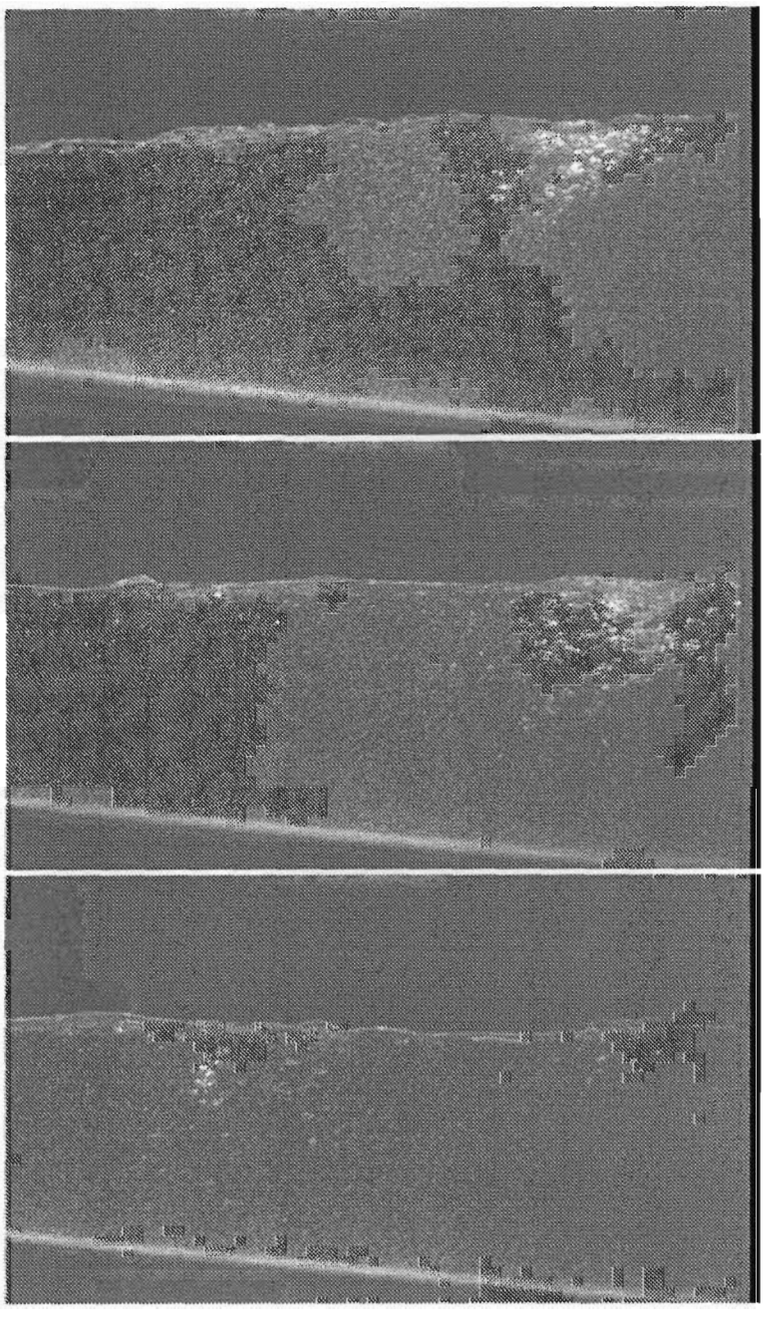

Figure 6.7: *Video images (for position* $40-80$ *cm beyond the break point) of different waves (from top to bottom) at wave phases* $3, 4$ *and* 5 *as captured during the CIV measurement part of the experiment.*

The first image of Figure 6.6 shows the wave front and the roller which is visible as a result of the entrainment of air bubbles. Present in all the images are the air bubbles indicating the spreading of the aeration over an area larger than the roller area. This would imply a lower fluid density in a larger part of the crest and not just in the roller. This spreading of the aeration is more easily seen in image 1 which is redrawn to a larger scale in Figure 6.8. In this particular image the formation of the roller is also clearly visible. The wave profile was extrapolated in the roller area by a straight line as shown in the figure.

Using only the video image containing the wave front, the roller and aeration areas are estimated as follows.

1. Using the cursor command in IDL, the profiles of the overall surface, the bottom aeration boundary and the wave front were determined.

2. The co-ordinates of these profiles were exported to Microcal Origin and the equations of the "best fit" curves were obtained.

3. The region between the overall wave profile and the lower aeration boundary is the aeration area while the roller area is the region between the surface profile and the wave front.

4. The area between two curves was determined by dividing the total area into small rectangles and summing the areas of each rectangle.

The resultant profile corresponding to the image shown in Figure 6.8 is given in Figure 6.9. The aeration and roller areas were estimated numerically using these estimated profiles. This procedure was repeated for fourteen images. The average roller area was found to be $(23.3 \pm 0.2)\,\mathrm{cm}^2$. This then corresponds to the roller area for position 40 cm from the break point and ties up closely with the wave gauge measurement. The aeration area was estimated as $(112.0 \pm 0.2)\,\mathrm{cm}^2$ and the average roller slope was found to be 16.5^o.

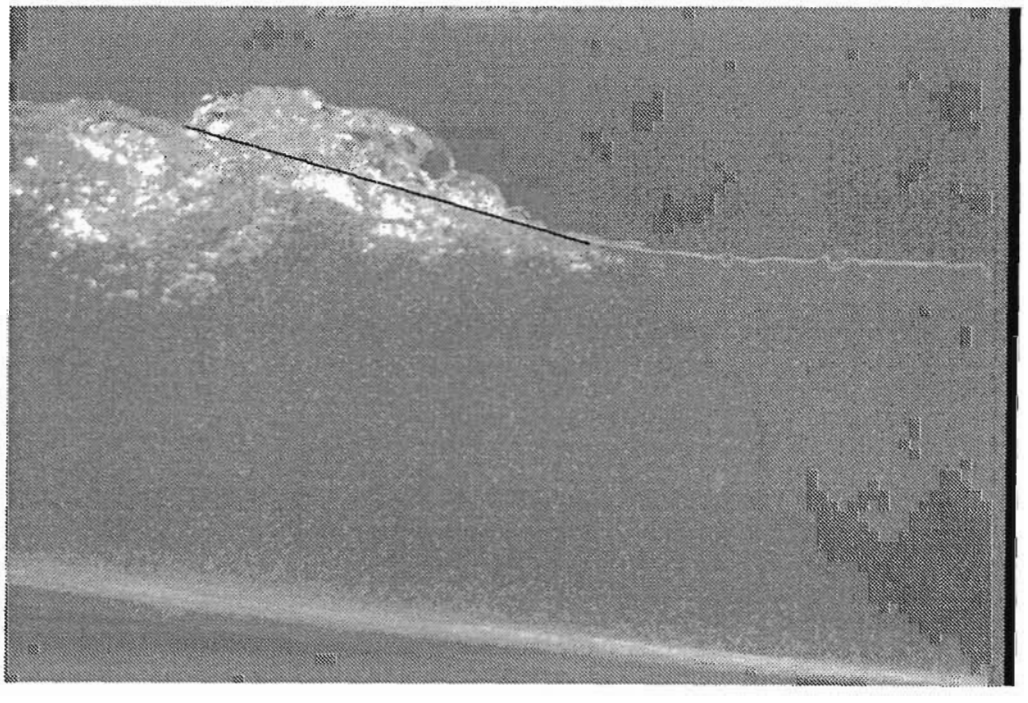

Figure 6.8: *Magnified video image of a wave at phase* 0. *The extrapolated boundary between the roller and the wave front is depicted by the solid black line.*

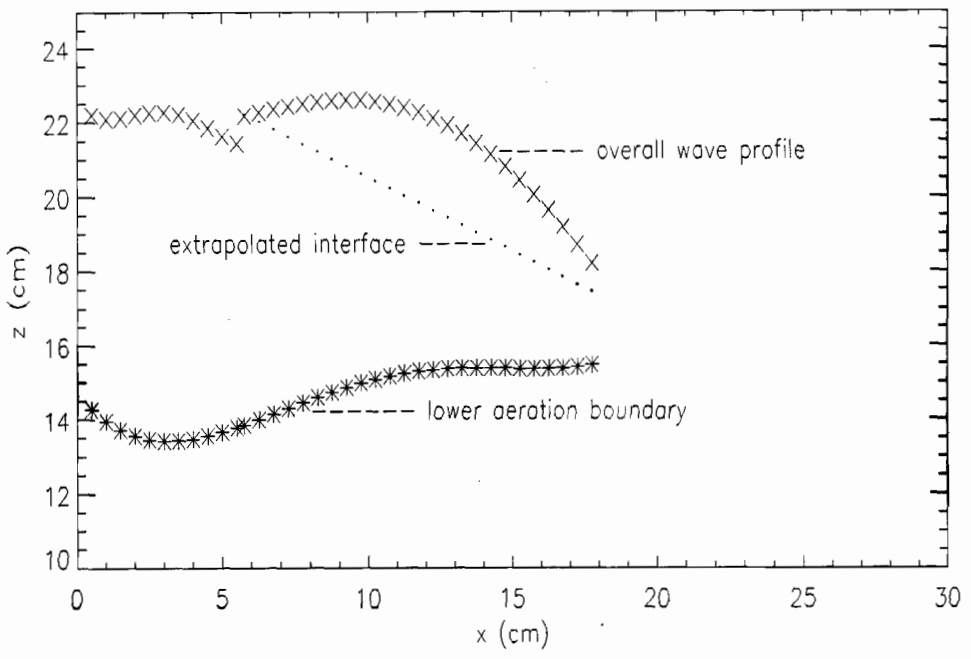

Figure 6.9: *Plot of the outlines obtained from the image shown in Figure 6.8. The crosses represent the total profile, the dotted line represents the boundary between the roller and the wave front and the asterisks represent the lower boundary of the aeration. The roller is the area between the crosses and the dots.*

6.5 Summary

In this chapter, surface rollers and aeration were investgated. Two methods of estimating the roller area have been explored. The first method utilised the wave gauge measurements of the surface elevation. Here, the estimated position of the wave front was obtained by joining the foot of the wave front to the crest. The roller was estimated to be the body of fluid between the wave profile and the estimated position of the wave front. The roller area

was found at various postions beyond the break point and the results were compared to those published in the literature.

The second method employed to determine the roller area entails the analysis of video images. Snap shots of the waves were captured as they passed by the stationary camera. The images that contained the wave front and the roller were analysed. From the images, the overall surface profile, the lower aeration boundary and the wave front profile were determined. The roller was estimated as the region between the overall surface profile and the estimated position of the wave front. The results obtained agree with the results from the wave gauge measurements. The aeration area was estimated to be the region between the overall surface profile and the lower aeration boundary.

Chapter 7

Summary and Conclusion

The experimental investigation of two dimesional waves breaking over a submerged bar in a laboratory surf zone has been presented. The actual experiment was conducted by M.J. Alport and K. Govender with funding obtained from the Joint France/South Africa Science and Technology Agreement. The author of this thesis has been involved only in the analysis of the data. The time series of the water level was measured using resistive wave gauges and the velocity flow fields were measured using video techniques. From these measurements several wave properties were investigated and these include the distribution of the mean wave height, the potential energy, the density of the aerated fluid in the crests, mass, energy and momentum fluxes, the wave energy dissipation and the roller and aeration areas.

The wave height was found to increase to reach a maximum value just before breaking. Immediately after breaking there was a decrease in wave height. From the time series measurements of the surface elevations it was observed

that the wave becomes asymmetrical as it approaches the break point. The presence of harmonics was noticed in the frequency spectra. There was a gradual decrease in potential energy prior to breaking, which was followed by a rapid decrease in potential energy in the surf zone. The rate of energy dissipation as calculated by the bore prediction and wave height analysis were compared and showed to be in agreement. Both calculations reveal a decrease in energy after breaking.

From the time-averaged flow fields it was evident that in the region soon after breaking, the velocities in the crests of the waves were larger compared to the velocities in the troughs of the waves. The maximum velocity in the crest was found to be $26\,\mathrm{cms}^{-1}$, and in the troughs it was -11 cms^{-1}. It was also evident that the profile of the undertow changes from having a maximum at the top to having its maximum velocity at the center of the profile.

The forward velocity flux in the crests of the waves was found to be larger than the reverse velocity flux below the trough level. This was due to a difference in the fluid densities in these regions. Using this difference in forward and reverse fluxes, the fractional density of the fluid in the crests was calculated to be approximately $700\,\mathrm{kgm}^{-3}$, in fact it ranges from $600\,\mathrm{kgm}^{-3}$ to $800\,\mathrm{kgm}^{-3}$ across the breaking region.

From the plot of momentum versus position from the bar the maximum momentum was found to be larger than the initial momentum. This increase in momentum may be attributed to the large increase in mass flux in the

wave roller. Also, there was an increase in kinetic energy in the region soon after breaking which was due to the initial potential energy of the wave being converted to kinetic energy during wave breaking.

The initial radiation stress in the wave due to the momentum flux is given by $\frac{S_{xx}}{\rho g} = 6.8\,\mathrm{cm}^2$. In the section far beyond the break point, the wave motion is a combination of two leading modes having the fundamental frequency f_m of the wave generator and the frequency $2f_m$ respectively. From the amplitudes of the two modes, the radiation stress (due to momentum flux) is estimated as $\frac{S_{xx}}{\rho g} = 2.7\,\mathrm{cm}^2$ which is shared between the two modes, that is, there is a loss in radiation stress across the breaking region. A maximum momentum flux of $9\,\mathrm{cm}^2$ is realised just after breaking. This momentum flux is a combination of the momentum flux of the wave plus the forward and reverse currents.

The initial wave energy $\frac{E}{\rho g} = 6.8\,\mathrm{cm}^2$ is shared equally between the potential energy and kinetic energy. In the surf zone, there is a large increase in kinetic energy and a corresponding decrease in potential energy. The increase in kinetic energy is due to the mean currents that are generated as a result of breaking. In the flat section beyond the bar crest, most of the energy is potential energy with the kinetic energy being shared between the mean forward and reverse currents, although their contribution is minimal.

Two methods of determining the roller area were explored. The first method used the wave gauge measurements of the surface elevation while the second method used video images. The wave gauge measurements showed a distinct

increase in area from the break point to $x - x_b = 40\,\text{cm}$ where the maximum was attained and thereafter a decrease in area. This pattern was attributed to the growth in the roller from the moment that the breaking events began until the roller reached its maximum size. The video measurements were performed at one position only and the results obtained tie up closely with the wave gauge measurements. The roller area was estimated to be just 21 % of the total aeration area at $x - x_b = 40\,\text{cm}$. The average roller slope at this position was found to be 16.5^o.

In conclusion, new insights into the dynamics of the upper regions of waves breaking over a submerged bar have been provided. For positions below the trough level, measurements are in agreement with those previously published in the literature. Future work in this area may include a study of turbulence phenomena associated with waves breaking over a bar.

Appendix

1. Mory M., Currents induced by breaking waves over a bar, *Modelling of Coast. and Estuarine processes*, 27-38, 1994.

2. Govender K., Velocity, vorticity and turbulence measurements in the surf zone, *PhD Thesis - Chapter 4*, 29-47, 1999.

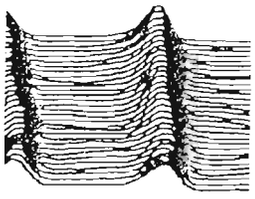

Modelling of Coastal and Estuarine Processes

Seminário Luso Francês de Modelação em Hidráulica Marítima
Séminaire Franco Portugais de Modélisation en Hydraulique Maritime
Coimbra, 11-13 July 1994

Currents induced by breaking waves over a bar

Mathieu MORY
Laboratoire des Ecoulements Géophysiques et Industriels /IMG
(Laboratoire de l'Université J. Fourier et de l'INPG, associé au CNRS)
BP 53 X, 38041 Grenoble Cédex / France

ABSTRACT

Laboratory experiments on the breaking of regular waves over a submerged bar are reported. The main scope of the paper is the measurement of the mean currents produced by breaking waves using Laser Doppler Anemometry. Their amplitude is strong in the breaking zone, reaching about 1/3 of the maximum orbital velocity. The changes in the wave over the bar is also measured using a resistivity gauge. A spectral evolution of the wave is noticed with an energy transfer to higher harmonics of the primary frequency of the wave maker. The results include the determination of the mean water level. All the results are analysed in terms of momentum flux and the respective contributions of radiation stress, mean water level set-up and set-down and momentum flux of the mean current are estimated.

1. Introduction

Long shore bars observed on beaches have been thought by various authors to be induced by wave breaking. The sediment suspension is increased in the surf zone owing to the presence of a high level of turbulence produced by the breaking waves. Breaking waves also generate mean currents which transport the sediment. The sediment is then deposited in the vicinity of the breaking point of the wave to form the bars. The present paper aims at providing laboratory measurements of the mean current produced by breaking waves over a bar. The question of sediment transport is decoupled from the question of mean current generation by breaking waves ; regular waves break over a submerged rigid bar. The emphasis is on the mean current generation by breaking waves, but other phenomena related to wave breaking in the surf zone such as set-down or set-up of mean water level and high frequency wave generation are also observed in our experiment (see Battjes, 1988, for a review of these phenomena).

In their review on wave breaking, Banner and Peregrine (1993) classified laboratory experiments on two-dimensional wave breaking into two main categories. The first are experiments that are used to predict the conditions for wave breaking (Bonmarin, 1989, among others). The second category has provided cinematic descriptions of the flow in breaking waves. Instantaneous velocity fields have been obtained by Greated et al (1992) using Particle Image Velocimetry. Averaged flow fields have also been determined by Rapp & Melville (1990). The purpose and the kind of results presented in the paper by Rapp & Melville, which is apparently the most detailed published, are similar to those presented here. Rapp & Melville analysed their experimental data in terms of momentum flux and breaking induced currents. Their experiment is, however, different. By using the two-dimensional focused wave approach in deep-water they produced a unique breaking event for each wave packet. Ensemble averages of the flow field are estimated for given times after breaking has occurred. It is therefore an averaged instantaneous flow field. This kind of averaging provides a good description of the vortex structure generated during breaking. For our part, we determine the mean time-averaged flow for regular breaking waves, i.e. the mean current. Averaged instantaneous flow fields similar to those determined by Rapp & Melville (1990) would have been obtained by averaging our velocity measurements for a given phase in a wave period.

The following of paper is divided in four sections. The experimental set-up and procedures are described in Section 2. Section 3 presents measurements of the wave changes over the bar ; the wave decomposition over the bar is characterised. Measurements of vertical profiles of the horizontal and vertical velocity components at various positions inside and outside the surf zone using Laser Doppler Anemometry are presented in Section 4. Section 5 is devoted to the discussion of the results.

component is also given in Fig. 6 but its averaged value is determined with a much lower confidence as it is much smaller than the mean horizontal velocity component. The mean current profiles were measured several times in order to test the reproducibility of measurements. Much lower estimates of the mean horizontal velocity component were measured in one case at the position x = 60 cm. This profile is also plotted in Figure 6, although it is physically doubtful, since it implies a strong upward flux between x = 45 cm and x = 74 cm. We were unable to determine *a posteriori* whether this surprising velocity profile is attributable to a misreading of the LDA apparatus or to some change in wave generation that modified the location of the breaking point over the bar.

The shape of the vertical mean velocity profile changes according to whether it is measured before breaking occurs or in the breaking zone; in the former case the return flow increases from the bottom toward the free surface whereas in the latter case the return flow is maximum near the bottom. The condition of zero mean flux across a vertical section implies that an intense mean flux in the direction of wave propagation should take place in a very thin layer below the free surface. As the crossed laser beam is not covered by the water during the whole period and as bubbles greatly disturb the velocity signal when the measurement point is close to the still water level, the velocity profiles shown in Fig. 6 are limited to depths greater than 20 mm from the still water level. The horizontal velocity component u is usually negative at z = -20 mm, but there are indications that the flow direction is positive near the surface for x = 60 cm to x = 130 cm.

The position of the mean water level relative to the still water level was determined by averaging the position of the free surface measured by resistivity probes (see Section 3). The results at the nine positions where mean velocity profiles were measured are listed in Table I. Also included in Table I is the mean water level determined at x = - 750 cm where the water depth is 40 cm and the wave is almost monochromatic (Fig. 2a). At two positions in the breaking zone (x = 45 cm and x = 60 cm), two very different estimates were obtained from two different records. Obviously, determining the mean water level in the breaking zone requires averaging over records of longer duration. The results given in Table I qualitatively agree with the classical idea according to which a significant set-down is produced just before breaking and a set-up then occurs after breaking (see Horikawa, 1988, section 5.2). The mean water level deviation from the still water level is small in our experiments outside the breaking zone. Its order of magnitude is 1 mm.

x (cm)	-750	- 7	10	25	45	60	74	95	130	195
$\bar{\eta}$ (mm)	- 1.8	- 2.3	- 3.3	- 3.9	- 1.9 4.3	-0.4 1.0	- 0.6	- 0.8	0.0	0.9

Table I: Mean water level elevation relative to the still water level.

4. Velocity measurements

The time variation of the horizontal velocity component u over 20 periods is shown in Figure 5 for two typical cases. The variations of the free surface position for the same time interval are shown in Figures 2b and 2c, respectively. The velocity record plotted in Fig. 5a is measured just before breaking occurs. The record of Figure 5b, which is measured in the breaking zone, clearly indicates production of turbulent fluctuations due to the release of potential energy during breaking. Each period is clearly distinguished, but the averaged velocity over one period slowly varies in time. It was therefore necessary to average the velocity variations over very long times in order to determine the mean velocity.

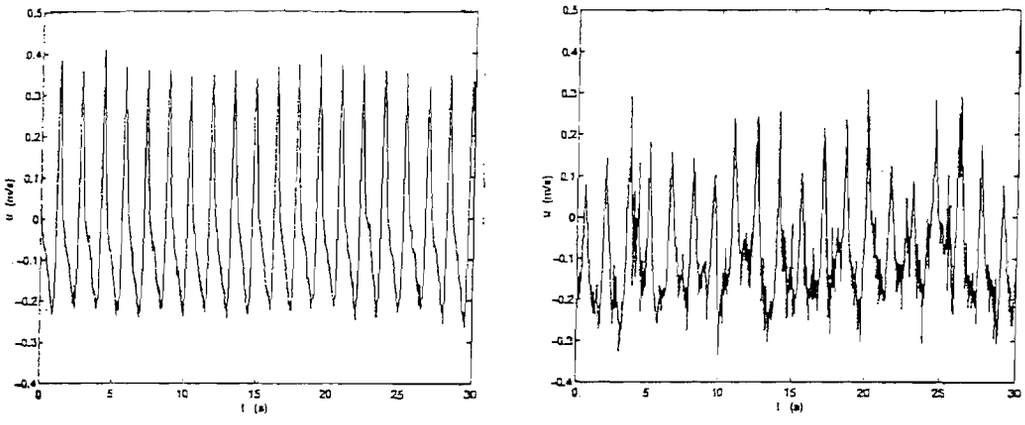

(5a). x = - 7 cm (5b). x = 45 cm

Figure 5: Variation of the horizontal velocity component u versus time. The sampling frequency is f_s = 50 Hz. The wave height is H_{40} = 7.4 cm. The velocity is measured at a depth z= - 80 mm from the still water level.

Mean velocity profiles are shown in Figure 6. In order to visualise qualitatively where the plotted vertical velocity profiles are measured in the breaking zone, a schematic drawing of the wave variation is included in the upper part of Figure 6. The shape of the wave is drawn for several times during a wave period (T=1.5s), each being a time when the wave elevation is maximum at a position on the x axis where a velocity profile has been measured. During breaking, the domain containing entrained bubbles is indicated using hatched areas. The main observation that emerges from Figure 6 is the existence of a significant mean current below the breaking wave. Mean velocities measured in the x direction reach 10 cm/s, which is comparable with the orbital velocity (of the order of 30 cm/s, see Fig. 5). The occurrence of a strong mean current is spatially limited to the breaking zone (10 cm < x < 95 cm); the undertow current is again much smaller when breaking has ended (x = 195 cm). The vertical mean velocity

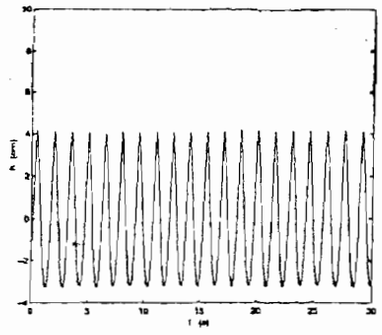

(2a). x = -7.5 m

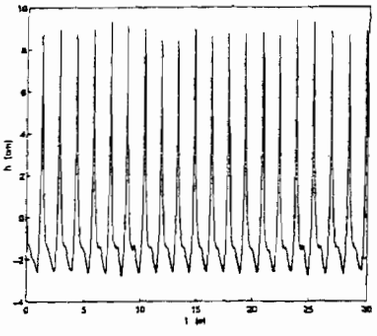

(2b). x = - 0.07 m

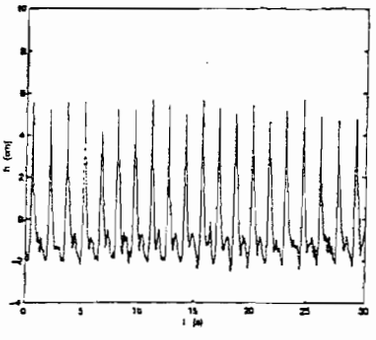

(2c). x = 0.45 m

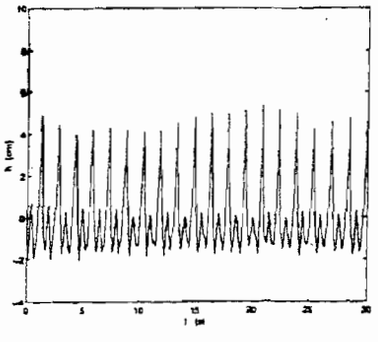

(2d). x = 1.95 m

Figure 2: Free surface displacements.

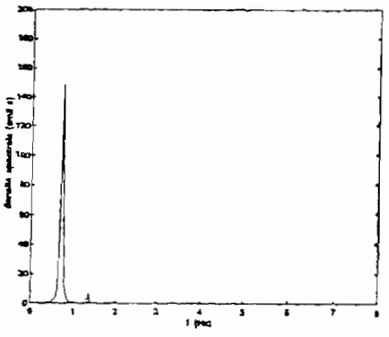

(3a). x = -7.5 m

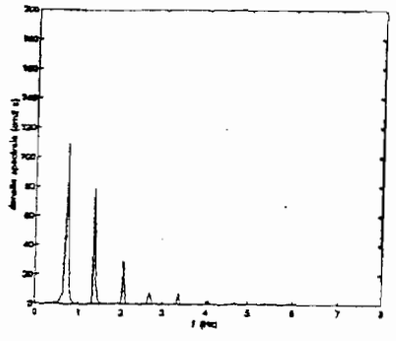

(3b). x = - 0.07 m

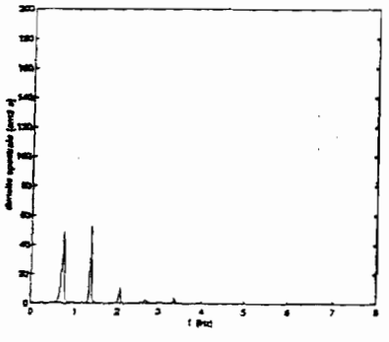

(3c). x = 0.45 m

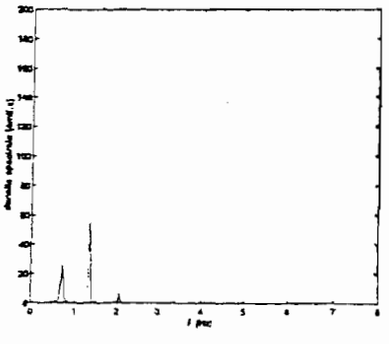

(3d). x = 1.95 m

Figure 3: Power spectra of the FFT of free surface displacements.

2. Experimental procedure

Figure 1 shows a schematic diagram of the experimental set-up. The experiments are carried out in a wave flume of length 17 m and width 0.8 m. The flume is equipped with a bottom topography of bar type. The wave maker produces regular sinusoidal waves with period T = 1.5 s. Waves propagate over a distance of 8.2 m in a water layer of constant depth h = 40 cm before they reach the upslope face (1:20) of the bar. The bar crest consists of a horizontal bottom section of length 10 cm at depth h_c = 10 cm from the still water level. After passing over the bar, the waves move over a down sloping bottom (1:10) of length 70 cm and in a section of constant depth h_t = 17 cm (length 2 m) before they reach the beach absorber. The design of the bottom topography is based on the laboratory experiments of Smith & Kraus (1990) and Beji & Battjes (1993). The upslope and downslope of the bar are chosen from Beji & Battjes; the slopes are smaller than those used by Smith and Kraus, in order to be more representative of a field bathymetry. The ratio h_t / h_c = 1.7 is identical to the value in Smith & Kraus' experiment, but in this experiment the bar is continued by a sloping beach. Beji & Battjes considered a bar crest of much greater length, because they were primarily interested in the phenomenon of high frequency wave generation over the bar. Our scope is the breaking wave over the bar through.?

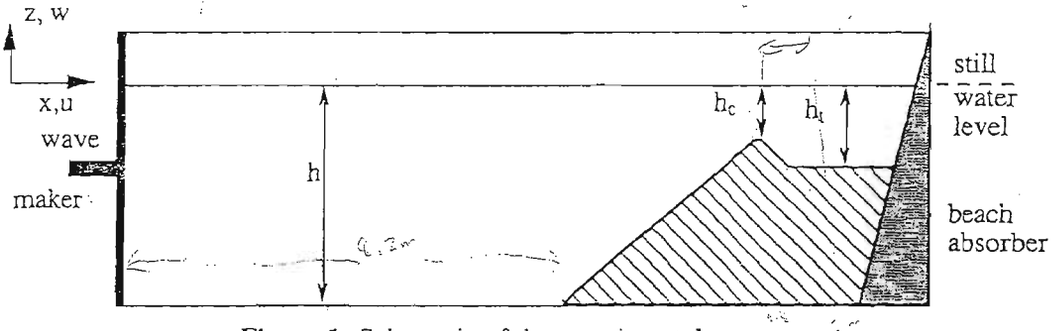

Figure 1: Schematic of the experimental set-up.

The amplitude of the wave is chosen so that the wave will break at the crest of the bar, leading to a wave height value (See section 3) in the first part of the flume (h = 40 cm) of H_{40} = 7.4 cm. An estimate of the parameter

$$\xi = \frac{\operatorname{tg}\beta}{\left[\frac{H_\infty}{L_\infty}\right]^{1/2}} \qquad (1)$$

predicts that breaking is of spilling type according to the criterion proposed by Battjes (1975) and Smith & Kraus (1990) (β is the angle of the upslope face of the bar, L_∞ the wave length and H_∞ the wave depth in infinite depth). Our observations reveal that the breaking type is

a continuous set-up after the breaking zone (85 cm < x < 195 cm). These two domains are located outside the breaking zone and the values obtained for the mean water level, though small, are reproducible estimates of the mean slope of the free surface prior to breaking and after breaking. Denoting

$$R_{\bar{\eta}}(x_0, x_1) = \int_{x_0}^{x_1} \rho g h \frac{\partial \bar{\eta}}{\partial x} dx \qquad (4)$$

the integral in the right hand side of eq. (3), we estimate (assuming that the mean water level varies linearly between two points given in table I)

$$R_{\bar{\eta}}(-750, 10) / \rho g = -2.0 \text{ cm}^2$$
$$R_{\bar{\eta}}(85, 195) / \rho g = 2.9 \text{ cm}^2$$

Evaluating the integral (4) in the breaking zone is questionable as Table I shows large variability of the data for 10 cm < x < 85 cm. Computing the integral (4) with the various data listed in Table I leads to

$$-7.7 \text{ cm}^2 < R_{\bar{\eta}}(10, 85) / \rho g < 13.1 \text{ cm}^2$$

The uncertainty is large compared to the estimated radiation stresses obtained above. This means that, although the mean water level variations are small in our experiment, they may play a significant part in the mean momentum balance. Better accuracy in the mean water level is required to be more conclusive.

We now consider a section in the breaking zone and estimate the momentum associated with the mean current. We approximate the vertical profiles of the current in the direction of wave propagation near the free surface and the return current in the deeper layer by two linear functions

$$u(z) = U \frac{(1-\delta)(z-\delta h)}{\delta^2 h} \quad \text{for} \quad 0 < z < \delta h$$
$$u(z) = U \frac{(z-\delta h)}{(1-\delta) h} \quad \text{for} \quad \delta h < z < h \qquad (5)$$

U is the velocity at the bottom, h is the depth and (1-δ)h is the depth of the return flow. The mean momentum of the mean current is then

$$P_U = \int_0^h \rho u^2(z) dz = \rho U^2 \frac{h}{3} \frac{(1-\delta)}{\delta} \qquad (6)$$

Considering the mean current measured at the position x = 60 cm (Fig. 5a), we estimate U ~ 10 cm/s and δ ~ 0.2 for a depth h = 15 cm. We then deduce $P_U / \rho g \sim 2.0$ cm². This estimate indicates that a significant part of the momentum $S_{xx,0}$ of the incident wave in the breaking zone is transmitted to the momentum of the mean current P_U. After breaking, the mean current vanishes downstream and the momentum of the mean current P_U is again transmitted to the momentum $S_{xx,1}$ of the wave which is produced.

list of references devoted to this topic and their experiments showed that high frequency generation is not specifically connected with the wave breaking over a bar. The power spectra $\Phi(f)$ are computed using the Fast Fourier Transform $\hat{\eta}(f)$ of the time variation $\eta(t)$ of the free surface position ($\Phi(f)= \hat{\eta}(f)\,\hat{\eta}^*(f)$, $\hat{\eta}^*(f)$ being the conjugate complex of $\hat{\eta}(f)$). The FFT are computed from a set of 1024 points corresponding to a record duration of about 20.5 s. While Figure 3 confirms the occurrence of surface oscillations with higher frequencies, the power spectra differ significantly from those presented by Beji and Battjes (1993). In the frequency band analysed [0.05 Hz - 25 Hz] the surface oscillations involve only frequencies that are simple harmonics of the basic frequency f_m=0.67 Hz of the wave maker. This is a surprising result when the power spectrum shown in Fig. 3c is considered; the surface displacement is measured at a place where breaking occurs and one would have expected to see a much broader spectrum due to turbulence generation. Such a behaviour was observed by Beji & Batjjes (1993). On the other hand it is surprising that all spectra obtained by Beji & Battjes are broad even when the wave does not break.

The variation of the potential energy along the flume is plotted in Figure 4. The potential energy is normalised using the potential energy estimated when the wave travels in the first part of the flume (x = -7.5 m). As shown by Fig. 3a, the potential energy there is associated with the primary mode f_m. The plot of Fig. 4 is qualitatively similar to that obtained by Beji and Battjes. At the first point plotted (x = -7 cm), which is close to the breaking point, the potential energy associated with higher frequencies has reached the level associated with the primary frequency. A significant increase of the potential energy prior to breaking can be seen as well as the subsequent very rapid decrease of the potential energy in the breaking zone. In the breaking zone and beyond the potential energy is equally distributed between the primary frequency and the higher frequencies. This is different from the observations of the Beji & Battjes experiment: the ratio of the potential energy of the primary mode to the potential energy of higher frequencies decreases in the onshore direction.

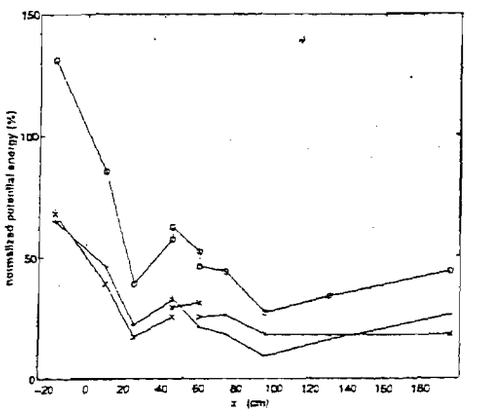

Figure 4: Spatial variation of the potential energy. (o) total potential energy, (x) potential energy of the primary mode. (+) potential energy associated with higher frequencies

5. Discussion

We estimate in this section the relative importance of wave propagation, mean water level set-up or set-down and mean flow generation by considering the mean momentum balance in a domain limited upwards by the free surface, downwards by the bottom boundary and by sections S_0 and S_1 (with respective depths h_0 and h_1) across which mean flow and wave propagation take place. A force R_x is applied at the bottom boundary which is decomposed into the mean weight of water and a dynamic force R'_x. The mean momentum balance in the domain is written

$$R_x = R'_x - \int_0^L \rho g (h+\bar{\eta}) \frac{\partial h}{\partial x} dx = I_0 - I_1 \qquad (1)$$

where I_0 and I_1 denote the mean momentum fluxes across S_0 and S_1, respectively. When a wave propagates across a section of depth h the mean momentum flux is to second order

$$I = \int_{-h}^{\bar{\eta}} \left(p + \rho u^2 \right) dz = \frac{1}{2} \rho g h^2 + \rho g h \bar{\eta} + \frac{1}{2} \rho g a^2 \left(2 \frac{C_g}{C} - \frac{1}{2} \right) \qquad (2)$$

The last term in the right hand side of equation (2) is the radiation stress S_{xx} as introduced by Longuet-Higgins and Stewart (1964), whereas the first two terms account for hydrostatic pressure effects. Combining equations (1) and (2), we deduce that

$$R'_x = S_{xx,0} - S_{xx,1} - \int_0^L \rho g h \frac{\partial \bar{\eta}}{\partial x} dx \qquad (3)$$

$S_{xx,0}$ and $S_{xx,1}$ are the radiation stresses appearing in eq. (2) if a pure wave is passing across the corresponding sections or, more generally, the dynamic part of the mean momentum flux across the section.

Our experimental results do not allow us to estimate the dynamic force in the x direction applied on the bar because the mean water level was determined only at the ten locations at which vertical velocity profiles were measured. Nevertheless several conclusions may be drawn as to the significance of the mean water level deviation from the still water level and the magnitude of the mean current in the breaking zone.

Let us first consider a domain limited by the section x = -750 cm ahead of the bar crest and by the section x = 195 cm after the bar. The mean current is negligible in these sections. The wave is nearly monochromatic in the section at x = -750 cm (Figs. 2a and 3a). The radiation stress is determined from eq. (2) : $S_{xx,0}/\rho g = 6.8$ cm^2. In the section at x = 195 cm the wave motion is a combination of two leading modes having respectively the fundamental frequency f_m of wave generation and the frequency $2f_m$ (Figs. 2d and 3d). Evaluating the amplitude of the two modes from Fig. 3d, the radiation stress is estimated to be $S_{xx,1}/\rho g = 3.0$ cm^2 nearly equally shared between the two modes. The data listed in Table I show a continuous set-down of the mean water level before the wave break (-750 cm < x < 10 cm) and

intermediate between plunging and spilling. This is not inconsistent with the predictions of Smith and Kraus (1990) and Battjes (1975).

The experimental results are based on velocity measurements performed using a two component TSI Laser Doppler Anemometer. Vertical profiles of the u and w velocity components are measured in different sections in the flume (u and w are the velocity components in the direction of wave propagation and in the upwards vertical direction), especially in the breaking zone. The time history of the two velocity components is recorded at a sampling frequency $f_S = 50$ Hz so that 75 values are obtained during each wave period. Mean currents are determined by averaging the velocity over a large number of periods. Depending on the distance of the measurement point to the free surface and on its position in or out of the breaking zone the digitised records cover 600 to 1100 wave periods. In some places, several records were made for the same conditions to test the reproducibility of averaged values.

The free surface displacements are measured using resistivity gauges and recorded simultaneously with the laser Doppler measurements at the positions in the flume where vertical profiles of the mean currents are determined. Free surface measurements aim at characterising the changes of the wave over the bar (amplitude, Fourier spectrum) and at determining the mean level of the free surface.

3. Wave changes over the bar

Typical records of free surface displacements are shown in Fig. 2, measured at four positions along the flume that correspond to different stages of the wave evolution over the bar. Figure 2a represents the wave produced by the wave maker in the first part of the tank ($h = 40$ cm). The x co-ordinate is positive in the direction of wave propagation and the origin. $x = 0$ is located at the point where the upslope reaches the crest. Figure 2b and 2c show the displacement in time of the free surface just before the wave breaks and in the breaking zone, respectively. Figure 2d characterises the wave which is reconstructed after breaking. We observe that the wave becomes very asymmetrical when travelling upslope toward the bar crest (a small asymmetry is already noticed at position $x = -7.5$ m). The wave is very steep at position $x = -7$ cm; a rough estimate of the angle of the wave with the horizontal at its crest is about 35°. In the breaking zone ($x = 45$ cm) irregular turbulent fluctuations of the free surface are observed after the breaking crest has just passed. The breaking events end at the position $x = 195$ cm and the wave recovers a regular shape with two successive crests during each basic period of 1.5 s.

Power spectra of the surface oscillations are shown in Figure 3 for the four records of Figure 2. They provide an insight into the phenomenon of high frequency generation occurring when waves propagate over bars or submerged obstacles. This phenomenon, which is due to shoaling and de-shoaling, has long been known. Beji & Battjes (1993) provided an up to date

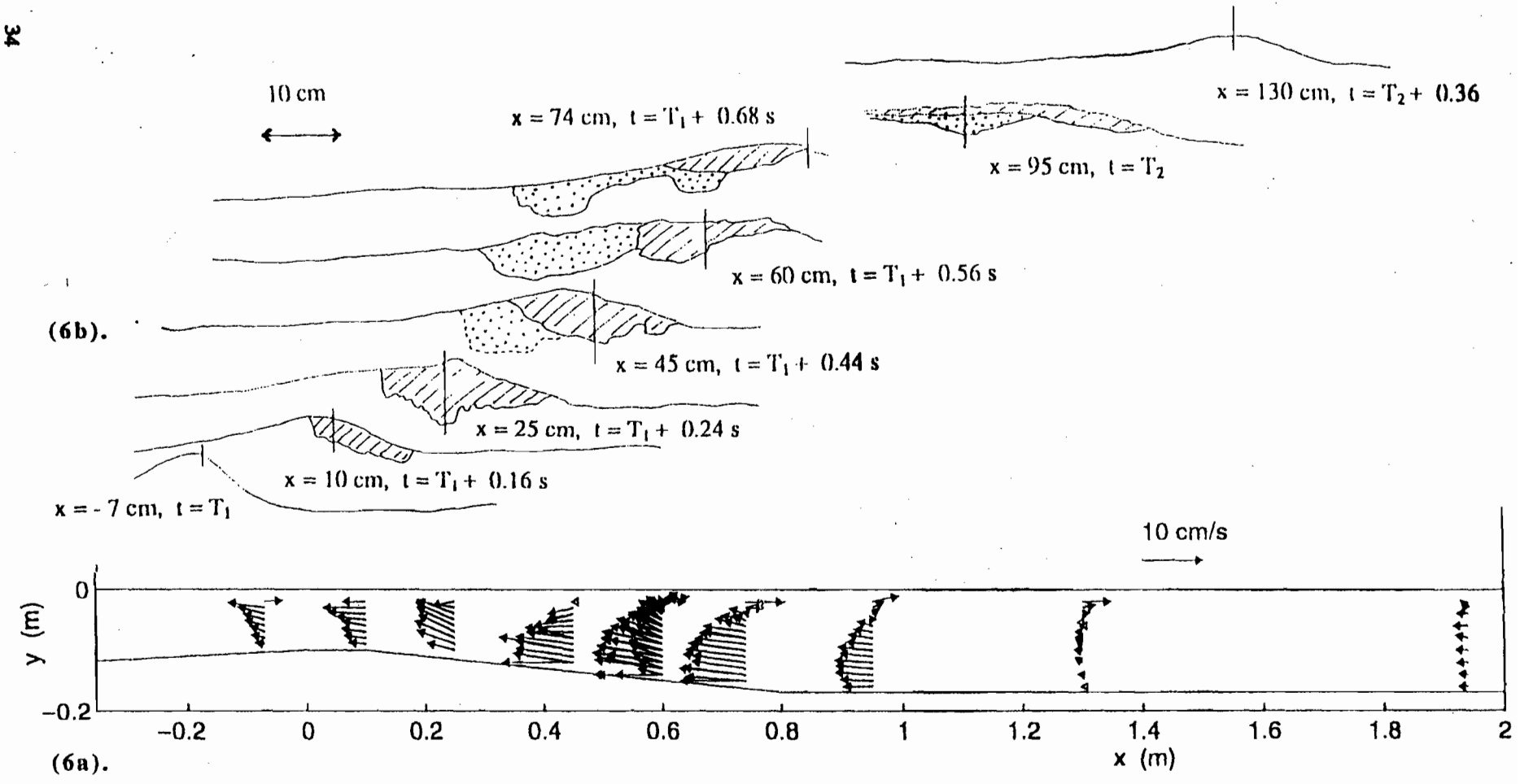

Figure 6: (6a). Vertical profiles of the mean horizontal et vertical velocity components.
Wave properties in the part of the tank with constant depth h = 40 cm : wave period T = 1.5 s, wave height H_{40} = 7.4 cm.
(6b). Qualitative evolution of the free surface. Hatched areas indicate the breaking domain. The areas identified using bubbles characterize domains where bubbles are much more dispersed than in the breaking domain.

Acknowledgements: This work was carried out as part of the G8M Coastal Morphodynamics programme. It was funded by the Commission of the European Communities, Directorate General for Science, Research and Development under Contract No. MAS2-CT-92-0027.

References

BANNER M.L. & PEREGRINE D.H. (1993) "Wave breaking in deep water", Ann. Rev. Fluid Mech., 25, pp. 373-397.

BATTJES J.A. (1975) "Surf similarity", Proceedings of the 13th Coastal engineering conference, American Society of Civil Engineers, pp466-480.

BATTJES J.A. (1988) "Surf-zone dynamics", Ann. Rev. Fluid Mech., 20, pp. 257-293.

BEJI S. & BATTJES J.A. (1993) "Experimental investigation of wave propagation over a bar", Coastal engineering, 19, pp.151-162.

BONMARIN P. (1989) "Geometric properties of deep-water breaking waves", J. Fluid Mech., 209, pp. 405-433.

GREATED C.A., EASSON W.J., QUINN P.A., SKYNER D.J. & SHE K. (1992) "Velocity measurements under 2D and 3D breaking waves using Particle Image Velocimetry", Final Workshop G6M, Pisa (Italy).

HORIKAWA K. (Editor) (1988) *Nearshore Dynamics and coastal processes*, University of Tokyo Press.

LONGUET-HIGGINS M.S. & STEWART R.W. (1964) "Radiation stresses in water waves ; a physical disccussion, with applications", Deep-Sea Res., 11, pp. 529-562.

MEI C.C. (1989) *The applied dynamics of ocean surface waves*, Advanced Series on Ocean Engineering - Vol. 1, World Scientific.

RAPP R.J. & MELVILLE W.K. (1990) "Laboratory measurements of deep water breaking waves" Phil. Trans. R. Soc. Lond., A 331, pp. 735-800.

SMITH E.R. & KRAUS N.C. (1990) "Laboratory study on macro-features of wave breaking of bars and artifical reefs", CERC Technical report 90-12.

CHAPTER 4

TECHNIQUES FOR FLUID VELOCITY AND WATER LEVEL MEASUREMENTS USING VIDEO IMAGERY

The application of digital particle image velocimetry (DPIV) and digital correlation image velocimetry (DCIV) to the measurement of the velocity flow field of breaking water waves in a two dimensional wave flume is described. The basic optical aspects are reviewed with regards to particle position estimation and significant features of the system components are described. The estimation of particle velocities is accomplished by exploiting the construction of a TV image and by the use of strobing techniques. Improvements in spatial resolution are achieved by using sub-pixel position estimation. The measurement of the time series of the water elevation is also discussed. A keogram is generated from a recording of the wave, from which the time series is extracted by tracking the evolution of the air-water interface. Measurement of the roller area of a plunging wave, an important parameter for mass and momentum flux determinations, is also extracted using the keogram concept.

4.1 Introduction

In this chapter we describe the measurement of the time series of the surface wave and the velocity flow field of waves in a laboratory surf zone using digital image and analysis techniques developed by author and co-workers (*Govender et al, 1998*).

The application of imaging techniques to experiments in fluids has increased in popularity in recent years due to the advancement in digital technology. The figure below illustrates the major components of an imaging system, consisting of the object plane, the camera lens and the image plane. The object plane will contain the physical object and the image plane will contain the focused image of the object. The position of the object and image planes are governed by the simple relation $1/d_0+1/d_i=1/f$, where f is the focal length of the camera lens, and d_0 and d_i are the position of the object and image planes, respectively, with respect to the lens.

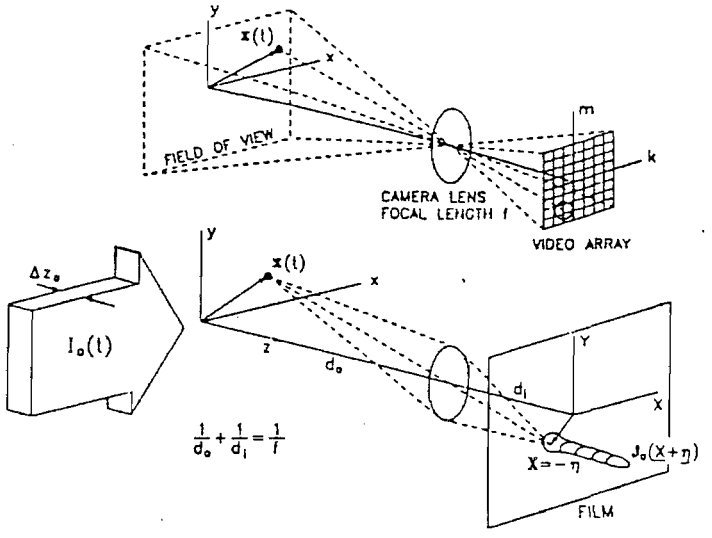

Figure 4.1: Geometry of the imaging system. (Top) Video recording, (bottom) photographic recording (*Adrian, 1991*).

Early application of imaging systems in fluid mechanics utilised photographic film to record the image formed at the image plane. A transformation exists that transforms positions in the object plane, xy plane, to the image plane, XY plane.

Modern systems, however, employ a sensor array consisting of charge coupled devices (CCD) arranged in a rectangular array. In this case a sampled version of the image is obtained. Each sample is then referred to as a pixel. Position in the image plane will then be in terms of pixels. The intensity of each pixel is then digitised and is represented as a binary value. The entire image is then represented as matrix of numbers.

Measurements of object motion then involves tracking the object in the image plane and, by suitable transformations, determine the motion of the object in the object plane. The DPIV technique involves capturing the instantaneous image of a large number of submerged neutrally buoyant seeds at two or more time instances. The velocity is then computed using the displacements that these particles have incurred over the known time intervals. This clearly requires the existence of particles to be imaged in the field of view, and a method of recording and processing these images. There are essentially two types of possible image analysis techniques; In situations where the density of seed particles are low, individual tracking of particle images is required, whilst in cases of high seed densities, 2D cross correlation techniques are employed to track the image of a group of particles. Both these techniques are described here.

In the past, most PIV systems have used photographic film for image recording and optical methods for processing. This provides a high spatial resolution measurement of particle positions. Current CCD camera technology on the other hand, does not provide a high spatial resolution. Typically, a consumer grade CCD face plate has a resolution of $\approx$ 760 x 680 pixels. However, a significant improvement in spatial resolution can be achieved by the appropriate choice of seed particle size, exposure times, and the use of sub-pixel position estimation techniques. This digital version of PIV has certain advantages over the film based method, such as reduced cost and real time processing of the data. The spatial resolution is also bound to improve with advancements in image sensor technology.

Section 4.2 provides details of velocity measurements in the surf zone using DPIV. Here the discussion is centred around the choice of various system components and the method of analysing the images using individual particle tracking and 2D cross correlation techniques. It is also shown that it is possible, using high sampling rates and the cross correlation method of analysis, to use the bubbles created during breaking to form the necessary structure for tracking purposes. This is certainly a breakthrough, since there is to date a scarcity of velocity measurements in the highly aerated region of a breaking wave. Results of phase averaged and instantaneous velocity flow fields for a spilling and plunging wave, respectively, are provided.

We also report here on a method for measuring the time series of water elevation suitable for studying wave propagation in a 2D wave flume. This method involves imaging the wave from the side and exploiting the gradient in the grey level intensity of the image across the air-water interface. The time series at a particular position is obtained by first generating a keogram from a video recording of the wave. This technique is also used to estimate the size of the roller formed in the bore of the wave during breaking. The concept of keograms and the method of extracting the time series of the wave are explained in Section 4.3.

4.2 Velocity measurement using particle image velocimetry (PIV)

As mentioned in the Introduction, PIV involves the tracking of suspended seed particles. This implies observing the position of the particles at two or more time instances. The velocity, v, of the i^{th} particle at position $x=(x,y)$ is then

$$v(x,\theta)=\frac{x(t+\Delta t)-x(t)}{\Delta t} \tag{4.1}$$

The phase, θ, is required in order to bin the velocity estimate with respect to the wave phase. For the technique to be effective, there are a number of inter-related issues that need to be addressed. The choice of one component can seriously effect the performance of other components in the system. Figure 4.2 shows a schematic view of the experimental setup.

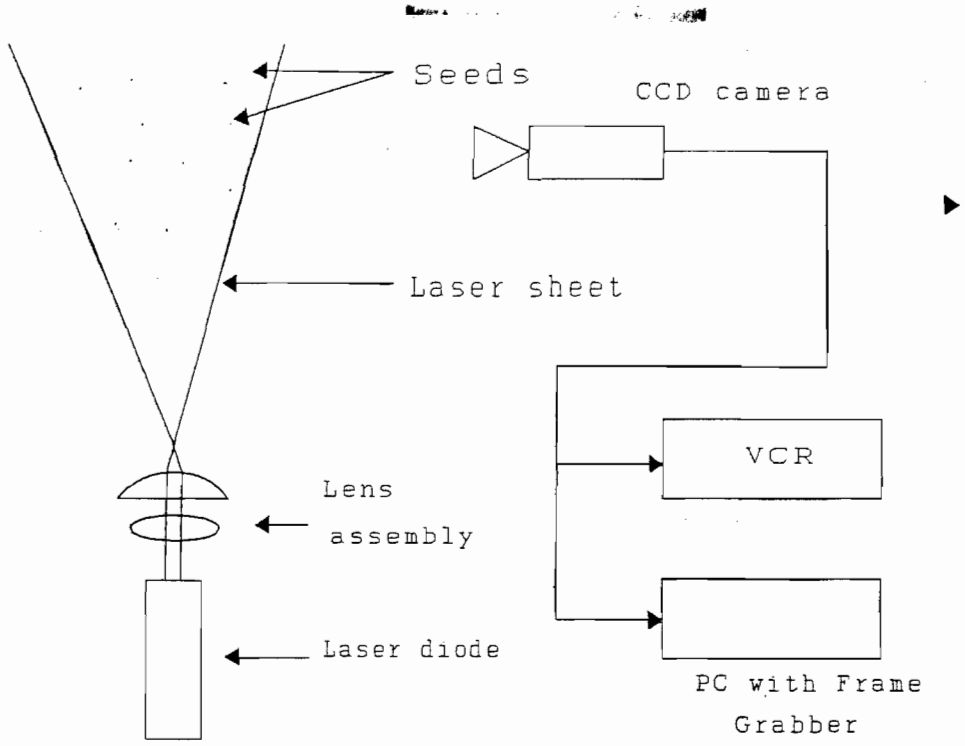

Figure 4.2:: Experimental arrangement for the measurement of fluid velocities using particle image velocimetry.

The light sheet is used to illuminate those particles that are within the focal plane of the camera. The composite video output of the CCD camera is connected to a Video Cassette Recorder (VCR) and also to a PC containing a digital frame grabber card. In most PIV applications a laser is used as a source for the light sheet, however, in applications where the coherent properties of a laser is not essential, it is possible to use ordinary white light. The following issues are of importance when setting up a PIV system:

1. Optical considerations,
2. Choice of seed particles,
3. Laser source characteristics,
4. Video processing equipment, and
5. The analysis of the images.

We will examine each of the above items with application to surf zone measurements.

A. Optical Considerations

The geometry of the optical system and the focusing lens determines the position of the object and image planes. The object plane will in this case coincide with the plane of the laser sheet. The video sensor array is located in the image plane. The distance from the lens to the image plane is typically 4 to 16 mm. The object distance will be in the range of a few centimetres to a few metres. The sensor array consists of a matrix of charge coupled devices (CCD). Most commercial devices have approximately 760 x 680 pixel elements on the die having overall dimensions of 7 mm x 5 mm. This results in a pixel spacing of 12 μm. The rate at which images are captured gives an upper bound to the system's temporal resolution. This will be discussed at length in a later section.

The image of a point source in the object plane is an Airy distribution consisting of a bright central region, the Airy disk, with a number of concentric dark and bright rings. The Airy disk, which is referred to as the point spread function (PSF), has a diameter given by (*Adrian and Yao, 1985*):

$$d_s = 2.44(M+1)f^{\#}\lambda \tag{4.2}$$

where $f^{\#}$ is the f number of the camera lens, λ is the wavelength of the light and M the magnification of the camera. Most CCD cameras with a sensor array such as that described above typically have a magnification that is less than or equal to one.

In order to understand the impact of sampling the image via the CCD array it is necessary to evaluate the optical processes occurring at the sensor. Consider the image intensity of the point source at the image plane of the lens to be $I(x,t)$ in W/m^2. The point spread function can be approximated by a gaussian function:

$$I(x,y) = C\exp(-2\frac{(x-a)^2+(y-b)^2}{\sigma}) \tag{4.3}$$

where the width and height are characterised by the parameters, σ, and, C, respectively, and (a,b) represents the offset from the origin. The exposure then is given by:

$$\varepsilon(x) = \int_0^T I(x,t)dx \tag{4.4}$$

where T is the exposure time.

Now if the point source is moving to the right with velocity $v=(v_x, v_y)$ we write for the image intensity:

$$\begin{aligned} I(x,t) &= I(x-v_x t, y-v_y t) \\ &= C \exp\left(\frac{-2(x-a-v_x t)^2+(y-b-v_y t)^2}{\sigma}\right) \end{aligned} \tag{4.5}$$

and the exposure thus being:

$$\begin{aligned} \varepsilon(x,y) &= \int_0^T I(x-v_x t, y-v_y t)dt \\ &= \int_0^T C \exp\left(\frac{-2(x-a-v_x t)^2+(y-b-v_y t)^2}{\sigma}\right)dt \end{aligned} \tag{4.6}$$

Thus, there is a smearing out of the instantaneous PSF during the integration time.

The image of a moving particle can also be viewed as a convolution between the point spread function and an aperture function. This can be easily seen by considering only the x-dependence of the integral in Equation 4.6, using the substitution $s=v_x t$, to give:

$$\varepsilon(x) = \int_{-\infty}^{\infty} w(x)I(x-s)ds \tag{4.7}$$

where

$$w(x)=\begin{cases} 1/v_x & for \;\; x_i \le x \le x_i + v_x T \\ 0 & otherwise \end{cases} \qquad (4.8)$$

and v_x =particle velocity, T =exposure time, x_i = initial particle position and $I(x)$ is the one-dimensional point spread function. Equations 4.7 and 4.8 shows that the intensity due to a moving particle is inversely proportional to its velocity. The exposure of an hypothetical particle, having a PSF given by Equation 4.3 with σ= 10.0 and C=1.0 and moving to the right with a velocity v=1.0 pixels/s, is computed using Equation 4.7 for three different exposure times. The result is shown in Figure 4.4.

From Figure 4.4 it can be seen that the image will retain most of its gaussian characteristics for exposures less than some critical value. The image will have a flat top for exposures above this critical exposure. For very much shorter exposures, the height of the gaussian is attenuated. This behaviour is exploited in sub-pixel resolution estimation discussed later.

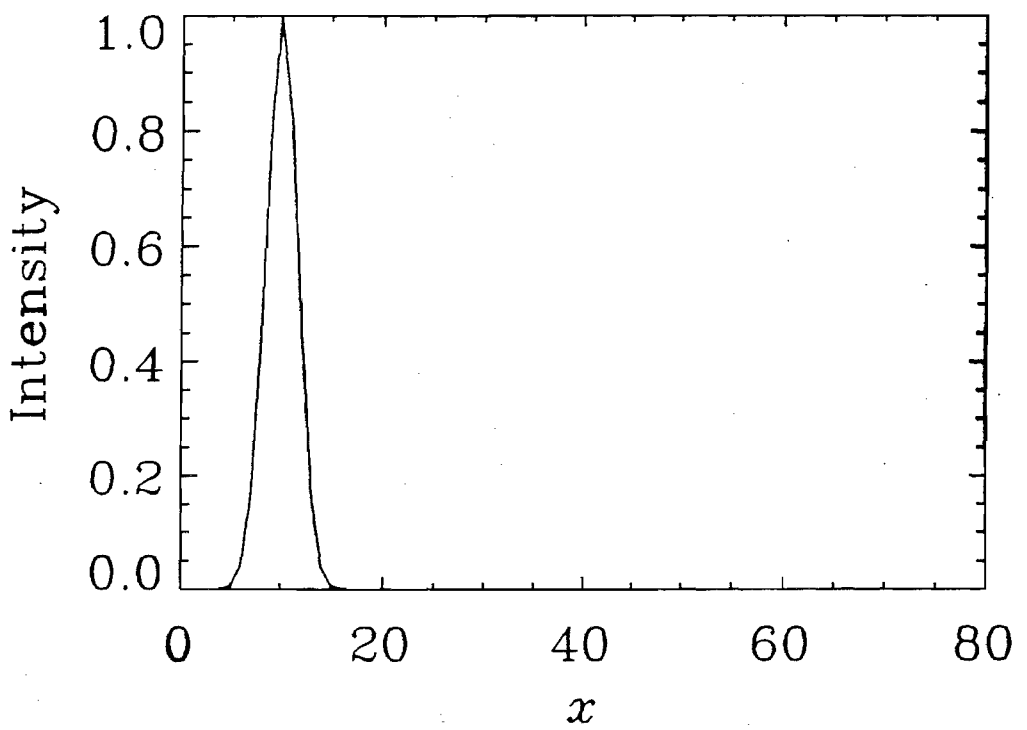

Figure 4.3: Point spread function of an hypothetical particle.

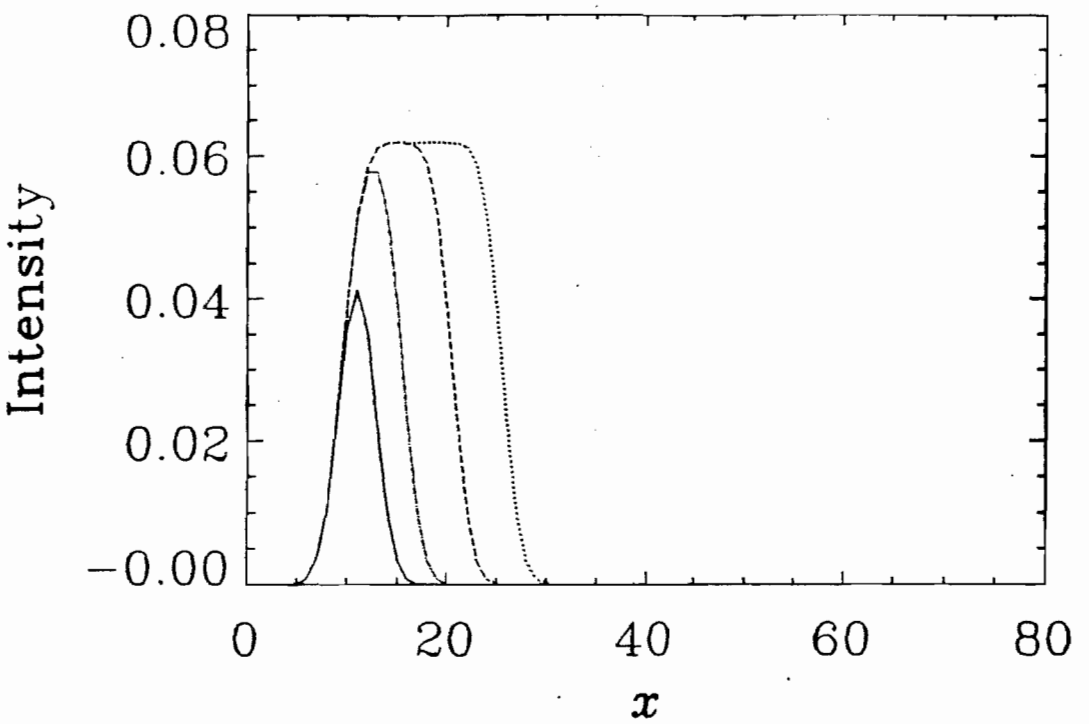

Figure 4.4: Exposure for a particle, with PSF given in figure 4.3, moving to the right. The solid, dash-dotted, dashed and dotted lines represent exposures $T_1 < T_2 < T_3 < T_4$.

B. Seed Particles

Most PIV systems to date have been used in gas dynamics and other flow regimes where the velocity field is to a large extent deterministic and predominately two dimensional. In these instances a few snapshots are essentially all that is required. In gas dynamics, one is dealing with very high velocities and the seed particles should possess dynamic properties similar to the gas under test. This puts a limit on the maximum seed particle size, typically a few microns in diameter. This small particle size then requires the use of a high power laser source, typically a few watts.

The surf zone, however, has a completely different character. Firstly, the processes occurring are highly turbulent. Statistical techniques are therefore required, implying long observation times in order to extract average and rms quantities. Furthermore, because there is a net onshore mass and momentum towards the beach due to breaking in the region above the wave trough there results a net reverse offshore flow (undertow) below the approximate

trough level. This implies that a given volume of water never stays in a fixed region for long. This in turn implies that seed particles added to the water in a particular region will eventually move out, some ending up on the beach and some accumulating at the breakpoint. Therefore a constant supply of particles is required in order to maintain a constant seed density at the point of observation. Thirdly, air bubbles are a characteristic feature of wave breaking in the surf zone. These appear as white patches or streaks in the image which obscure the seed trajectories. It will be shown later that it is possible, using correlation techniques, to determine the velocity flow field by tracking the structure created by the presence of bubbles.

It was discovered, after experimenting with a number of macroscopic particles, that un-expanded polystyrene beads, which were heated in water at a temperature of around 86° C for approximately 30 seconds, were most suitable. These partially expanded beads, approximately 0.8 mm in diameter, function well as seed particles since they are almost neutrally buoyant and their white matt surface makes them good point source scatterers.

C. Laser characteristics

The laser optical power output and frequency are dictated by the seed size, and the spectral response of the camera. Blue/green lasers are most suitable for transmission in water, since these incur the least attenuation. Since these are usually gas lasers, they are not so easily available in compact form. On the other hand red lasers are more compact, and available in a variety of lasing materials, i.e., HeNe, ruby and semiconductor diode lasers.

A 633 nm laser is closely matched to the human eye's response, but these tend to be more expensive. Monochrome video cameras typically have a broader spectral response, thus making it feasible to use a less expensive, longer wavelength, laser. In this particular case a 5 mW, 670 nm semiconductor laser diode was used in conjunction with a monochrome CCD camera having a sensitivity of 0.005 lux. The compactness of the diode laser allows for it to be installed in the bed of the flume, encased in a water tight container.

The generation of a laser sheet of light is easily accomplished using a system of cylindrical lenses. A single cylindrical lens will generate a V shaped laser sheet having a fan angles of

5 -30°.

D. Video Processing Equipment

Some of the essential features of the camera have already been highlighted. A large CCD sensor array is required for good spatial resolution. A camera with a high sensitivity and spectral response that is matched to the image is also desirable.

The images from the camera can be recorded on video tape or stored on hard disk in digital form. In the latter case, the camera output is connected direct to a frame grabber residing in a PC for digitising and storage. The video tape is a high density storage medium and allows for the cost effective archiving of large volumes of raw experimental video data. The video tape, however, does suffer from wear and tear and is subject to stretching, resulting in the distortion of images. There are certain essential features which must be considered when selecting a frame grabber for a PIV application. The frame grabber should operate without significant sampling jitter and should digitise both the even and odd fields of each video frame.

The digitised images can then be analysed using any one of the image processing packages available commercially such as IDL[1]. Typically, each frame is saved in BMP format as a separate file. These files are then read in and converted into binary data arrays by IDL for analysis.

E. Analysis Procedure for low seed density applications

The preferred method of estimating the seed velocity from the captured images is dependent on the density of seed particles. For very high seed densities, where the image of the seeds in two consecutive frames overlap, correlation analysis is usually used and this method will be discussed later. For very low seed densities tracking of individual seed is required. In this section discussion will pertain to the low seed density regime and two methods for tracking particle positions in this regime are described. As will be discussed below there are three possible sampling rates that can be achieved, viz., 20 ms using even/odd field analysis, > 20 ms where the images are separated by multiples of the frame period, and < 20 ms where a laser strobes the seeds during a single frame period.

1 Interactive Data Language.

Frame analysis

The frame analysis method exploits the underlying structure of the PAL TV format. A single TV image consists of a frame that is made up of an even and odd field. These fields are interlaced on the screen to provide a picture of reasonable definition whilst at the same time minimising the transmission bandwidth requirements. The picture is continuously updated with the even and odd fields being alternatively displayed at a rate of 50 Hz. Thus the time interval between consecutive even and odd fields is 20 ms.

Thus, from a single frame, it is possible to extract either the even or odd fields of the particle by selecting the even and odd lines respectively. By correctly matching particles with nearest neighbours, the displacement of each particle can be determined. If particle velocities are small then it is necessary to make observations over a longer time interval. In this case we could observe particle position in two fields separated by an integral number of field time periods.

The duration of the integration time of the light on CCD face plate during each field will determine the shape of the images of the particles. Clearly, short time exposures will freeze the seed images which will then appear as dots, while long exposures result in streaks. This additional streak length information is useful in finding matching pairs of particles, since the particles in each pair should have a streak of similar length and angle of inclination.

Figures 4.5 (a) and (b) show examples of streaked seed images appearing in two consecutive even fields. It can be seen that not every particle in the first image can unambiguously form a pair with its partner in the second image. This can be more clearly seen by subtracting the second image from the first, as is shown in Figure 4.5(c). In this subtracted image, the images of seeds from the first image, labelled A_1, B_1, C_1, D_1 and E_1, appear white, while those from the later image, labelled A_2, B_2, C_2, D_2 and E_2, appear black. The reasons why there is no matching seed for some of the images may be explained in the following way.

Although the flow field in the surf zone is predominantly two-dimensional there is a measure of three dimensionality, particularly in turbulent regions. The velocity component perpendicular to the laser sheet is, however, a lot smaller than those in the plane of the sheet.

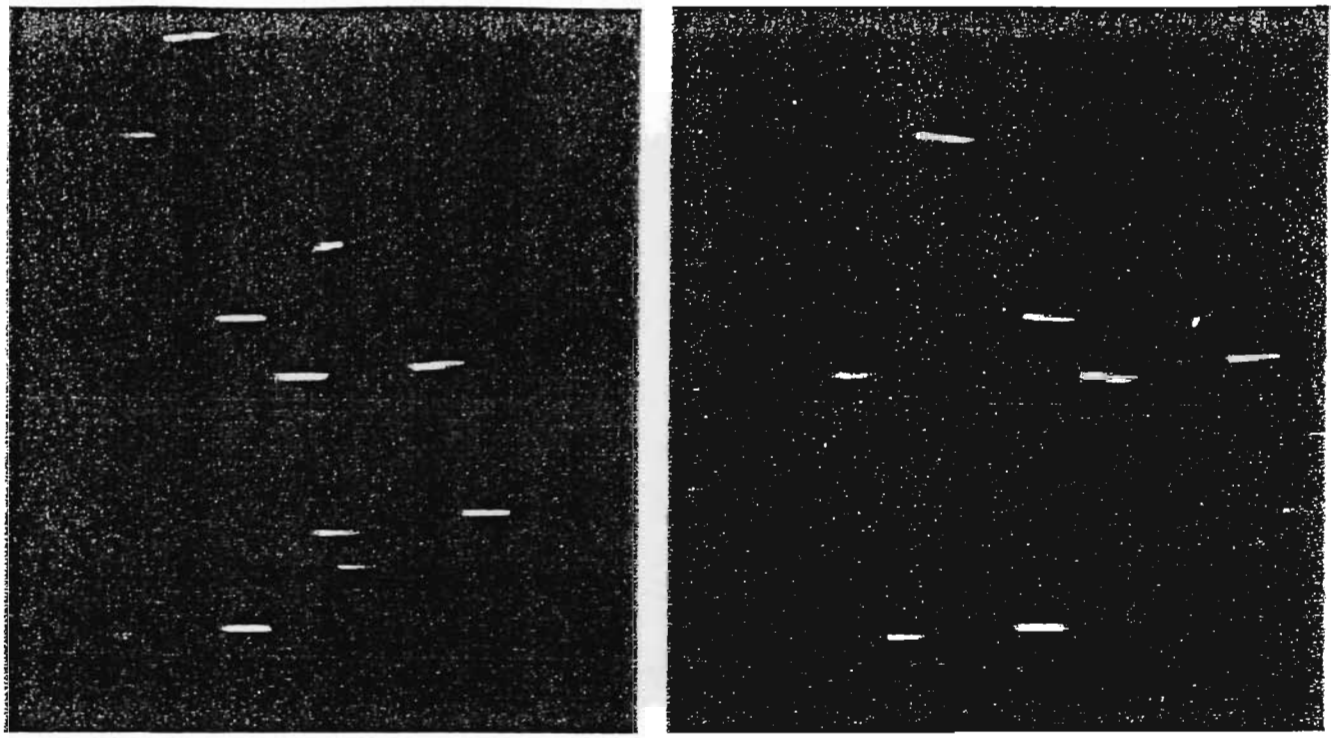

(a) (b)

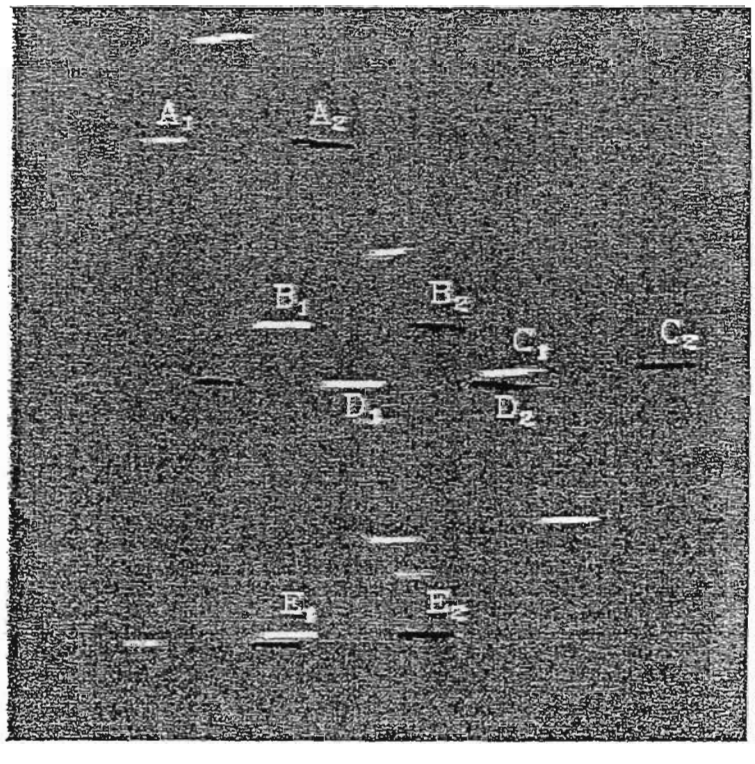

(c)

Figure 4.5: (a) First image of particle streaks, (b) second image of particle streaks and (c) image resulting from subtracting the second image from the first, matching pairs are labelled A-E with subscripts denoting the original image in which they occur.

Figure 4.6 depicts the geometry of the laser sheet and the motion of a seed. In order to find a matching pair, a particle needs to remain in the sheet for one field/frame period, τ. This then restricts the measurement to those particles with $v_y < (d-y_i)/\tau$, where v_y is the component of velocity perpendicular to the sheet and y_i is initial position of the particle. Those particles with $v_y \geq (d-y_i)/\tau$ will not stay in the sheet long enough for them to appear in two consecutive fields/frames. Thus the reason why some seeds are in the first image and not in the second, or visa versa, is because they enter or leave the sheet within the field/frame period. Also, particles with very high velocities, travel greater distances, thus making it more probable that they leave the sheet which in turn makes it difficult to find matching pairs. The absence of complete seed pairs in Figure 4.5(c) does illustrate one of the limitations of velocity estimation using field tracking.

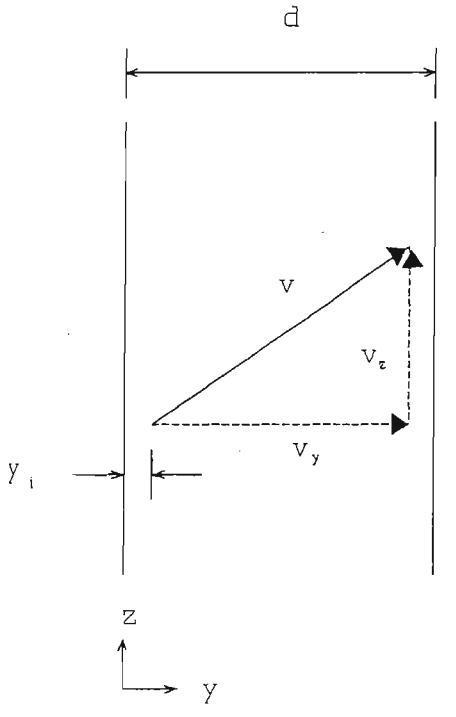

Figure 4.6: Geometry of the laser sheet and particle motion. d is the width of the sheet, y_i is the initial position of particle, and v_y and v_z are the components of velocity in the y and z directions, respectively.

Laser strobing

When the component of velocity perpendicular to the laser sheet becomes large, such as in the turbulent region during the breaking of a wave, then the frame analysis procedure

discussed above fails due to the fact that sufficient particles do not stay in the laser sheet long enough. In this case it is necessary to observe the position of the particle over a shorter time interval. This can be accomplished by strobing the laser sheet within each TV field. Since the laser is strobed a number of times during one field scan, it is necessary to ensure that the electronic shutter is open during the whole field period. Using a symmetric strobe, without any other prior knowledge about the velocity field, results in an unavoidable 180° ambiguity with respect to the direction of the observed velocity. The coded strobe technique offers a way of removing this ambiguity by varying the length of the strobe pulses. There are various methods to accomplish this (*Adrian, 1991*). The directional ambiguity is completely removed if at least three different strobe lengths are repeatedly generated and the particle does not experience a sufficiently high acceleration in a single frame period and thus cause the illuminated particle track to masquerade as a different pulse length. Another potential problem is that, although the particle is being illuminated by a long pulse, its track may appear as a short one if it enters or exits the sheet while it is being illuminated. In order to reduce errors caused by particles crossing the sheet boundary, it thus helps to select those particle images that have at least four tracks. Figure 4.7 shows the chosen pulse lengths where the pulse to be τ, 2τ and 3τ.

Strobing of the laser is accomplished by mechanically rotating a slotted disc in the path of the laser beam. Modern laser diodes can be strobed electrically. This can be an advantage, since strobing can be synchronised with the TV field scan rate and is much more accurate in controlling pulse lengths. In either case the image of the moving particle under strobed illumination is then a series of broken streaks; the length of each segment being dependent on both the pulse length and the seed's velocity. The direction of motion can be inferred by examining the sequence of the line segments. If the particle image spans only a few pixels on the CCD sensor, due to its low velocity, then it might become difficult to distinguish difference between lengths. A way around this difficulty is to use the fact that each strobed line segment is created using different effective time exposures. This results in the peak intensity of each strobed segment being proportional to the pulse duration, thus the ordering of the peak pixel intensities of each line segment can be used as an alternative coding scheme to resolve the directional ambiguity. Figure 4.8 shows a surface plot of the grey scale intensity variation of the strobed image of a single seed. On examining the middle two peaks

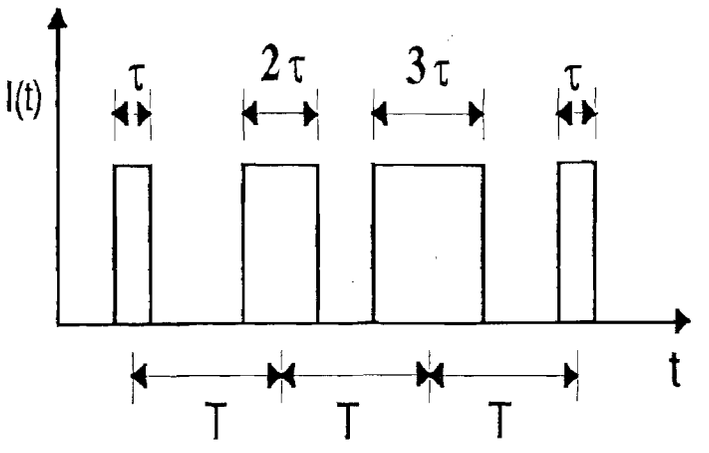

Figure 4.7: Schematic diagram of the coded strobe sequence.

in Figure 4.8, it can be seen that the intensity of one is approximately twice the other. We thus conclude that these two middle pulses correspond to the first two pulses in Figure 4.7. Since the shorter pulse in Figure 4.7 occurs first, we can be sure that particle in Figure 4.8 was moving to the left. It is clear that the width and peak intensity of the two outer peaks may not be reliable since the particle may have been entering or leaving the sheet during these times.

Using the chosen laser pulse widths and assuming typical seed velocities, the particle image travels only a few pixels between flashes. An estimate of the seed position using only the peak intensity value will thus result in the particle position being accurate to within half a pixel, resulting in an uncertainty in the velocity of up to 50%. This uncertainty clearly decreases for higher seed velocities. In order to decrease this uncertainty, it is necessary to estimate particle positions with sub-pixel resolution.

Sub-pixel Resolution

Estimation of the position of point source using peak intensity gives the position accurate to within $\pm$ 0.5 of the pixel separation. In terms of object distance, this accuracy will depend

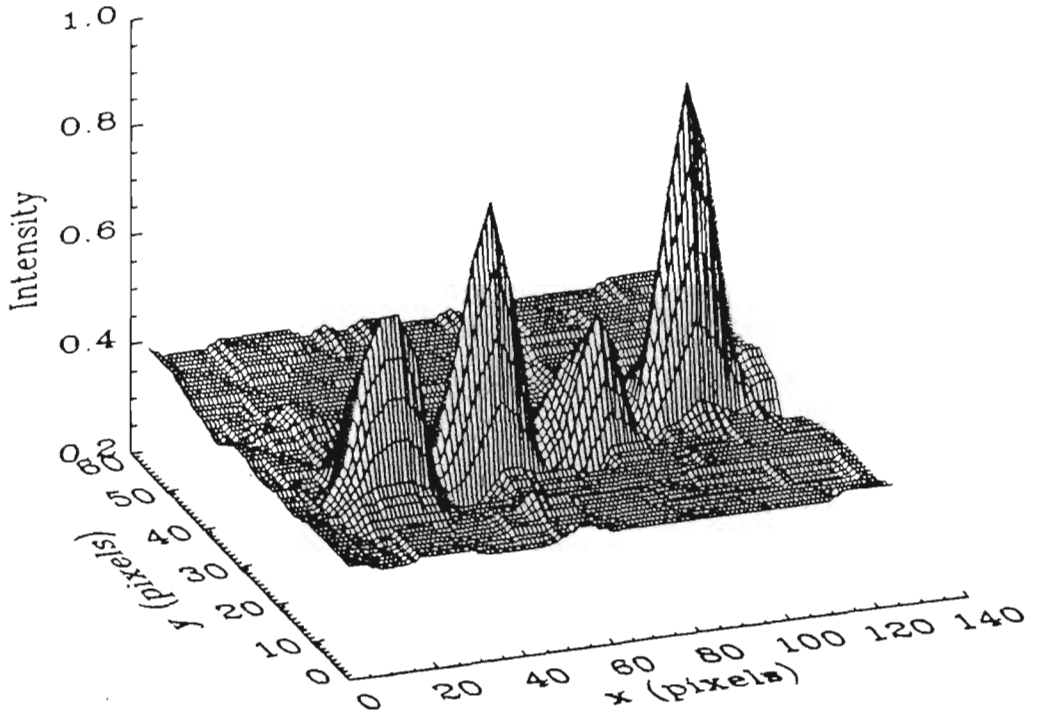

Figure 4.8: Grey scale intensity variation of a single particle illuminated by a coded strobe pulse.

on the size of the CCD array and the magnification of the lens. In our application, the pixel separation in the object plane was 0.8 mm/pixel over a field of view of 200 mm x 200 mm.

Examining the intensity distribution of the strobed images as shown in Figure 4.8, it can be seen that each strobed image of the seed has an approximate gaussian shape. One possible method of improving on position accuracy is to determine the coordinates of all points exceeding a predetermined intensity level around a particular peak, and computing an average position. This can at least improve the estimate to less than half a pixel spacing. A more accurate method is to employ a least square gaussian curve fit to the intensity profile in the x (horizontal) and y (vertical) directions about each peak. The coordinates of the peak can then be determined using the fitted curves. Alternatively, the intensity in the x and y directions can be interpolated using the following algorithm: The intensity profile in horizontal and vertical direction about the peak is Fourier transformed using an FFT of length N_1, where N_1 is sample length of the intensity profile. The spectrum is then zero padded to a length N_2 , $N_2 > N_1$, and the inverse Fourier transform computed using an inverse FFT of length N_2 to give the interpolated intensity profile in the respective directions.

An interpolation factor of N_2/N_1 is achieved. In our application an interpolation factor of 64/1 was used. We will refer to this form of interpolation as the Fourier interpolation method. This method approaches the ideal reconstruction of an analogue signal from its digital samples (*Oppenhiem and Schaffer, 1990*). A peak search using the interpolated intensity profile in the x and y direction gives the position of the peak accurate to within the interpolated pixel spacings.

F. Analysis Procedure for high seed density applications

In cases where high seed densities are present it is more beneficial to employ cross correlation techniques (*Craig et al., 1996, Chang et al., 1996*) to track the image of a group of seeds in consecutive frames or fields, since this technique allows for greater automation. This type of analysis is commonly referred to as Digital Correlation Image Velocimetry (DCIV). Correlation techniques involve finding matching structure between two images and therefore requires high seed densities. The presence of unmatching seeds or seed patterns between images simply contributes to noise. Provided the signal-to-noise ratio of the matching structures is large enough, then the peak of the computed cross-correlation function is a good estimate of the displacement of that particular structure.The cross correlation can be computed in the spatial domain by explicit evaluation of the 2D cross correlation function (*Fincham and Spedding, 1997*) or in the spectral domain by computing the cross spectral density function and transforming back into the spatial domain using the 2D FFT (*Willert and Gharib, 1991*).

The cross correlation of the images in the Fourier domain are performed as follows: Each image frame is sub-divided into smaller 32 × 32 pixel sub-images, and transformed into the fourier domain using a 2D FFT algorithm. This FFT of a sub-image in the first frame is multiplied by the conjugate of the FFT of the corresponding sub-image in the second frame, which is then transformed back into the spatial domain as given in equation 4.9 below.

$$R_{fg}(u,v) = F(u,v).G^*(u,v)$$
$$r_{fg}(m,n) = FFT^{-1}\{R_{fg}(u,v)\} \qquad (4.9)$$

where $F(u,v)$ is the Fourier transform of the sub-image, $f(m,n)$, in the first video frame, $G^*(u,v)$ is the conjugate of the Fourier transform of the corresponding sub-image, $g(m,n)$, in the second frame, and $r_{fg}(m,n)$ is the computed 2D cross correlation function of the sub-images. The intensity profile along the x and y direction about the peak in the computed cross correlation is then interpolated using the Fourier interpolation method. The displacement of each sub-image is thus estimated to within the interpolation factor, i.e. typically 1/64, of the original pixel spacing.

When using 2D FFT algorithms, it is beneficial to use sub-images having sizes that are powers of two. This, however, does not necessarily preclude the computation of the displacement of a sub-image whose dimensions are not a power of two. This is achieved as follows: Typically a smaller sub-image from the first frame, say 12 x 18 pixels, about some point (k,l), is selected. This odd-sized sub-image is then adjusted, such that it has a zero mean, and then zero padded in the horizontal and vertical direction to a size of 32 x 32 pixels, resulting in a border of zero intensity around the original 12 x 18 pattern box. The search area, that is the corresponding region in the second frame where a match with the sub-image in the first frame is likely to occur, can be a full 32 x 32 sub-image centred at (k,l) in the second frame. The co-ordinates of the peak in the resulting cross correlation are then the displacement of the original 12 $\times$ 18 pattern box. The zero padding does not influence the cross correlation result. In fact, the zero padding eliminates some of the problems associated with implementing cross correlation using the FFT, such as wrap around (*Oppenhiem and Schaffer, 1990*).

Since the cross correlation technique requires two separate images, we are therefore limited by the 20 ms(40 ms) sampling time associated with field (or frame) update rate of a conventional CCD camera. However, it is possible to obtain pairs of images separated by a few microseconds while still using video frame update rate by using a non-interlaced progressive scan camera and appropriately strobing the light sheet. The essential steps in determining the velocity flow field using the cross correlation technique is as described above except that the image capture configuration was changed in order to achieve sampling times smaller than the frame update rate.

The experimental setup used for DCIV is similar to that shown in Figure 1, except for the following changes; A strobe light is used as a source for the light sheet and a non-interlaced progressive scan digital camera, connected to a frame grabber, was used to record images directly to the hard disk. The non-interlaced camera provides a high spatial resolution, 764 x 468 pixels, and by strobing the light sheet at the end of one frame time and then again at the beginning of the next frame time, it is possible to obtain pairs of images with sampling times ranging from a few microseconds to a few milliseconds while still using the normal frame update rate. Since the sequence of the images is known, the 180 degree directional ambiguity,usually associated with multiple strobing during a single frame time, is removed.

The above cross correlation method was used to measure the velocity flow field of a 0.4 Hz plunging wave and 0.9 Hz spilling wave breaking on a 1:20 slope beach, and having deep water wave heights of 11 cm and 16 cm, respectively.

Figures 4.9(a) and (b) shows a pair of images of the crest of the plunging wave approximately 50 cm beyond the break point. The images are displaced 0.826 ms apart.

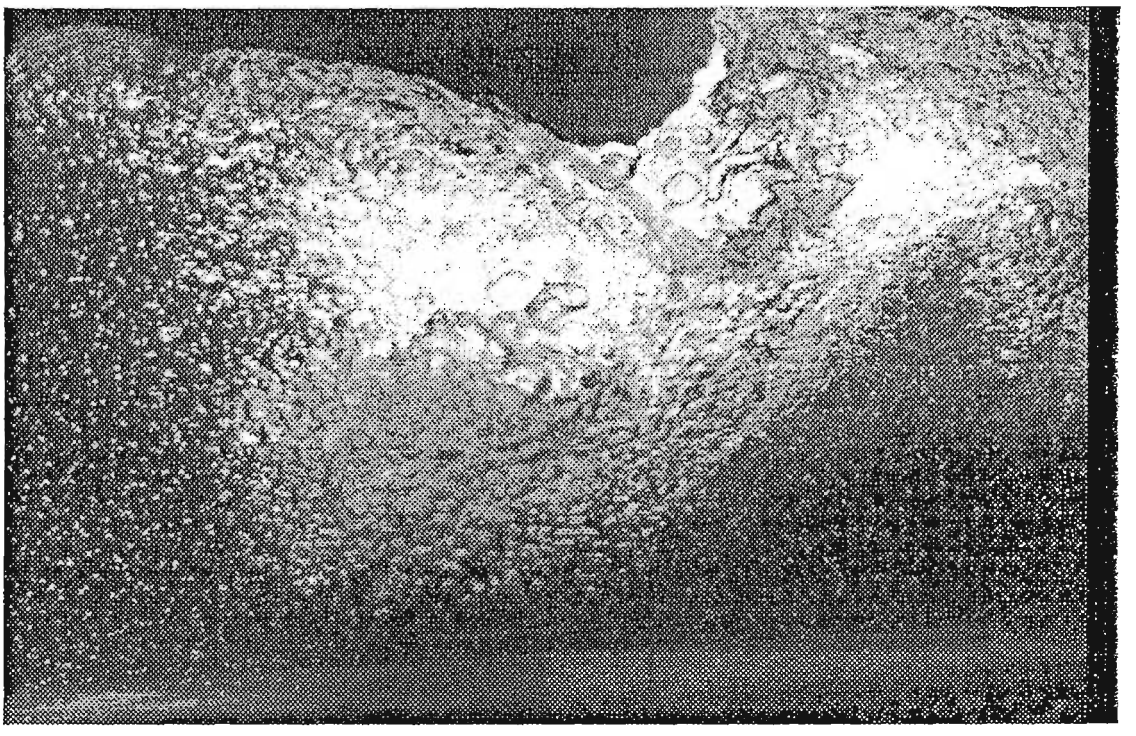

Figure 4.9:(a) First image of the crest of a plunging wave in the surf zone.

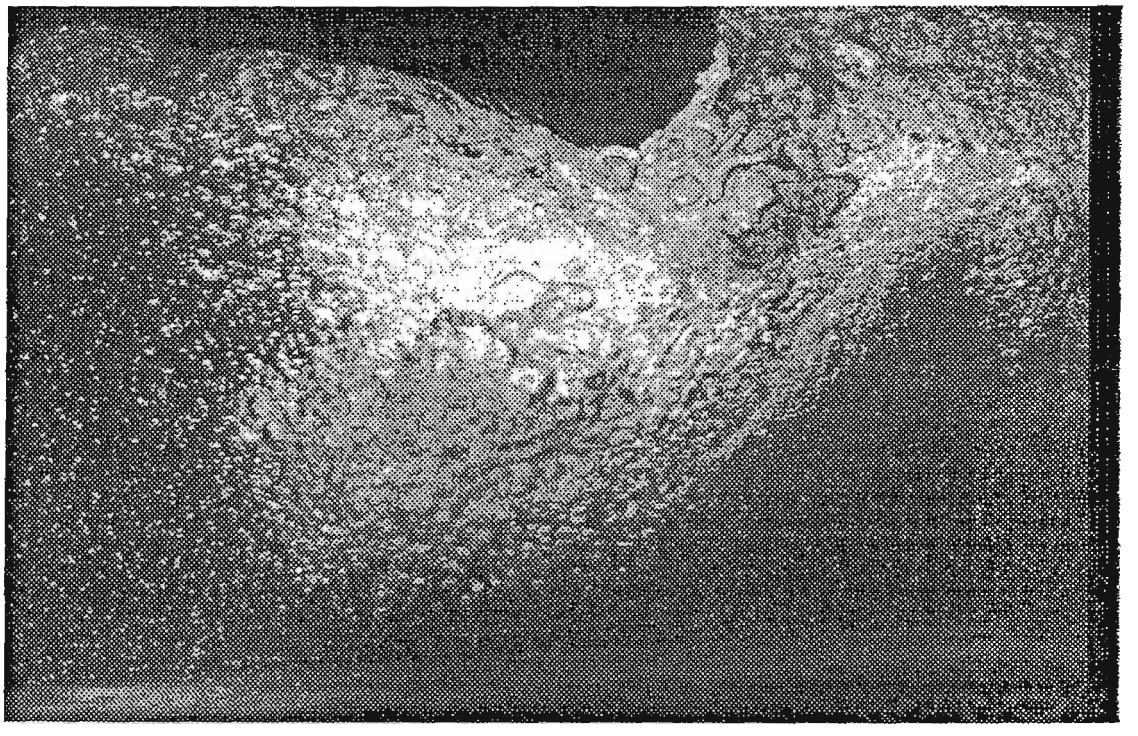

Figure 4.9:(b) Image of the crest of the same plunging wave in (a) captured 0.826 ms later.

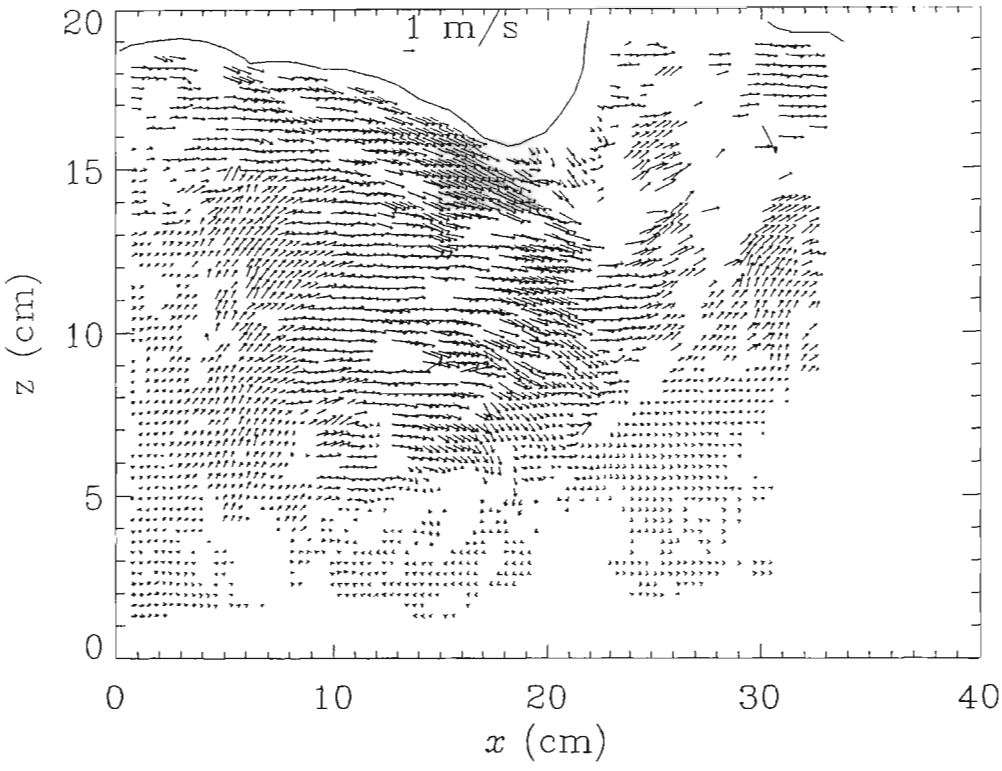

Figure 4.9:(c) Instantaneous velocity field computed using 2D cross correlation of images in (a) and (b).

These images show a scene containing both bubbles resulting from the wave breaking, and polystyrene seed particles. By overlaying the two images, it can be seen that the structure of corresponding portions of the two images persists for the duration of sampling time with very little distortion. The calculated velocity vector field for the above image pairs is shown in Figure 4.9(c). There is maximum flow velocity ($\sim$ 3 m/s) near the surface of the wave, whilst near the bottom, the velocity is almost zero. The formation of a large eddy in the centre of both images and in the vector field is evident. As the rise velocity of the air bubbles in this highly turbulent flow regime is negligible in comparison to the velocity components of the flow, it is thus possible to obtain a detailed flow pattern well into the aerated region of the wave using the air bubbles to create the necessary structure. In the past, some researchers (*Craig and Thieke, 1998*) have gone to great lengths to remove the effects of the air bubbles in order to highlight particulate matter that has been deliberately added to the flow. This appears not to be necessary for the flow regime under discussion. In streamline laminar flow, however, it would be necessary to obtain an estimate of the bubbles rise velocity and apply the necessary correction to the flow field. The sampling time is determined by satisfying the competing criteria of requiring a persistent bubble structure as

well as a measurable displacement.

4.3. Water Level Measurements

Measurement and Analysis

To obtain a time series measurement of the water level, the wave flume was imaged from the side with the camera located at the still water line level and the wave illuminated from above. A black backing sheet was placed behind the flume and used as a backdrop. This arrangement allows the air-water interface to be identified by locating the sharp transition in the vertical lines of grey scale intensity. The camera was also mounted on a base that could be translated on a set of rails parallel to the flume.

The procedure for extracting the time series was as follows: At each position along the flume a video recording of the wave was made. A single vertical line of pixels at a fixed position was then extracted from a sequence of images. These vertical samples were then stacked side by side to create a new image, called a keogram. This procedure is depicted in Figure 4.10. Figures 11(a) and (b) show examples of keograms of a wave, before and after breaking, respectively.

A robust cross correlation algorithm was developed to determine the position of the air-water interface. The transition point was enhanced by cross correlating the vertical grey-scale intensity profile with the edge detection function shown in Figure 4.12. The resulting cross correlation was a signal with an easily found peak at the transition point. The width w1 and w2, and the amplitude a1 and a2 of the cross correlating function were adjusted to maximise the value of the resulting peak at the transition.

The keogram technique was also used to measure the geometry of the roller and the aerated region of the wave in the surf zone. This was achieved by first forming a phase averaged keogram of the wave and demarcating the high intensity region which was identified as being the roller or aerated region.

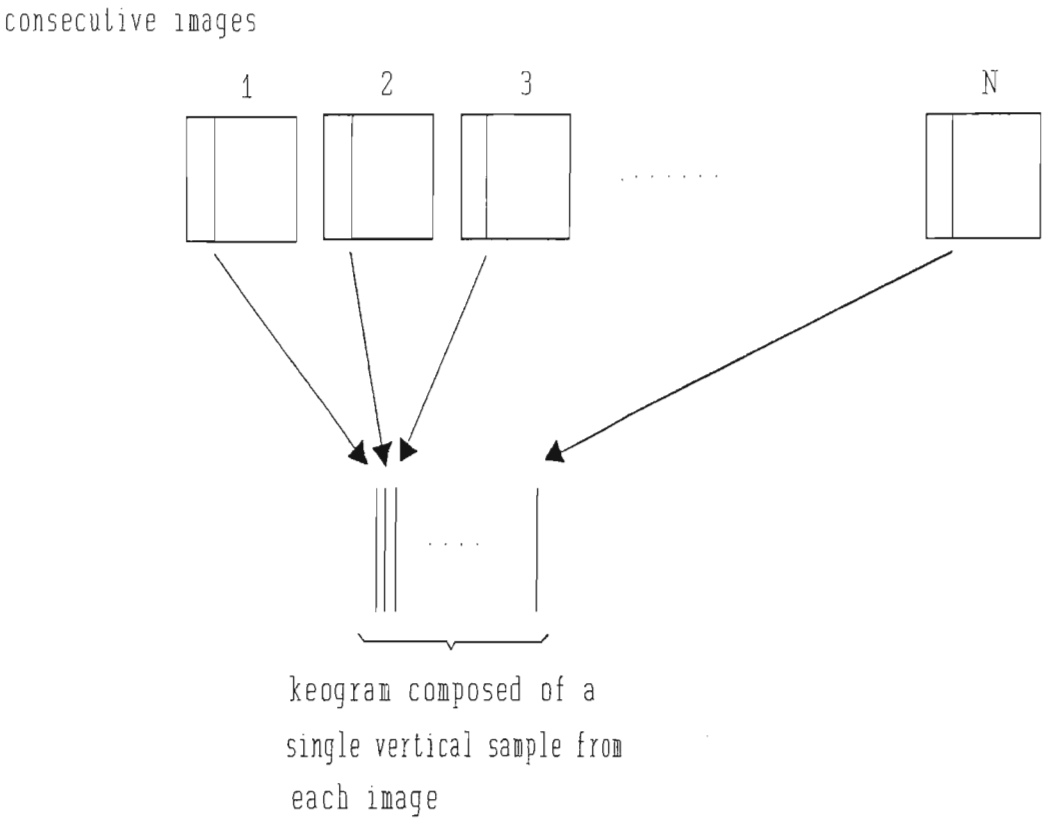

Figure 4.10:The generation of a keogram from a sequence of video images for the measurement of the time series of the water levels in a 2D wave flume.

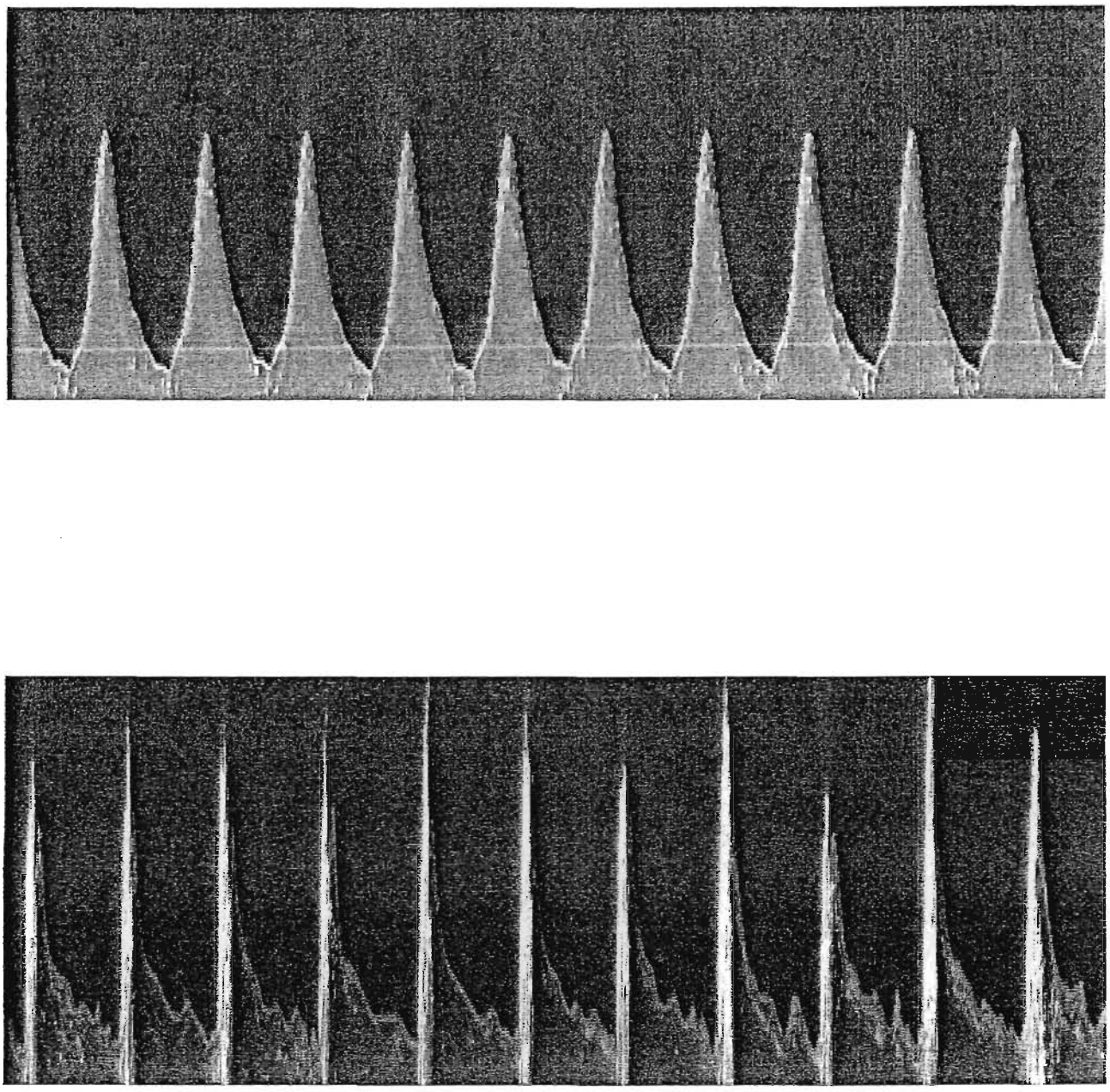

Figure 4.11: Examples of keograms of waves (top) before and (bottom) after breaking. The vertical and horizontal distances in the keogram represent height in image cordinates and time increments, respectively.

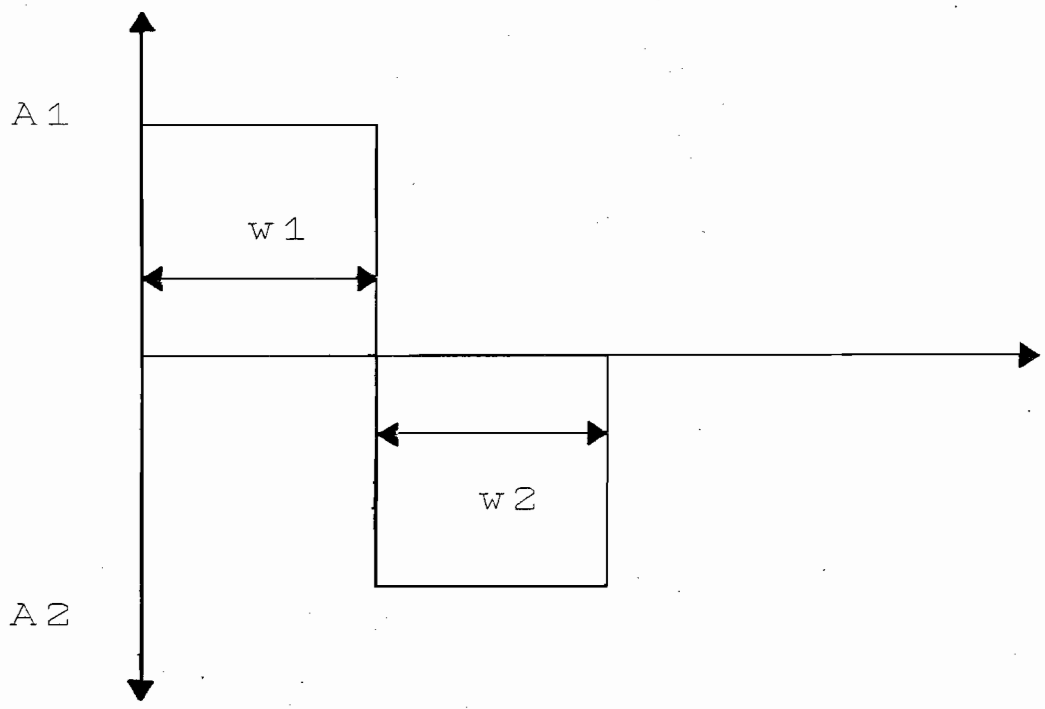

Figure 4.12: Example of an edge detecting function. The width w1 and w2, and amplitude A1 and A2 are adjusted to suit the application.

Extensive results of time series of water-levels measurement and aeration measurement are provided in the next chapter, together with resistive wave-gauge comparisons.

4.4. Summary

The measurement of the velocity flow fields in a laboratory surf zone using digital particle image velocimetry is demonstrated. The choice and operation of various components in the system were highlighted. In order to implement the sub-pixel estimation techniques described, it is necessary for the particle image to span a few pixels. Velocity estimation was accomplished by observing the position of seed particle at two or more time instances. The particle positions were sampled at the TV field/frame update rate. Higher effective sampling rates were accomplished by strobing the laser sheet within each field time. The direction of particle motion was determined by noting the sequence of the images in the field/frame analysis and by the use of pulse coding the laser. Higher sampling rates were achieved using a non-interlaced progressive scan camera and strobing the light sheet. This setup together with the cross correlation method of analysis was used to measure the instantaneous velocity

vector field in the highly aerated crest of a plunging wave.

The measurement of time series of the water level in a 2D flume using video techniques was also discussed and demonstrated. The time series of the wave was extracted from a keogram generated at fixed positions along the flume. The measurement of the roller area of waves in the surf zone is also possible using keogram technique.

A number of techniques suitable for measuring the velocity flow field and water levels of waves in the surf zone have been described and demonstrated. It has been shown that by using particle image velocimetry and correlation image velocimetry techniques it is now possible to obtain velocity measurements well into the aerated region of the wave. The calibration and sensitivity analysis of the video techniques will be presented within the context of surf zone measurements in Chapters 5 and 6. More comprehensive analyses using the techniques, including using the data for computational model validation, will be presented in Chapters 5, 6 and 7.

References

1. Banner M.L., Peregrine D.H., Wave breaking in deep water, *Ann. Rev. Fluid Mech.* **25**, 373-397, 1993.

2. Basco D., A Qualitative description of wave breaking, *J. Waterway, Port, Coast. and Ocean Eng.* **111**, 1985.

3. Battjes J.A., Computation of set-up, longshore currents, run up and overlapping due to wind-generated waves, *Comm. on Hydraulics, Dept. of Civil Eng., Delft Univ. of Technology* **74-2**, 1974

4. Battjes J.A., Janssen J.P.F.M., Energy loss and set-up due to breaking of random waves, 1978.

5. Beji S., Battjes J.A., Experimental investigation of wave propagation over a bar, *Coast. Eng.* **19**, 151-162, 1992.

6. Bonmarin P., Geometric properties of deep water breaking waves, *J. Fluid Mech.* **209**, 405-433, 1989.

7. Dally W.R., Brown C.A., A modeling investigation of the breaking wave roller with application to cross-shore currents, *J. Geophysical Res.* **100 C12**, 24873-24883, 1995.

8. Divoky D., Le Mehaute B., Lin A., Breaking waves on gentle slopes, *J. Geophysical Res.* **75**, 1681-1692, 1968.

9. Duncan J.H., An experimental investigation of breaking waves produced by a towed hydrofoil, *Proc. R. Soc. Lond.* **A 377**, 331-348, 1981.

10. Duncan J.H., Qiao H., Philomin V., Wenz A.,Gentle spilling breakers: Crest profile evolution, *J. Fluid Mech.* **379**, 191-222, 1998.

11. Engelund F., A simple theory of weak hydraulic jumps, *Inst. of Hydrodynamics and Hydraulic Eng., ISVA, Techn. Univ. Denmark* **54**, 29-32, 1981.

12. Flick R.E., Guza T., Inman D.L., Elevation and velocity measurements of laboratory shoaling waves, *Geophysical Res.* **86**, 1981.

13. Fredsoe J., Deigaard R., Mechanics of Coastal Sediment Transport, *World Scientific* , 1992.

14. Galvin Jnr C.J., Breaker type classification on three laboratory beaches, *J. Geophysical Res.* **73**, 3651-3659, 1968.

15. Govender K., Velocity, vorticity and turbulence measurements in the surf zone, *PhD Thesis* , 1999.

16. Govender K., Alport M.J., Mocke G.P., Michallet H., Video measurements of fluid velocities and water levels in breaking waves, *Physica Scripta* **T92** , 152-159, 2002a.

17. Govender K., Mocke G.P., Alport M.J., Video imaged surf zone wave and roller structures and flow fields, *J.Geophysical Res.* **107 (C7)**, 3072, 2002b.

18. Govender K., Mocke G.P., Alport M.J., Dissipation of isotropic turbulence and length scale measurements through the wave roller in laboratory spilling waves, *J.Geophysical Res.* **109**, C08018, 2004.

19. Gross M.G., Oceanography, *Merrill* , 1990.

20. Hansen J.B., Svendsen I.A., A theoretical and experimental study of undertow, *Proc.* **19th** *Int. Coast. Eng. Conf.*, 2246-2262, 1984.

21. James I.D., Non-linear waves in the nearshore region: shoaling and set-up, *Estuarine Coast. Mar. Sci.* **2**, 207-234, 1974.

22. Korteweg D.J., deVries G., On the change of form of long waves advancing in a rectangular channel, and on a new type of long stationary waves, *Phil. Mag.* (5) **39** , 422-443 , 1895.

23. Lighthill J., Waves in Fluids, *Cambridge University Press.*, 1978.

24. Le Mehaute B., An introduction to hydrodynamics and water waves, *Springer-Verlag*, New York, 1976.

25. Longuet-Higgins M.S., Stewart R.W., Radiation stresses in water waves; a physical discussion with applications, *Deep-Sea Res.* **11**, 529-562, 1964.

26. Mei C.C., The applied dynamics of ocean surface waves, *Wiley* , 1983.

27. Madsen P.A., Murray R., Sorensen O.R., A new form of the Boussinesq equations with improved linear dispersion characteristics, *Coast. Eng.* **15**, 371-388, 1991.

28. Mocke G.P.,The structure and modelling of surf zon turbulence due to wave breaking, *CSIR report*ENV/S-C97069A, 1998.

29. Mory M., Currents induced by breaking waves over a bar , *Modelling of Coast. and Estuarine processes* , 27-38, 1994.

30. Nwogu O., Alternative form of Boussinesq equations for nearshore wave propagation, *J. Waterway, Port, Coast. and Ocean Eng.* **119**, 618-638, 1993.

31. Peregrine D.H., Long waves on a beach, *J. Fluid Mech.* **27**, 815-827, 1967.

32. Perlin M., He J., Bernal L.P., An experimental study of deep water plunging breakers, *Phys. Fluids* **8**, 2365-2374, 1996.

33. Prasad A.K., Adrian R.J.,Landreth C.C., Offuth P.W., Effect of resolution on the speed and accuracy of particle image velocimetry interrogation, *Exp. in Fluids* **13**, 105-116, 1992.

34. Rapp R.J., Melville W.K., Laboratory measurements of deep water breaking waves, *Phil. Trans. R. Soc. London A* **331**, 735-800, 1990.

35. Sakai T., Battjes J.A., Wave shoaling calculated from Cokelet's theory, *Coast. Eng.* **4**, 65-84, 1990.

36. Schaffer H.A., Deigaard R.,Madsen P.A., A two dimensional surf zone model based on the Boussinesq equations, *Coast. Eng.* , 576-589, 1992.

37. Smith E.R, Kraus N.C., Laboratory study on macro features of wave breaking of bars and artificial reefs, *CERC technical report* , 1990.

38. Stive M.J.F., Velocity and pressure field of spilling breakers, *Proc.* **17th** *Int. Coast. Eng. Conf.*, 547-566, 1980.

39. Stokes G.G., On the theory of oscillatory waves, *Camb. Trans.*, **8**, 441-473, 1847.

40. Svendsen I.A., Wave heights and set-up in a surf zone, *Coast. Eng.* **8**, 303-329, 1984.

41. Ting F.C.K., Kirby J.T., Observation of undertow and turbulence in a laboratory surf zone, *Coast. Eng.***24**, 51-80, 1994.

42. Whitham G.B., Linear and non-linear waves, *Wiley* , 1974.

43. Willert C.E., Gharib M., Digital particle image velocimetry, *Exp. Fluids* **10**, 181-193, 1991.